Backward Stimulated Raman Scattering

G.R. Morrison
January 1993

Submitted in fulfilment of the requirements for the degree of Master of Science.

Department of Physics
University of Cape Town.

Abstract

We present both a theoretical overview and an experimental investigation of the stimulated Raman effect. A new prediction is made for the steady state linewidth of the forward Stokes output in the presence of a depleted pump. The theory is developed with the aim of gaining an understanding of the mechanism which favours stimulated Raman output in the backward direction. The experimental investigation with hydrogen as the Raman medium, was confined to a transient regime. We were therefore unable to verify our prediction for the steady state Stokes linewidth. A rare observation of anti-Stokes radiation in the backward direction was made. The general observations shed light on the question of the mechanism responsible for 'predominantly' backward Stokes output.

Introduction and Motivation

This is a somewhat different thesis to that originally intended. The original idea was to investigate stimulated Raman scattering in hydrogen as a means of frequency shifting the output of a frequency doubled $Nd:YAG$ $(532\,nm)$ laser for use as the pump in *coherent anti-Stokes Raman scattering* (CARS) experiments in nitrogen. The frequency shift was required since the tunability range of the tunable $Ti^{3+}:Al_2O_3$ laser to be used in these experiments was not compatible with the $Nd:YAG$ as pump. It was decided to attempt to obtain the stimulated Raman radiation in the backward direction, as this would enable the transmitted pump beam to be used to pump the tunable source, thus simplifying the CARS setup. Initially the main interest lay in ensuring that sufficient energy conversion to the backscattered beam could be achieved and that the spectral width of the backscattered output was narrow enough for use as the pump in a CARS experiment.

A preliminary review of the theory was undertaken after some introductory experimental work. It soon became clear that the topic of stimulated Raman scattering in the backward direction with a single longitunal mode pump is in itself of great interest. This realisation together with the unavailability of the laser for more than a year prompted a more thorough investigation of the available theory. This revealed that the backward scat-

tered process has received far less attention in the literature than its forward scattered counterpart, possibly as a result of the rather special conditions under which it is the dominant direction of the scattered output [1]. In fact the precise dynamics of the interaction giving rise to predominantly backscattered output are not yet clear. It was decided that it would be of great interest to investigate this phenomenon more carefully. When the laser finally became available, a more detailed experimental investigation, than was initially invisaged, was performed. This then motivates the shift in emphasis of this thesis which now contains the fruits of both a theoretical and experimental investigation into the phenomenon of backward stimulated Raman scattering.

We will now give an overview of the presentation. In Chapter 1 which follows, a general discussion of the modelling of a nonlinear response is presented. The nonlinear susceptibilities are described in terms of the classical polarisability model. Maxwell's equations, which are used to describe the propagation of the nonlinear response through the medium, are presented with careful attention being paid to the various approximations.

Chapter 2 contains an extensive theoretical investigation into stimulated Raman scattering. Most of the work is a review of previously available results, although an attempt has been made to include more detail than is generally available. The theory is developed from the simple steady state theory to include the depletion of the pump as well as the possibility of a focused pump geometry. A new development has been made to the theory of the spectral distribution of the Stokes output for the case where the depletion of the pump is included. Also, a neat model of propagation in a focused geometry has been applied to the case of the backward process. The effects

of dispersion and finite input spectral widths are included together with a discussion of anti-Stokes coupling. This all culminates in a detailed discussion of a simple transient theory for backward stimulated Raman scattering.

The results of our experimental investigation appear in Chapter 3. Specifically we looked at energy conversion efficiencies and linewidths of the backscattered output. We also investigated the temporal relationship between the various input and output beams. The effects of varying the laser intensity, hydrogen pressure and focusing characteristics on the various measured quantities were investigated. Wherever possible, contact has been made with the theoretical considerations of Chapter 2.

Finally, in Chapter 4 a discussion and conclusion of the investigation is presented. Specifically, the nature of the initiation interaction giving rise to backward stimulated Raman scattering will be discussed with respect to both theoretical and experimental considerations. Also, the possible use of this process as a means of frequency shifting the $Nd:YAG$ output ($532\,nm$) for use as the pump in CARS work will be discussed.

Chapter 1

Introductory Nonlinear Optics

Introduction

Nothing in nature responds purely linearly to stimuli. There is always a point at which the stimulus becomes sufficiently strong to induce a nonlinear response. This is also true of matter under the stimulation of light. The study of the vast array of effects observable due to this nonlinear response of matter to light, forms the exciting field of nonlinear optics. The required strength of the optical stimulus necessary to illicit a nonlinear response from the medium with which it is interacting is not usually achievable with everyday light-sources. In the overwhelming majority of cases a laser is required to invoke a nonlinear response from a medium.

Nonlinear optical effects are the manifestations of a nonlinear interaction between light and matter, which can be seen to arise in the following way. Optical signals existing in a medium will cause an oscillating polarisation in the medium. If the optical stimulus is sufficiently strong, this polarisation will be nonlinear and as such it will contain oscillating polarisations at fre-

quencies different from those of the optical signal originally in the medium. This nonlinear polarisation can itself interact with the fields propagating in the medium, causing nonlinear changes in the fields themselves. Thus in order to be able to describe nonlinear optical processes, we need to calculate the nonlinear polarisation induced in the medium by the optical fields. This is achieved via the constitutive equations. The oscillating polarisation is responsible for describing the continuing propagation of the optical fields through the medium, as governed by Maxwell's equations. The two steps of this feedback mechanism responsible for nonlinear optical effects will be described in the following two sections. Starting from Maxwell's equations in the section below, we will derive the wave equation describing the propagation of the waves through a medium. This will be followed by a description of the polarisation which acts as a source for this propagation.

1.1 Maxwell's Equations

Light waves as with all other electromagnetic phenomena are governed by Maxwell's equations:

$$\begin{aligned}
\vec{\nabla} \times \vec{E} &= -\frac{1}{c}\frac{\partial \vec{B}}{\partial t} \\
\vec{\nabla} \times \vec{H} &= \frac{1}{c}\frac{\partial \vec{E}}{\partial t} + \frac{4\pi}{c}\vec{J} \\
\vec{\nabla}.\vec{D} &= 4\pi\rho \\
\vec{\nabla}.\vec{B} &= 0
\end{aligned} \tag{1.1}$$

where we have used a generalised charge density ρ and current density $\vec{J}$, both of which are time dependent, as sources. These source terms can be

expanded in a multipole expansion [18]:

$$\rho = \rho_0 - \vec{\nabla}.\vec{P} - \vec{\nabla}(\vec{\nabla}.\vec{\mathbf{Q}}) + \ldots$$

$$\vec{J} = \vec{J}_0 + \frac{\partial \vec{P}}{\partial t} + c\vec{\nabla} \times \vec{M} + \frac{\partial}{\partial t}(\vec{\nabla}.\vec{\mathbf{Q}}) + \ldots \tag{1.2}$$

These expressions are, however, unphysical in the optical region [18]. We therefore deal instead with the generalised polarisation:

$$\vec{\mathbf{P}} = \vec{P} + \vec{\nabla}.\vec{\mathbf{Q}} + \ldots \tag{1.3}$$

Also for our purposes the magnetic multipole moments will be limited to the dipole approximation so that the linear constitutive relationship $\vec{B} = \mu\vec{H}$ will be assumed to hold. Thus the charge and current densities can be replaced by:

$$\rho = \rho_0 - \vec{\nabla}.\vec{\mathbf{P}}$$

$$\vec{J} = \vec{J}_0 + \frac{\partial \vec{\mathbf{P}}}{\partial t} \tag{1.4}$$

so that the charge conservation law:

$$\vec{\nabla}.\vec{J} + \frac{\partial \vec{\mathbf{P}}}{\partial t} = 0$$

is seen to hold. Here ρ_0 is the static charge density and $\vec{J}_0$ is the dc current density. Thus Maxwell's equations with $\vec{\mathbf{P}}$ as the only time-varying source term become:

$$\vec{\nabla} \times \vec{E} + \frac{1}{c}\frac{\partial \vec{B}}{\partial t} = 0$$

$$\vec{\nabla} \times \vec{B} = \frac{\mu}{c}\frac{\partial}{\partial t}(\vec{E} + 4\pi\vec{\mathbf{P}}) + \frac{4\pi\mu}{c}\vec{J}_0 \tag{1.5}$$

$$\vec{\nabla}.(\vec{E} + 4\pi\vec{\mathbf{P}}) = 4\pi\rho_0$$

$$\vec{\nabla}.\vec{B} = 0$$

from which we can obtain the wave equation governing the propagation of the fields through a dielectric medium:

$$[\vec{\nabla} \times (\vec{\nabla}\times) + \frac{\mu}{c^2}\frac{\partial^2}{\partial t^2}]\vec{E}(\vec{r},t) = -\frac{4\pi\mu}{c^2}\frac{\partial^2}{\partial t^2}\vec{\mathbf{P}}(\vec{r},t) \tag{1.6}$$

In general $\vec{\mathbf{P}}$ is a nonlinear function of the fields. The exact relationship with the fields is known as the constitutive equation and this fully describes the response of the medium to the fields. For sufficiently strong fields the response of the medium will be nonlinear which will enable interaction between the various fields. As long as the fields are not too strong, the generalised polarisation can be expanded as a power series in the field:

$$\begin{aligned}\vec{\mathbf{P}}(\vec{r},t) &= \sum_{n=1}^{\infty}\int_{-\infty}^{\infty}\chi^{(n)}(\vec{r}-\vec{r}_1,\ldots,\vec{r}-\vec{r}_n,\ldots,t-t_1,\ldots,t-t_n,\ldots) \\ &\quad\times\vec{E}(\vec{r}_1,t_1)\ldots\vec{E}(\vec{r}_n,t_n)\ldots d\vec{r}_1\,dt_1\ldots d\vec{r}_n dt_n\ldots \end{aligned}\tag{1.7}$$

where it is understood that there are n integrations to be performed in the n^{th} term. In the case of a linear response, the above expression reduces to:

$$\vec{\mathbf{P}}^{(1)}(\vec{r},t) = \int_{-\infty}^{\infty}\chi^{(1)}(\vec{r}-\vec{r}_1,t-t_1).\vec{E}(\vec{r}_1,t_1)\,d\vec{r}_1 dt_1 \tag{1.8}$$

Where $\chi^{(1)}$ is the linear susceptibility and is necessarily a tensor of rank 2. In the general case it therefore follows that $\chi^{(n)}$ is a tensor of rank $(n+1)$ and is known as the n^{th} order susceptibility. The evaluation of these susceptibilities will be reviewed in the following section.

For the moment we proceed with the description of the propagation of fields through a medium in which a nonlinear interaction is taking place. In this case we can separate the polarisation into a linear and nonlinear portion:

$$\vec{\mathbf{P}}(\vec{r},t) = \vec{\mathbf{P}}^{(1)}(\vec{r},t) + \vec{\mathbf{P}}^{NL}(\vec{r},t) \tag{1.9}$$

where $\vec{\mathbf{P}}^{NL}$ is obviously the $\sum_{n=2}^{\infty}$ portion of eqn. 1.7. Then the wave equation becomes:

$$[\vec{\nabla} \times (\vec{\nabla} \times) + \frac{\mu \underline{\epsilon}}{c^2} \frac{\partial^2}{\partial t^2}] \vec{E}(\vec{r}, t) = -\frac{4\pi\mu}{c^2} \frac{\partial^2}{\partial t^2} \vec{\mathbf{P}}^{NL}(\vec{r}, t) \tag{1.10}$$

where

$$\underline{\epsilon} \vec{E}(\vec{r}, t) = \vec{E}(\vec{r}, t) + 4\pi \vec{\mathbf{P}}^{(1)}(\vec{r}, t)$$

If we now expand the fields and the polarisation in the wave vector and frequency domains according to the fourier transform and its inverse:

$$\vec{A}(\vec{r}, t) = \int_{-\infty}^{\infty} \vec{A}(\vec{k}, \omega)\, e^{i(\vec{k}.\vec{r} - \omega t)} d\vec{k} d\omega$$

$$\vec{A}(\vec{k}, \omega) = \int_{-\infty}^{\infty} \vec{A}(\vec{r}, t)\, e^{-i(\vec{k}.\vec{r} - \omega t)} d\vec{r} dt \tag{1.11}$$

and we make the assumption that the linear susceptibility can be similarly transformed, then we have for each frequency component:

$$\vec{\mathbf{P}}^{(1)}(\vec{k}, \omega) = \chi^{(1)}(\vec{k}, \omega) \vec{E}(\vec{k}, \omega) \tag{1.12}$$

This result can be generalised for higher order polarisations, yielding:

$$\begin{aligned} \vec{\mathbf{P}}^{(n)}(\vec{k}, \omega) &= \chi^{(n)}(\vec{k} = \vec{k}_1 + \vec{k}_2 + \ldots + \vec{k}_n, \omega = \omega_1 + \omega_2 + \ldots + \omega_n) \\ &\quad \times \vec{E}(\vec{k}_1, \omega_1) \ldots \vec{E}(\vec{k}_n, \omega_n) \end{aligned} \tag{1.13}$$

From equation 1.8 it should be apparent that the polarisation exhibits a nonlocal response to the fields. This is illustrated by a change of variable:

$$t_1 = t - \tau \qquad \vec{r}_1 = \vec{r} - \vec{R}$$

in which case eqn. 1.8 becomes

$$\vec{\mathbf{P}}^{(1)}(\vec{r}, t) = \int_{-\infty}^{\infty} \chi^{(1)}(\vec{R}, \tau) \vec{E}(\vec{r} - \vec{R}, t - \tau)\, d\vec{R} d\tau \tag{1.14}$$

showing that the polarisation at location $\vec{r}$ and time t depends on the electric field at a position and time other than $\vec{r}$ and t.

We can now illustrate how the nonlinear susceptibility tensors describe a given nonlinear process by decomposing the field into an infinite set of monochromatic plane waves:

$$\vec{E}(\vec{r},t) = \hat{e}\sum_j E(\vec{r},t)\, e^{i(\vec{k}_j.\vec{r}-\omega_j t)} = \sum_j \vec{E}(\vec{k}_j,\omega_j) \tag{1.15}$$

We can write the polarisation down in a similar way:

$$\vec{\mathbf{P}}^{NL}(\vec{r},t) = \sum_j \vec{\mathbf{P}}^{NL}(\vec{k}_j,\omega_j)$$

If we consider a process which is described by a third order nonlinear susceptibility then we have:

$$\begin{aligned}\vec{\mathbf{P}}^{NL}(\vec{k},\omega) &= \vec{\mathbf{P}}^{(3)}(\vec{k},\omega) \\ &= \chi^{(3)}(\omega,\omega_1,\omega_2,\omega_3)\vec{E}(\vec{k}_1,\omega_1),\vec{E}(\vec{k}_2,\omega_2),\vec{E}(\vec{k}_3,\omega_3)\end{aligned} \tag{1.16}$$

So that a wave propagating through the medium at $\omega = \omega_1 + \omega_2 + \omega_3$ is described by the wave equation:

$$\begin{aligned}[\vec{\nabla}\times(\vec{\nabla}\times) + \frac{\mu\epsilon}{c^2}\frac{\partial^2}{\partial t^2}]\vec{E}(\vec{r},t) &= -\frac{4\pi\mu}{c^2}\frac{\partial^2}{\partial t^2}\chi^{(3)}(\omega,\omega_1,\omega_2,\omega_3) \\ &\quad\times\vec{E}(\vec{k}_1,\omega_1)\vec{E}(\vec{k}_2,\omega_2)\vec{E}(\vec{k}_3,\omega_3)\end{aligned} \tag{1.17}$$

Similar equations will exist to describe the evolution of the fields at the other frequencies as they propagate through the medium. Thus knowledge of the process occuring in a particular nonlinear effect enables the correct susceptibility to be chosen and hence calculated.

The above equation may be simplified by assuming that all the waves propagate in the same direction and that all the fields are polarised in the

same way. This enables us to dispense with the vectorial nature of the description. Also, since the nonlinear susceptibility is small compared to the linear portion, the relative change in the field amplitude over a wavelength will be small [3], thus enabling the slowly varying amplitude approximation to be invoked. This approximation is discussed in Appendix A. The wave equation then reduces to:

$$\left(\frac{\partial}{\partial z} + \frac{1}{v}\frac{\partial}{\partial t}\right) E(z,t) = -\frac{2\pi\mu\omega^2}{i\,k\,c^2}\mathbf{P}^{(3)}(z,t) \tag{1.18}$$

where the assumption $\frac{\partial^2}{\partial t^2}\mathbf{P}(z,t) = -\omega^2\mathbf{P}(z,t)$ has been made and it is understood that $E(z,t)$ represents the amplitude of the field at frequency ω. In order to obtain a workable equation it is necessary to consider the form of the susceptibilities more carefully so that calculable expressions can be found.

1.2 The Nonlinear Susceptibilities

The optical susceptibilities, describing as they do the response of the medium to the fields, depend in detail on the structure of the medium. Hence they can only be correctly determined by a full quantum mechanical calculation. This is most easily performed in the density matrix formalism. The necessary perturbation calculations are easily done for lower order susceptibilities ($n \leq 2$), but quickly become prohibitively long and complicated. Fortunately, diagramatical techniques based on Feynman diagrams have been devised [4, 5, 6] which enable one to simply write down the appropriate susceptibilty. However, for our purposes it will be much more instructive and less demanding to follow a classical model.

Before we proceed with the relevant model, there are some simplifications

which can be made. Firstly, the problem of the nonlocal response of the medium to the fields is resolved by the electric dipole approximation for dilute media, since in this case the susceptibilies are no longer functions of $\vec{r}$ (and hence $\vec{k}$). The electric dipole approximation is valid for stimulated Raman scattering as well as for many other nonlinear phenomena. In this approximation we neglect the contributions from all the higher order electric multipoles and from all the magnetic multipoles which are at least an order of magnitude less than the electric dipole contribution. We therefore have from eqn. 1.3

$$\vec{\mathbf{P}} = \vec{P}$$

and $\mu = 1$. Even in condensed media of isotropic or cubic structure only a simple correction is required to the local susceptibility [18]. For condensed media of other symmetries, the susceptibilities will exhibit their tensorial nature. As mentioned earlier, the n^{th} order optical susceptibility $\chi^{(n)}$, is a tensor of rank $(n+1)$ and has 3^{n+1} components. Fortunately, isotropy and symmetry of the medium drastically reduce the number of independent nonzero components. Also the exact process being described often results in further reductions in the number of independent nonzero components due to permutation symmetries of the susceptibilities. For a discussion on the tensorial nature of the susceptibilities and of the various symmetries which facilitate the reductions in the number of independent nonzero terms, see references [18, 7, 9]. In making this approximation we can further justify the non-vectorial nature of the wave equation (eqn. 1.18) for fields of the same polarisation propagating along the same direction, since in this case the tensorial nature of the susceptibility can be neglected. The wave equation

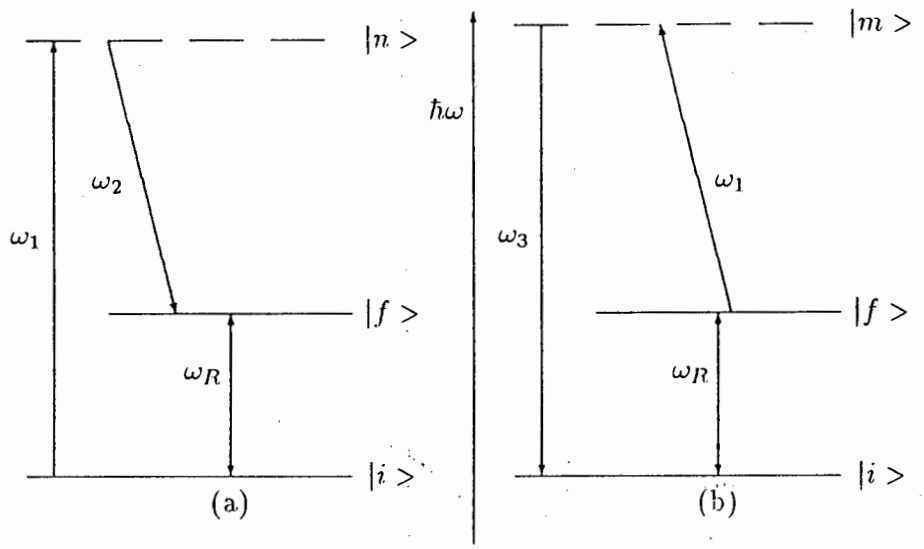

Figure 1.1: Schematic representation of the stimulated Raman scattering process: a) Illustrates the Stokes process and b) illustrates the anti-Stokes process. They are described in detail in the text. It should be noted that $|n>$ and $|m>$ represent virtual states of the system.

becomes:

$$\left(\frac{\partial}{\partial z}+\frac{1}{v}\frac{\partial}{\partial t}\right) E(z,t) = -\frac{2\pi\omega^2}{i\,k\,c^2} P^{(3)}(z,t) \tag{1.19}$$

1.2.1 Classical model of the SRS susceptibility

We now proceed with the specific example of the calculation of the relevant susceptibility for stimulated Raman scattering (SRS). Initially we motivate the form of the required susceptibility by considering the details of the scattering process involved. We follow this up with a classical model enabling evaluation of the susceptibility.

Stimulated Raman scattering can be viewed as the following process with reference to figure 1.1.

A pump field at ω_1 is incident on a medium in an initial state $|i>$. Photons at ω_1 are absorbed by the medium. This process is accompanied by the simultaneous emission of photons at ω_2, leaving the medium in a final state $|f>$. Hence the energy lost is acumulated by the medium. The amount of energy associated with each such event $\hbar\omega_R$ is associated with a transition (be it electronic, vibrational or rotational) of the medium. This is a spontaneous process which will become stimulated when the field at ω_2 becomes sufficiently strong. This emission is termed Stokes radiation since its frequency is down shifted from the that of the pump. If the constituents of the medium are, however, initially in the state $|f>$, then the absorbtion of a photon at ω_1 will be simultaneously accompanied by an emitted photon at ω_3, leaving the medium in a state of lower energy. This emission at ω_3 is termed anti-Stokes radiation since its frequency is upshifted from that of the pump. Naturally it is expected that the anti-Stokes intensity will be less than the Stokes intensity by a factor which is proportional to the population difference of the two states involved. From eqn. 1.16 it is seen that the SRS process is necessarily described by at least a third order susceptibility of the form:

$$\chi_R^{(3)}(\omega_2, \omega_2, \omega_1, -\omega_1) \tag{1.20}$$

These susceptibilities will, in general, consist of resonant and non-resonant terms. The non-resonant terms will, however, be negligible due to resonant enhancement and hence a description of the process will be facilitated by including only the resonant portion. In the remainder of this work we will take the susceptibilities to denote only the resonant part. By quantum mechanical calculation the resonant portion of the stimulated Raman scattering

susceptibility is found to be [18]:

$$\chi_R^{(3)}(\omega_2) = -\frac{N\,|M_{fi}|^2(\rho_i - \rho_f)}{\hbar[(\omega_1 - \omega_2 - \omega_R) - i\Gamma]} \tag{1.21}$$

where N is the density of the constituents of the medium and ρ_i , ρ_f are respectively the populations of the initial and final states. The quantum mechanical matrix element $|M_{fi}|^2$ is often not known or practically too difficult to calculate. For this reason we now present the classical method used by many authors which is based on the method of Placzek [9, 10, 11].

The Polarizability Model

We present a model of SRS in which the process is described as the coupling of three waves, two optical $\vec{E}_1(\omega_1), \vec{E}_2(\omega_2)$ and a material excitation wave described by the oscillation of the normal coordinate $Q(\omega)$. The optical waves are described for identically polarised fields propagating in the z-direction in the electric dipole and slowly varying amplitude approximations by:

$$\left(\frac{\partial}{\partial z} + \frac{1}{v_1}\frac{\partial}{\partial t}\right) E_1(z,t) = i\frac{2\pi\omega_1^2}{k_1 c^2} P_1^{(3)}(z,t)$$

$$\left(\frac{\partial}{\partial z} + \frac{1}{v_2}\frac{\partial}{\partial t}\right) E_2(z,t) = i\frac{2\pi\omega_2^2}{k_2 c^2} P_2^{(3)}(z,t) \tag{1.22}$$

where v_1 and v_2 are the group velocities of the pump and Stokes waves respectively. Since we are interested in SRS due to the $Q(1)$ vibrational transition of hydrogen, we will accordingly restrict ourselves to a dilute molecular medium. The molecules of the medium will be modelled as a set of N harmonic oscillators per unit volume. We consider the oscillation of

the normal coordinate Q of the oscillator in the z-direction in which case the equation of motion is:

$$\left(\frac{\partial^2}{\partial t^2} + 2\Gamma\frac{\partial}{\partial t} + \omega_v^2\right) Q(z,t) = \frac{F(z,t)}{m} \tag{1.23}$$

where 2Γ is the phenomenological damping term corresponding to the width of the Raman transition and ω_v is the natural frequency of vibration. The force driving the oscillation is provided by the beating of the pump and Stokes fields present in the medium. An expression for this force can be obtained by considering the energy per oscillator stored in the medium. This is given by:

$$U = \frac{1}{8\pi N}\vec{E}.\vec{D} = \frac{1}{8\pi N}(1 + N\alpha)\vec{E}.\vec{E} \tag{1.24}$$

where α is known as the polarizability of the medium and the average of the fields, over a few optical cycles, is implied. This polarizability can be expanded as a Taylor series in Q, yielding:

$$\alpha(Q) = \alpha_0 + \left(\frac{\partial\alpha}{\partial Q}\right)_0 Q + \frac{1}{2}\left(\frac{\partial^2\alpha}{\partial Q^2}\right)_0 Q^2 + \ldots \tag{1.25}$$

We drop all terms beyond those first order in Q as these are responsible for multiphonon processes. Substitution into eqn. 1.24 gives:

$$U = \frac{1}{8\pi N}\left(1 + N\left[\alpha_0 + \left(\frac{\partial\alpha}{\partial Q}\right)_0 Q\right]\right)\vec{E}.\vec{E} \tag{1.26}$$

for the stored energy per oscillator. Hence the force exerted per oscillator is:

$$F = \frac{\partial U}{\partial Q} = \frac{1}{8\pi}\left(\frac{\partial\alpha}{\partial Q}\right)_0 \vec{E}.\vec{E} \tag{1.27}$$

Now writing the fields as

$$\vec{E}_j(z,t) = \hat{e}\, E_j(z,t)e^{i(k_j z - \omega_j t)} \tag{1.28}$$

where the E_j are complex amplitudes, enables us to identify the beating of the fields as the origin of the force which drives the molecular vibrations. Then $(\frac{\partial \alpha}{\partial Q})_0$ can be seen as the coupling constant which, when nonzero, facilitates the energy exchange between the fields and the molecular vibration. It should be noted at this stage that the correspondence principle enables a quantum mechanical version of this model to be used [7].

If we have

$$Q(z,t) = A(z,t)e^{i(kz-\omega t)}$$

where $A(z,t)$ is a complex amplitude and we again use the slowly varying amplitude approximation together with the fact that $\omega_v \gg \Gamma$, then equation 1.23, describing the molecular vibration becomes:

$$\left[2i\omega\left(\frac{\partial}{\partial t}+\Gamma\right)+(\omega_v^2-\omega^2)\right]A(z,t) = \frac{-1}{16\pi m}\left(\frac{\partial \alpha}{\partial Q}\right)_0 E_1(z,t)E_2^*(z,t) \quad (1.29)$$

where the extra factor of $1/2$ comes from the averaging of the fields and $\omega = \omega_1 - \omega_2$ is the driven frequency. This does not necessarily equal the natural frequency ω_v. If we write

$$\omega_v = \omega + \Delta\omega$$

and use the fact that $\Delta\omega \ll \omega$ then the equation governing the amplitude of the molecular vibration becomes:

$$\left(\frac{\partial}{\partial t}+\Gamma - i(\omega_v-\omega)\right)A(z,t) = \frac{i}{(4\pi)8m\omega_v}\left(\frac{\partial \alpha}{\partial Q}\right)_0 E_1(z,t)E_2^*(z,t) \quad (1.30)$$

When in fact $\omega = \omega_v$ does hold, we say that it is on resonance. We initially restrict our considerations to this case with a steady state response of the medium. The amplitude of the molecular vibration is therefore given by:

$$A(z,t) = \frac{i}{(4\pi)8m\omega_v\Gamma}\left(\frac{\partial \alpha}{\partial Q}\right)_0 E_1(z,t)E_2^*(z,t) \quad (1.31)$$

in which the material excitation is described by the density matrix element $\rho^2_{if}(\omega)$. In this case the nonlinear polarisations are described, in terms of this matrix element, by

$$\vec{P}^{(2)}(\omega_2) = -NM_{fi}\vec{E}_1\rho^{(2)}_{if}(\omega_2 - \omega_1) \tag{2.2}$$

If we rewrite the propagating material excitation as:

$$\rho_{fi}(\omega_1 - \omega_2) = A(z,t)e^{i(k_1-k_2)z-i(\omega_1-\omega_2)t}$$

in analogy with $Q(z,t)$ in Chapter 1 (see page 16). Then in the density matrix formalism SRS is described by:

$$\begin{aligned}
\left(\frac{\partial}{\partial z} + \frac{1}{v_2}\frac{\partial}{\partial t}\right) E_2(z,t) &= i\left(\frac{2\pi\omega_2^2}{k_2c^2}\right) NM_{fi}E_1(z,t)A^*(z,t) \\
\left(\frac{\partial}{\partial z} + \frac{1}{v_1}\frac{\partial}{\partial t}\right) E_1(z,t) &= i\left(\frac{2\pi\omega_1^2}{k_1c^2}\right) NM^*_{fi}E_2(z,t)A(z,t) \\
\left(\frac{\partial}{\partial t} + \Gamma\right) A^*(z,t) &= \frac{-i}{\hbar}M^*_{fi}(\rho_i - \rho_f)E^*_1(z,t)E_2(z,t)
\end{aligned} \tag{2.3}$$

which are the analogous coupled equations of eqn. 1.22 and eqn. 1.30 in the polarisability model. It should be noted, however, that the population difference $(\rho_i - \rho_f)$ should in general (from physical argument) obey the relaxation equation [18]:

$$\left(\frac{\partial}{\partial t} + \frac{1}{T_1}\right)[(\rho_i - \rho_f) - (\rho_i - \rho_f)_0] = 2\frac{dW_{fi}}{N\,d\omega_2}(\rho_i - \rho_f) \tag{2.4}$$

for a two level system, where $\frac{dW_{fi}}{d\omega_2}(\rho_i - \rho_f)$ is the transition rate between the levels. In general, this equation should be solved together with eqn. 2.3 (cf ref [12]). Under weak excitation $(\rho_i - \rho_f)$ can, however, be replaced by its equilibrium (thermal) distribution.

Following the procedure of section 1.2.1 for a steady state material excitation 'on' resonance, we obtain the following definition for the stimulated Raman susceptibility:

$$\chi_R^{(3)} = \frac{N|M_{fi}|^2}{i\hbar\Gamma}(\rho_i - \rho_f) \tag{2.5}$$

By comparing this with the previous definition (eqn. 1.36) from the polarisability model enables the matrix elements $|M_{fi}|^2$ to be evaluated.

Now that we are satisfied that the material excitation can be treated quantum mechanically, we proceed with the classical polarisability model for the duration of this work. The coupled equations to be used are therefore eqn. 1.22 and eqn. 1.30 which we requote below for convenience.

$$\begin{aligned}
\left(\pm\frac{\partial}{\partial z} + \frac{1}{v_2}\frac{\partial}{\partial t}\right) E_2(z,t) &= i\frac{N}{4\pi}\left(\frac{2\pi\omega_2^2}{k_2c^2}\right)\left(\frac{\partial\alpha}{\partial Q}\right)_0 E_1(z,t)A^*(z,t) \\
\left(\frac{\partial}{\partial z} + \frac{1}{v_1}\frac{\partial}{\partial t}\right) E_1(z,t) &= i\frac{N}{4\pi}\left(\frac{2\pi\omega_1^2}{k_1c^2}\right)\left(\frac{\partial\alpha}{\partial Q}\right)_0 E_2(z,t)A(z,t) \\
\left(\frac{\partial}{\partial t} + \Gamma + i(\omega_v - \omega)\right) A^*(z,t) &= \frac{-i}{(4\pi)8m\omega_v}\left(\frac{\partial\alpha}{\partial Q}\right)_0 E_1^*(z,t)E_2(z,t)
\end{aligned} \tag{2.6}$$

It should be noted that our description of the Stokes field now includes the case of a backward propagating wave as evidenced by the $\pm$ sign in the above equation. The minus sign, describing the backscattered wave, is obtained by replacing the propagation vector by $-\vec{k}_2$. It should be noted that we have neglected the possibility of higher order SRS. This can occur when the first Stokes output becomes sufficiently intense so that it acts as the pump in the generation of second Stokes output by stimulated Raman scattering.

2.2 Steady State Theory

In the steady state approximation of constant field amplitudes, the time derivatives are zero and the equations describing the spatial propagation of the field amplitudes through the medium are:

$$\begin{aligned}
\frac{\partial}{\partial z}E_1(z) &= i\frac{N}{4\pi}\left(\frac{2\pi\omega_1^2}{k_1c^2}\right)\left(\frac{\partial\alpha}{\partial Q}\right)_0 E_2(z)A(z) \\
\pm\frac{\partial}{\partial z}E_2(z) &= i\frac{N}{4\pi}\left(\frac{2\pi\omega_2^2}{k_2c^2}\right)\left(\frac{\partial\alpha}{\partial Q}\right)_0 E_1(z)A^*(z) \\
A^*(z) &= \frac{-i}{(4\pi)8m\omega_v\Gamma}\left(\frac{\partial\alpha}{\partial Q}\right)_0 E_1^*(z)E_2(z)
\end{aligned} \tag{2.7}$$

where from Chapter 1, eqn. 1.36 defines the Raman susceptibility which we restate below:

$$\chi_R^{(3)}(\omega_2) = \frac{-iN\left(\frac{\partial\alpha}{\partial Q}\right)_0^2}{(4\pi)^2 8m\omega_v\Gamma} \tag{2.8}$$

This yields upon substitution of $A^*(z)$ into the two field equations:

$$\begin{aligned}
\frac{\partial}{\partial z}E_1(z) &= i\left(\frac{2\pi\omega_1^2}{k_1c^2}\right)\chi_R^{(3)^*}|E_2|^2E_1(z) \\
\pm\frac{\partial}{\partial z}E_2(z) &= i\left(\frac{2\pi\omega_2^2}{k_2c^2}\right)\chi_R^{(3)}|E_1|^2E_2(z)
\end{aligned} \tag{2.9}$$

where equation 1.37 has been used. These equations describe the steady state solution to the coupled wave equations. As before the plus (minus) sign denotes a forward (backward) propagating wave.

2.2.1 Non-depletion of the Pump

Neglecting depletion of the pump simplifies things further in that the solution is obtained by solving only the second of the above equations. The solution is easily shown to be:

$$E_F(z) = E_0 e^{iK_1 z}$$

$$E_B(z) = E_0 e^{iK_1(L-z)} \tag{2.10}$$

for the forward and backward propagating waves respectively, assuming that the boundary conditions $E_F(0) = E_0$ and $E_B(L) = E_0$ hold. By a simple coordinate shift in the case of the backward solution, it is seen that both the forward and backward waves are described by the first equation above [11, 10]. It should be noted that the identification

$$K_1 = \left(\frac{2\pi\omega_2^2}{k_2 c^2}\right)\chi_R^{(3)}|E_1|^2$$

has been made. The full expression for the SRS field of the forward propagating wave is:

$$\vec{E}_2(z,t) = \hat{e}_2 E_2 e^{iK_1 z} e^{i(\omega t - kz)} \tag{2.11}$$

Naturally the discussion to follow holds also for the backward propagating wave as long as the propagation vector has its sign reversed. By separating K_1 into its real and imaginary parts, it is seen that the imaginary part affects the amplitude of the wave while the real portion results in a change in the propagation vector.

$$\vec{E}_2(z,t) = \hat{e}_2 E_0 e^{-Im(K_1)z} e^{i[\omega t - (k - Re(K_1))z]}$$

The quantity of interest here as far as measurement is concerned is the intensity. This is obtained by multiplying the above expression by its complex congugate, yielding:

$$I(z) = I_0 e^{-2Im(K_1)z} \tag{2.12}$$

Using the previously given expression for K_1, and noting that the imaginary part of the susceptibility is negative (see eqn. 2.8) shows that the above equation for the intensity of the SRS beam is one of exponential gain. The *steady state Raman gain* is then defined by:

$$g = -2Im(K_1) = -\left(\frac{4\pi\omega_2^2}{k_2 c^2}\right) Im\chi_R^{(3)} |E_1|^2 \tag{2.13}$$

resulting in the well-known equation for describing the steady state SRS process in the absence of pump depletion:

$$I(z) = I_0 e^{gz} \tag{2.14}$$

2.2.2 Spontaneous Initiation

The above description of SRS is valid when the fields can be treated classically. This means that a description of SRS which is built up from spontaneous Raman scattering (noise) is not facilitated. A full quantum mechanical description of SRS which treats both the buildup and evolution of the SRS in a unified way has been presented [17]. We will, however, restrict ourselves to a semi-classical treatment by the rate equation model. Comparison with the result of the unified treatment will yield the correct interpretation of the quantities.

We consider spontaneous Raman scattering which produces Stokes photons which act as the source for stimulated Raman growth. The Stokes

emission intensity $I_2(z)$ in the steady state obeys to a good approximation the phenomenological rate equation:

$$\frac{\partial I_2(z)}{\partial z} = N\sigma_{sp} I_1 + g I_2(z) \tag{2.15}$$

Since $I_2(0) = 0$ (spontaneous initiation), the solution is easily shown to be given by:

$$I_2(z) = \frac{I_1 N \sigma_{sp}}{g}(e^{gz} - 1) \tag{2.16}$$

where σ_{sp} is the spontaneous Raman scattering cross-section, N is the population density and g is the steady state Raman gain. This can be compared with the result of the unified treatment [17], which yields:

$$I_2(z) = \frac{\Gamma\hbar\omega_2}{2A}(e^{gz} - 1) \tag{2.17}$$

where A is the cross-sectional area of the interaction region of length L. It is seen that this reduces to the previous result (eqn. 2.14) even for small gains, when the identification $I_0 = \frac{1}{2}\Gamma\hbar\omega_2/A$ is made. Here Γ is the halfwidth of the Raman transition. Raymer et al. [17] give a more general result where the finite diameter of the pump is taken into account by considering a pencil-shaped interaction region of area A and length L with $A \ll L^2$. The Stokes intensity is then given by :

$$I_2(z) = \left(\frac{A}{\lambda_2 L}\right)^2 \frac{\Gamma\hbar\omega_2}{2A}(e^{gz} - 1) \tag{2.18}$$

so that the source term in eqn. 2.14 can be identified as:

$$I_2(0) = \left(\frac{A}{\lambda_2 L}\right)^2 \frac{\Gamma\hbar\omega_2}{2A} \tag{2.19}$$

This identification enables SRS initiated by spontaneous Raman scattering to be described by the same equation (2.14) as before.

2.2.3 Spectral Distribution with Undepleted Pump

In a simplistic way we can show that the SRS output should be gain narrowed [11]. If we relax the condition of 'on' resonance, then in the steady state it is seen from eqn. 1.30 that:

$$A^*(z) = \frac{\left(\frac{\partial\alpha}{\partial Q}\right)_0}{(4\pi)8m\omega_v} \frac{1}{(\omega_2 - \omega_1 + \omega_v + i\Gamma)} E_1^*(z)E_2(z) \tag{2.20}$$

Substituting this form of $A(z)$ into equation 2.7 yields after a little manipulation:

$$\frac{\partial}{\partial z}E_1(z) = i\left(\frac{2\pi\omega_1^2}{k_1c^2}\right)\chi_R^{(3)}\frac{i\Gamma}{(\Delta\omega - i\Gamma)}|E_2|^2E_1(z)$$

$$\pm\frac{\partial}{\partial z}E_2(z) = i\left(\frac{2\pi\omega_2^2}{k_2c^2}\right)\chi_R^{(3)}\frac{i\Gamma}{(\Delta\omega + i\Gamma)}|E_1|^2E_2(z) \tag{2.21}$$

where we have used $(\omega_2 - \omega_1) - \omega_v = \Delta\omega$. Again the forward and backward solutions will be identical (with a shift of coordinates) and hence the $\pm$ sign will be dropped. We now define the Raman susceptibility χ' for this the 'off' resonance case as:

$$\chi' = \frac{i\Gamma}{(\Delta\omega + i\Gamma)}\chi_R^{(3)}$$

This is seen to reduce to the 'on' resonance susceptibility $\chi_R^{(3)}$ when $\Delta\omega = 0$. This can be rewritten as:

$$\chi' = i\chi_R^{(3)}\frac{\Gamma(\Delta\omega - i\Gamma)}{(\Delta\omega^2 + \Gamma^2)} \tag{2.22}$$

In the case where pump depletion is neglected, this coupled system becomes uncoupled and SRS is described by:

$$\frac{\partial}{\partial z}E_2(z) = i\left(\frac{2\pi\omega_2^2}{k_2c^2}\right)\chi'|E_1|^2E_2(z) \tag{2.23}$$

yielding a solution

$$E_2(z) = E_0 e^{iK_1' z}$$

where

$$K_1' = \left(\frac{2\pi\omega_2^2}{k_2 c^2}\right)\chi'|E_1|^2 = K_1 \frac{i\Gamma}{(\Delta\omega + i\Gamma)}$$

The imaginary part of K_1' and hence the susceptibility χ' is as before responsible for the gain experienced by the Raman scattered beam. The Raman gain for this case is obtained by using the relationship between the imaginary parts of these two expressions

$$Im\chi' = Im\chi_R^{(3)} \frac{\Gamma^2}{(\Delta\omega^2 + \Gamma^2)}$$

to replace $\chi_R^{(3)}$ in equation 2.13, giving

$$g' = \left(\frac{4\pi\omega_2^2}{k_2 c^2}\right) \frac{Im\chi_R^{(3)}}{\left(\left(\frac{\Delta\omega}{\Gamma}\right)^2 + 1\right)} |E_1|^2 \tag{2.24}$$

Using equation 2.13, this simplifies to:

$$g' = \frac{g}{\left(\left(\frac{\Delta\omega}{\Gamma}\right)^2 + 1\right)}$$

It is evident from this expression that the gain has a Lorentzian distribution. The output intensity in this case is found by replacing the gain g in equation 2.14 by the above expression , giving

$$I(z) = I_0 e^{\frac{gz}{((\Delta\omega/\Gamma)^2+1)}} \tag{2.25}$$

This expression allows the frequency dependence of the SRS output to be investigated by fixing the gain length $gz = gl$ (l is the interaction length).

If this is done then the above equation can be rewritten as a function of the frequency mismatch.

$$I(\Delta\omega) = I(0)e^{\frac{-gl}{((\Gamma/\Delta\omega)^2+1)}} \tag{2.26}$$

It is of interest here to obtain an expression for the expected linewidth (HWHM) of the SRS output. Limiting the mismatch to be much smaller than the spontaneous Raman scattering linewidth: $\Delta\omega \ll \Gamma$ enables the following expression for the output linewidth to be obtained [11]:

$$\Delta\omega_{\frac{1}{2}} \simeq \sqrt{\frac{ln2}{gl}}\Gamma \tag{2.27}$$

From this it is evident that the SRS linewidth is gain narrowed. In the case where depletion of the pump is neglected but the correct temporal response of the medium is included, the solution for input fields of arbitrary bandwidth will also be shown to reduce, in the case of a monochromatic pump and a broadband Stokes input, to the above result [16]. It can also be shown that SRS built up from noise is equivalent to the case of a weak broadband input Stokes field [17]. Hence the above result is seen to be quite general when the pump field is treated as constant.

2.2.4 Solution with pump depletion

We return to the general steady state solution 2.9. If we multiply the equation for E_l by E_l^* and add its complex conjugate equation, we obtain:

$$E_l^*\frac{\partial}{\partial z}E_l + E_l\frac{\partial}{\partial z}E_l^* = i(-1)^l\left(\frac{2\pi\omega_l^2}{k_l c^2}\right)|E_1|^2|E_2|^2\left[\chi_R^{(3)} - \chi_R^{(3)*}\right]$$

where $l = 1, 2$ for the laser and Stokes waves respectively. This results in:

$$\frac{\partial}{\partial z}|E_1|^2 = \left(\frac{4\pi\omega_1^2}{k_1 c^2}\right) Im\chi_R^{(3)}|E_2|^2|E_1|^2$$

$$\frac{\partial}{\partial z}|E_2|^2 = -\left(\frac{4\pi\omega_2^2}{k_2c^2}\right) Im\chi_R^{(3)}|E_1|^2|E_2|^2 \tag{2.28}$$

Recalling that $k = \frac{n\omega}{c}$, where n is the refractive index of the medium, enables the equations to be rewritten as:

$$\frac{n_l}{\omega_l}\frac{\partial}{\partial z}|E_l|^2 = (-1)^{l-1}\frac{4\pi}{c} Im\chi_R^{(3)}|E_1|^2|E_2|^2$$

so that adding the two equations (for $l = 1, 2$) yields:

$$\frac{\partial}{\partial z}\left(\frac{n_1}{\omega_1}|E_1(z)|^2 + \frac{n_2}{\omega_2}|E_2(z)|^2\right) = 0 \tag{2.29}$$

which is the Manley-Rowe relation, expressing the conservation of the total number of photons. More explicitly this gives:

$$\frac{n_1}{\omega_1}|E_1(z)|^2 + \frac{n_2}{\omega_2}|E_2(z)|^2 = \frac{n_1}{\omega_1}|E_1(0)|^2 + \frac{n_2}{\omega_2}|E_2(0)|^2 = N \tag{2.30}$$

for a constant N. Using this, we can eliminate $|E_1(z)|^2$ from the equation for $|E_2|^2$ in (2.28), yielding:

$$\frac{\partial}{\partial z}|E_2|^2 = -\left(\frac{4\pi\omega_2^2}{k_2c^2}\right) Im\chi_R^{(3)}|E_2|^2[N - \frac{n_2}{\omega_2}|E_2|^2]\frac{\omega_1}{n_1} \tag{2.31}$$

Defining G by the relationship

$$G|E_1(0)|^2 = g \tag{2.32}$$

where g is the steady state Raman gain defined by eqn. 2.13, enables the equation to be rewritten as:

$$\frac{\partial}{\partial z}|E_2|^2 = G\frac{\omega_1}{n_1}[N|E_2|^2 - \frac{n_2}{\omega_2}|E_2|^4] \tag{2.33}$$

This is a Bernoulli differential equation in $|E_2|^2$. Defining $A = \frac{1}{|E_2|^2}$ enables the above equation to be reduced to

$$\frac{\partial}{\partial z}A(z) + NG\frac{\omega_1}{n_1}A(z) = -G\frac{n_2}{\omega_2}\frac{\omega_1}{n_1} \tag{2.34}$$

which can be solved with the help of the integration factor $e^{NG\frac{\omega_1}{n_1}z}$, yielding:

$$A(z) = \frac{n_2}{\omega_2}\frac{1}{N} + \left[A(0) - \frac{n_2}{\omega_2}\frac{1}{N}\right] e^{-GN\frac{\omega_1}{n_1}z} \tag{2.35}$$

A similar equation can be found for $|E_1(z)|^2$. The solutions can then be found to be [18]:

$$\begin{aligned}
\frac{|E_1(z)|^2}{|E_1(z)|^2 - \frac{\omega_1}{n_1}N} &= \frac{|E_1(0)|^2}{|E_1(0)|^2 - \frac{\omega_1}{n_1}N} e^{-GN\frac{\omega_1}{n_1}z} \\
\frac{|E_2(z)|^2}{|E_2(z)|^2 - \frac{\omega_2}{n_2}N} &= \frac{|E_2(0)|^2}{|E_2(0)|^2 - \frac{\omega_2}{n_2}N} e^{GN\frac{\omega_1}{n_1}z}
\end{aligned} \tag{2.36}$$

It is easily shown that this solution may be written in the form of energy transmission fractions $T(z)$ as [19, 20]:

$$\begin{aligned}
T_1(z) &= \frac{|E_1(z)|^2}{|E_1(0)|^2} = \frac{1+\delta}{\delta + e^{\alpha z}} \\
T_2(z) &= \frac{|E_2(z)|^2}{|E_2(0)|^2} = \frac{1+\delta}{1+\delta e^{-\alpha z}}
\end{aligned} \tag{2.37}$$

Where $\alpha = GN\frac{\omega_1}{n_1}$ is the steady state gain with pump depletion and

$$\delta = \frac{\frac{n_1}{\omega_1}|E_1(0)|^2}{\frac{n_2}{\omega_2}|E_2(0)|^2} \tag{2.38}$$

is the input intensity ratio. These solutions are illustrated in figure 2.1 which clearly shows the initially exponential gain of the Stokes signal with the concomitant depletion of the pump.

We proceed to analyse the physical meaning of this result in terms of the input intensity ratio δ, and the ratio between the exponential gain and the input intensity ratio x, where

$$x\delta = e^{gz} \tag{2.39}$$

This exhibits the expected result for low gain as long as other processes can be neglected.

1*b*) $x \gg 1$, which represents the high gain limit in this case.

The intensity transmissions in this limit are seen to be given by:

$$\frac{I_1(z)}{I_1(0)} \simeq (1+\delta)e^{-\alpha z} \qquad \frac{I_2(z)}{I_2(0)} \simeq 1+\delta \tag{2.41}$$

The second of these can be rewritten in the more useful form:

$$I_2(z) \simeq I_2(0) + \frac{\omega_2}{\omega_1} I_2(0)$$

This solution illustrates the exponential loss experienced by the pump as well as the fact that all of the pump photons can in theory be converted into Stokes photons. In reality this will be approached for a sufficiently long interaction length [19, 21].

2) $\delta \gg 1$. This case is the most interesting, representing the buildup of Raman intensity from weak Raman input. It is thus known as the small signal case. The limiting forms for this case are most easily obtained from the following form of the solution (i.e. eqn. 2.37)

$$\frac{I_1(z)}{I_1(0)} \simeq \frac{\delta}{\delta + e^{\alpha z}}$$

$$\frac{I_2(z)}{I_2(0)} \simeq \frac{\delta}{1 + \delta e^{-\alpha z}}$$

In this case there is no simple correspondence between the various gain limits and the parameter x. This will become apparent below.

2*a*) $x \ll 1$, treats the situation of variable gain in this case. The resulting intensity transmissions are given by:

$$\frac{I_1(z)}{I_1(0)} \simeq 1 \qquad \frac{I_2(z)}{I_2(0)} \simeq e^{\alpha z} \tag{2.42}$$

This is the solution obtained when pump depletion was neglected (see eqn. 2.14 and note that $\alpha \rightarrow g$). It is thus obvious that high gain is also represented here i.e. $e^{\alpha z} \gg 1$ as long as δ is sufficiently bigger than $e^{\alpha z}$ so that the condition, $x \ll 1$ is maintained. Hence even for high gains the assumption of a constant pump may be made as long as these conditions are upheld.

2*b*) $x \simeq 1$, again represents a situation with variable gain, although here the gain can not be considered as low since $x \simeq 1 \Rightarrow e^{\alpha z} \gg 1$. This is evident from the resulting intensity transmissions (below), where the magnitude of the resulting gain is seen to depend crucially on the size of the input intensity ratio. It should be noted, however, that in the case of growth from spontaneous emission, the input intensity ratio will be very large and hence this will represent a situation with high gain. Also, as noted before, this is more a particular evaluation rather than a limiting case.

$$\frac{I_1(z)}{I_1(0)} \simeq \frac{1}{2} \qquad \frac{I_2(z)}{I_2(0)} \simeq \frac{1}{2}\delta \Rightarrow I_2(z) \simeq \frac{1}{2}\frac{\omega_2}{\omega_1} I_1(0) \tag{2.43}$$

Here the pump is depleted to half its original level, while all the lost pump photons are converted into Stokes photons.

2*c*) $x \gg 1$, represents the high gain limit regardless of the size of the input intensity ratio δ. The resultant intensity transmissions below, indicate that the pump has been completely depleted with all of its photons being converted into Stokes photons.

$$\frac{I_1(z)}{I_1(0)} \simeq \delta e^{-\alpha z} \ll 1 \qquad \frac{I_2(z)}{I_2(0)} \simeq \delta \Rightarrow I_2(z) \simeq \frac{\omega_2}{\omega_1} I_1(0) \tag{2.44}$$

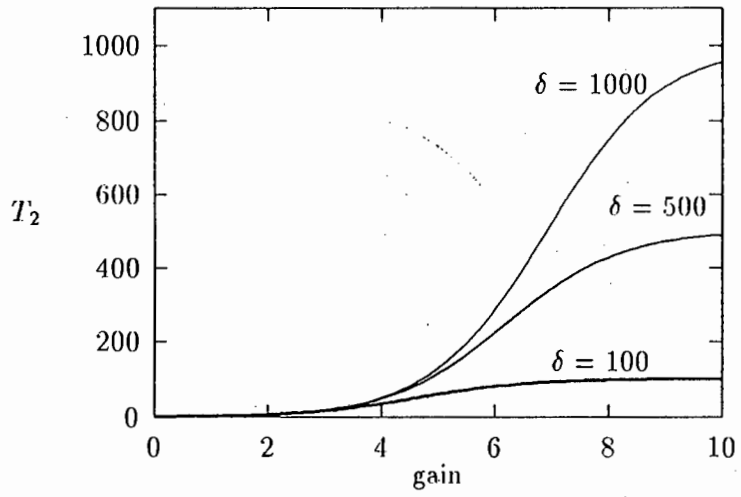

Figure 2.2: Illustrates the Stokes intensity ratio for various input intensity ratios, as a function of the gain. The general trends of case 2) $\delta \gg 1$ are evident. The region of small gain (i.e. $x \ll 1$) corresponds to the area close to the origin. Recall that this will only be valid provided we do not approach the region where the solution neglecting pump depletion is valid. The region $x \simeq 1$, corresponds roughly to the position where T_2 takes on half its maximum value. The position of this region as well as the position of the region where saturation occurs (i.e. $x \gg 1$ or the region of high gain), is seen to vary depending on the input intensity ratio.

These trends can be seen in figure 2.2 in which the relationship between the region of validity of the above limits and the input intensity ratio is illustrated. It should be noted that for the cases considered here (i.e. $\delta = 1000$ and $\delta = 100$), the identification of the gain with the parameter x is valid.

Of interest now is to examine the spectral distribution of the Stokes output in each of these cases. I am unaware of a detailed investigation into the spectral distribution of the Stokes output where depletion of the pump is included.

2.2.5 Spectral Distribution with Pump Depletion

The output intensity of the SRS in the case where pump depletion is allowed for, is given by:

$$I_2(z) = I_2(0)\frac{1+\delta}{1+\delta e^{-\alpha' z}} \tag{2.45}$$

where the gain α' is defined, in analogy with that of section (2.2.3) (see eqn. 2.24), as:

$$\alpha' = \frac{\alpha}{\left(\frac{\Delta\omega}{\Gamma}\right)^2 + 1} \tag{2.46}$$

The intensity can be written as a function of frequency mismatch instead of position, yielding:

$$I_2(\Delta\omega) = I_0\frac{1+\delta e^{-\alpha z}}{1+\delta e^{-\alpha' z}} \tag{2.47}$$

where $I_0 = I_2(\Delta\omega = 0)$. The halfwidth of this distribution is easily shown to be given by:

$$\Delta\omega_{\frac{1}{2}} = \Gamma\sqrt{\frac{\alpha z}{\ln(\frac{\delta}{1+2\delta e^{-\alpha z}})} - 1} \tag{2.48}$$

We now examine the limiting forms of the halfwidth for the five cases considered above. It should be noted that we have modelled monochromatic input beams (pump and Stokes) with the output spectrum arising due to mixing with a material excitation of finite width (Raman transition width). The expression for the halfwidth may be rewritten in terms the parameter x as:

$$\Delta\omega_{\frac{1}{2}} = \Gamma\sqrt{\frac{\alpha z}{\ln(\frac{\delta}{1+2/x})} - 1}$$

Due to the form of the logarithm in this equation, only the limiting forms of the parameter x are seen to simplify the expression for the halfwidth.

1a) $\delta > 1$, $x \simeq 1$, i.e. low gain for input Stokes signal less than pump. Again, this case constitutes the evaluation at a particular gain satisfying these conditions. The halfwidth in the vicinity of this point is given by:

$$\Delta\omega_{\frac{1}{2}} \simeq \Gamma\sqrt{\frac{\ln 3}{\ln\delta - \ln 3}} \tag{2.49}$$

This is not a very interesting case. Of more interest is the high gain limit which is treated next.

1b) $\delta > 1$, $x \gg 1$, which is the high gain limit. In this case the halfwidth becomes:

$$\Delta\omega_{\frac{1}{2}} \simeq \Gamma\sqrt{\frac{\ln x}{\alpha z - \ln x}} = \Gamma\sqrt{\frac{\ln x}{\ln\delta}} \tag{2.50}$$

which implies that the SRS width is broadened.

The validity of this limiting form can be gauged from figure 2.3 in which it is plotted together with the exact expression for the halfwidth, given by eqn. 2.48. The cases of most interest to us are, however, those in which the input Stokes intensity is much less than that of the pump, i.e. small signal. This includes the situation of SRS generation from noise (see section (2.2.2)).

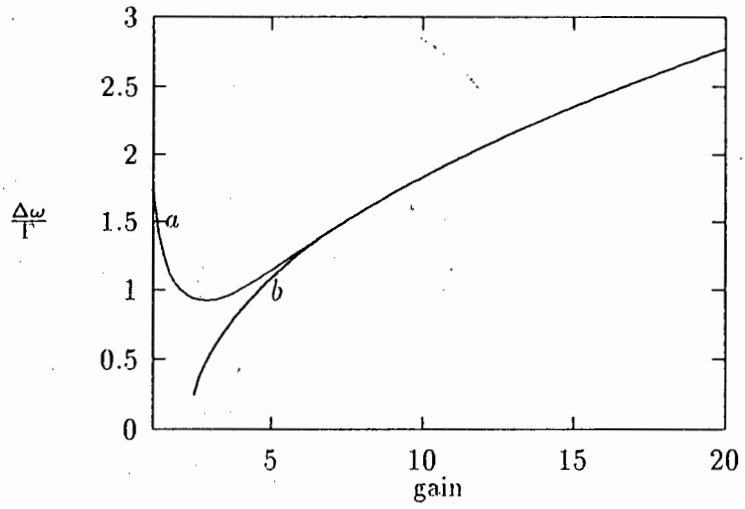

Figure 2.3: illustrates the correspondence between the limiting forms of the halfwidth: *b*) $x \gg 1$ and the exact expression (labelled *a*) for the case 1) $\delta = 10$.

2) $\delta \gg 1$. The halfwidth in this case can take on three different limiting forms depending on the parameter x.

2a) $x \ll 1 \Rightarrow \alpha z \geq 0$, and as before describes the situation of variable gain in this case. The linewidth is given by:

$$\Delta\omega_{\frac{1}{2}} \simeq \Gamma\sqrt{\frac{\ln 2}{\alpha z - \ln 2}} \tag{2.51}$$

In general it can be seen that the halfwidth is of the order of the width of the spontaneous transition. It is evident that for $\alpha z > 2\ln 2$ we start obtaining a gain narrowed output. In the case of high gain, this is seen to reduce to the expression obtained when pump depletion was neglected (i.e. eqn. 2.27), as expected.

2b) $x \simeq 1 \Rightarrow e^{\alpha z} \simeq \delta \gg 1$. Here the halfwidth in this vicinity is given by the expression obtained in case 1a). However, in this case, situations of higher gain are allowed so that gain narrowing is certainly experienced for high enough gains (i.e. for $\ln\delta > 2\ln 3$). In the case of high gain, the expression for the halfwidth, eqn. 2.49 reduces to:

$$\Delta\omega_{\frac{1}{2}} \simeq \Gamma\sqrt{\frac{\ln 3}{\ln\delta}} \tag{2.52}$$

which clearly exhibits gain narrowing.

2c) $x \gg 1 \Rightarrow e^{\alpha z} \gg \delta \gg 1$, which therefore represents the high gain limit. Here the general expression for the halfwidth is seen to reduce to that in 1b) above, which in this case is more conveniently written as:

$$\Delta\omega_{\frac{1}{2}} \simeq \Gamma\sqrt{\frac{\alpha z}{\ln\delta} - 1} \tag{2.53}$$

Now $\delta \gg 1$ and $x \gg 1$ imply that $e^{\alpha z} \gg \delta \gg 1$, and hence $\alpha z > \ln\delta$. Thus from the above expression for the halfwidth it is evident that there is gain narrowing of the linewidth provided $\alpha z < 2\ln\delta$ i.e. $e^{\alpha z} < \delta^2 \Rightarrow x < \delta$. This

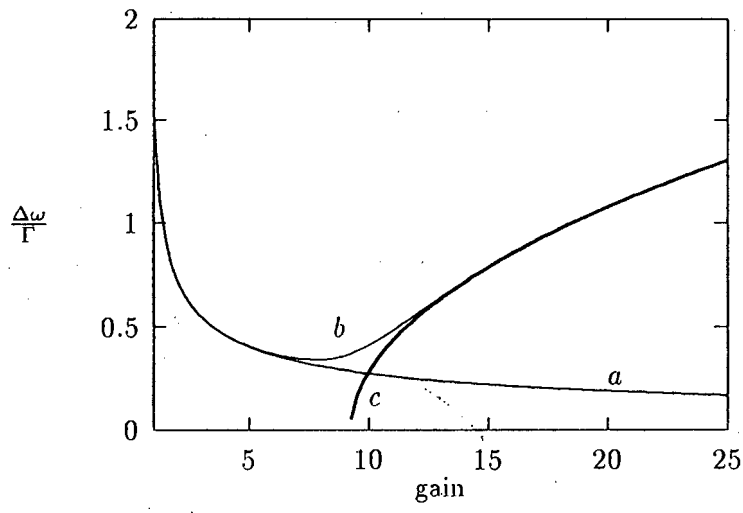

Figure 2.4: illustrates the correspondence between the limiting forms of the halfwidth: *a*) $x \ll 1$, *c*) $x \gg 1$ and the exact expression (labelled *b*) for the case 2) $\delta = 10000$

means that the narrowest SRS linewidth is achieved when δ and $e^{\alpha z}$ are as large as possible and x is as small as the condition $x \gg 1$ will allow. This is evident from eqn. 2.50.

The validity of these limiting forms can be gauged from figure 2.4 in which they are plotted together with the exact expression for the halfwidth, given by eqn. 2.48.

Since this is the case of interest, we will also investigate the effect of pressure (in the case of a gaseous medium) on the Stokes halfwidth. In this case we have

$$\alpha \simeq g = G\,|E_1(0)|^2$$

The pressure dependence arises since both the spontaneous Raman linewidth and the Raman gain (through N and Γ in eqn. 2.8) depend on the pressure of the gain medium. Finally, if we are also considering the case of SRS generation, then from eqn. 2.17 of section 2.2.2 it is evident that the input intensity ratio has a pressure dependence.

Various models of the dependence on pressure of the spontaneous Raman scattering linewidth have been constructed [13, 14, 15]. The basic model to be used is that of Bischel et al. [15], where

$$\Gamma_{FWHM} = A/\rho + B\rho \tag{2.54}$$

is the relevant relationship. Here ρ is the density in Amagats, A is proportional to the self diffusion coefficient of ref. [14], and B is the pressure broadening coefficient. For the $Q(1)$ vibration of hydrogen the coefficients are given at $T = 298\,K$ by:

$$A = 309 \pm 11\ MHz.Amagat$$

$$B = 52.2 \pm 0.5\ MHz/Amagat$$

and

$$\rho(\text{in } Amagat) = \tfrac{T_0}{T} P(\text{in } atm) \tag{2.55}$$

where T_0 is the temperature of the hydrogen. Using this together with the fact that $N \propto \rho$ enables the linewidth as a function of pressure to be

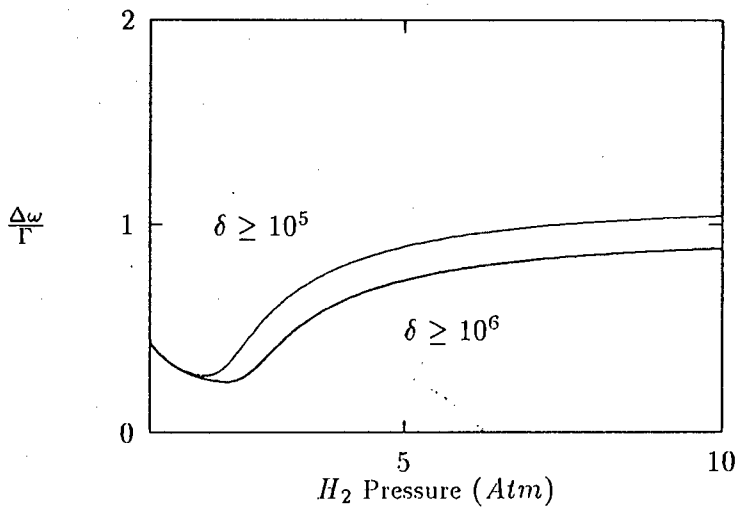

Figure 2.5: For a fixed laser intensity and for $\delta \geq 10^5$ and $\delta \geq 10^6$, the linewidths of the SRS output is plotted as a function of pressure

found. The result at a constant pump intensity ($I_1 = 10\ GW/cm^2$) and with $\delta \geq 10^5$, is plotted in fig. 2.5. It should be noted that as the input intensity ratio δ increases, the linewidth ratio $\frac{\Delta\omega}{\Gamma}$ remains less than unity for increasingly higher pressures. Since this trend occurs at a fixed gain, this seems to imply that the pump is responsible for the gain narrowing effect. This is substantiated by the behaviour illustrated in fig. 2.3 and 2.1 in which the linewidth of the output is seen to be narrowest at the region where the pump starts to become depleted, i.e. depleted pump is accompanied by an increase in the linewidth of the SRS output.

Often experiments are performed with a focused pump beam. This will obviously complicate the above discussion. Focusing will be dealt with in the following section. Its importance in decoding the forward/backward gain

anomaly will be discussed in section 2.4.

2.3 SRS with Focused Beams

The plane wave theory presented up till now is not able to describe accurately the situation of real beams which are of 'finite' cross-sectional extent. In general the intensity will have an inhomogeneous distribution over the beam cross-section, which will also change as the beam propagates. We will attempt to take this into account by considering the propagation of focused Gaussian beams. The effects of focusing and cross-sectional intensity fluctuations have been shown to be important in a description of higher order Raman radiation generated either by SRS with the first Stokes beam as pump [22, 23, 24, 25] or by 4-wave mixing processes which are dependent on phase matching [26, 27].

An exact theory in terms of the rotationally symmetric Gaussian-Laguerre functions which are solutions of the free-space wave equation, has been derived [28, 29]. In this description, the pump is assumed to have a Gaussian intensity distribution so that the gain region in the medium which is set up by the focused propagation of this pump, will be rotationally symmetric. A Stokes field propagating through such a gain region can be described in terms of the coupled free space solutions. This coupled mode description allows for a flow of energy between the modes and hence will better describe the threshold generation of second Stokes radiation by SRS pumped by the first Stokes radiation. It has also resulted in an improved description of competing 4-wave mixing processes [27]. However, the solution is only valid for low gain cases since pump depletion has been neglected.

The theory has been extended to include the possibility of pump deple-

tion [30], simultaneously removing the constraint of the pump necessarily being of the lowest order mode. This solution, however, requires knowledge of the modal composition of the pump and Stokes beams as well as the statistical dependence of these modes on one another. For our purposes we will take a more approximate approach. This will require knowledge of Gaussian beam propagation and therefore a short summary of the basic results appears in Appendix B.

2.3.1 Backward SRS with Focusing

Most of the theory presented thus far has been on forward SRS. Since we ultimately wish to obtain a description of backward SRS, we will now proceed to analyse the effects of focusing for this case. The method of accounting for focusing will be the simple method used by Zhang et al. [31] in the forward case.

The derivation begins with the equations for backward SRS, 2.9, in the steady state. The method of section 2.2.4 is followed to the point where the backward process is described by the equations:

$$\frac{n_l}{\omega_l}\frac{\partial}{\partial z}|E_l|^2 = \frac{4\pi}{c} Im\chi_R^{(3)}|E_1|^2|E_2|^2 \tag{2.56}$$

where $l = 1, 2$ for the pump and Stokes beams respectively. Now for a focused pump beam energy conservation implies that [31]:

$$\frac{n_1}{\omega_1}|E_1(z)|^2\, A(z) = \frac{n_1}{\omega_1}|E_1(0)|^2\, A(0) \tag{2.57}$$

This is easily seen to be the solution of the differential equation:

$$\frac{\partial}{\partial z}|E_1(z)|^2 = -|E_1(z)|^2 \frac{\partial}{\partial z} \ln w_1^2(z) \tag{2.58}$$

where eqn. B.9 has been used. Thus a term of this form included in the above equations of backward SRS will account for a focused beam geometry. It is

clear, however, that $w_2(z)$ for the Stokes beam will in general not be known. Since the focused pump beam defines the gain region for Stokes growth, we expect that the Stokes spot size will follow that of the pump as it propagates. Hence the approximation

$$\frac{1}{w_2(z)}\frac{\partial w_2(z)}{\partial z} = \frac{1}{w_1(z)}\frac{\partial w_1(z)}{\partial z} \Rightarrow \frac{w_2}{w_1} = a \tag{2.59}$$

(a is a constant), results in backward SRS with focused beams being described by:

$$\begin{aligned}\frac{\partial}{\partial z}\eta_1(z) &= -\sigma\eta_1(z)\eta_2(z) - \eta_1(z)\frac{\partial}{\partial z}\ln w_1^2(z) \\ \frac{\partial}{\partial z}\eta_2(z) &= -\sigma\eta_1(z)\eta_2(z) - \eta_2(z)\frac{\partial}{\partial z}\ln w_1^2(z)\end{aligned} \tag{2.60}$$

where the $\eta_i = \frac{n_i}{\omega_i}|E_i|^2$ are the photon densities and $\sigma = -\frac{4\pi}{c}Im\chi_R^{(3)}\frac{\omega_1}{n_1}\frac{\omega_2}{n_2} = -\frac{\omega_1}{n_1}G$ is the generalised gain (note that eqns. 2.32 and 2.13 have been used). Subtracting these two equations from one another leads to the equation

$$\frac{\partial}{\partial z}\ln M(z) = -\frac{\partial}{\partial z}\ln w_1^2(z) \tag{2.61}$$

where

$$M(z) = \eta_1(z) - \eta_2(z) \tag{2.62}$$

This equation (eqn. 2.61) has a solution:

$$M(z) = M(0)\frac{w_1^2(0)}{w_1^2(z)} \tag{2.63}$$

which is analogous to the conservation of the total number of photons during the focused passage through the medium in the forward case (see eqn. 2.30). At this point we note that for a Raman active medium of length L, the boundary conditions are that $\eta_1(0)$ and $\eta_2(L)$ are specified. We proceed

by substituting for $\eta_1(z)$ in the equation for $\eta_2(z)$ which together with the definition

$$P(z) = \left[\frac{1}{\sigma}\frac{\partial}{\partial z}\ln M(z) - M(z)\right]$$

results in Stokes photon density $\eta_2(z)$ being described by the equation

$$\frac{\partial \eta_2(z)}{\partial z} = -\sigma\eta_2^2(z) + \sigma\eta_2(z)P(z) \tag{2.64}$$

which is of the form of eqn. 2.33 and can thus be solved as before. Multiplying through by the integration factor

$$k'(z) = e^{\sigma\int_0^z P(y)\,dy}$$

and integrating the result yields:

$$\frac{k'(z)}{\eta_2(z)} = \sigma\int k'(z)\,dz + C$$

Noting that

$$-\sigma\,k'(z) = \frac{\partial}{\partial z}e^{-\sigma\int_0^z M(y)\,dy}$$

allows the integration to be performed, yielding after manipulation:

$$\frac{M(z)}{\eta_2(z)} = C\,e^{\sigma\int_0^z M(y)\,dy} - 1$$

Applying the boundary condition at $z = 0$, yields $C = \eta_1(0)/\eta_2(0)$ for the integration constant, so that the solution becomes:

$$\eta_2(z) = M(z)\left[\frac{\eta_1(0)}{\eta_2(0)}\,e^{\sigma\int_0^z M(y)\,dy} - 1\right]^{-1} \tag{2.65}$$

To obtain an expression from which the Stokes output $\eta_2(z = 0)$ can be found, requires the solution of the pump to found. Following the above method, we obtain for the pump:

$$\eta_1(z) = M(z)\left[1 - \frac{\eta_2(0)}{\eta_1(0)}\,e^{-\sigma\int_0^z M(y)\,dy}\right]^{-1} \tag{2.66}$$

Evaluating this at $z = L$ and solving for $\eta_1(0)/\eta_2(0)$ yields

$$\frac{\eta_1(0)}{\eta_2(0)} = \frac{M(L) + \eta_2(L)}{\eta_2(L)} e^{-\sigma \int_0^L M(y)\, dy} \tag{2.67}$$

where eqn. 2.62 has been used. Substituting this into eqn. 2.65 and evaluating at $z = 0$, yields the output Stokes photon density:

$$\eta_2(0) = M(0) \left[\left(\frac{M(L)}{\eta_2(L)} + 1 \right) e^{-\sigma \int_0^L M(y)\, dy} - 1 \right]^{-1} \tag{2.68}$$

Finally we need to evaluate the integral in the exponential. This is easily achieved by making use of equation 2.63 with equation. B.12 for the beam spot size. Substitution into the integral appearing in the exponential, yields:

$$\int_0^L M(y)\, dy = M(0) \frac{w_1^2(0)}{w_0^2} z_r \left[tan^{-1} \frac{(L-l)}{z_r} + tan^{-1} \frac{l}{z_r} \right] \tag{2.69}$$

where l is the position of the beam focus in the cell. This substituted into equation 2.68 fully describes the backward Stokes output in the steady state when pump depletion is included together with the effects of focusing.

This is seen to reduce to the solution of Johnson and Marburger [20] in the plane wave case. It is thus seen that the focusing affects the plane wave result in a simple way. This is evident too in the forward case where the result in ref. [31] is seen to be a simple adaption of eqn. 2.37. It is also pleasing to note that the more general solution with pump and Stokes fields of arbitrary cross-sectional intensity profiles [30] reduces to the simpler result of Zhang et al. [31] in the limit of fields containing only the lowest order mode under the assumption of similar beam waists (i.e. eqn. 2.59). These are the conditions under which the above theory was developed. This simplification ignores the observed phenomenon that at high gain, the Stokes beam has a larger divergence than the pump [23, 26] due to the mode coupling which allows for an exchange of energy between the modes [27]. Thus the Stokes

output appears to be coming from a location different from that of the focus of the pump [24]. Since the broad application of the general theory [30] requires knowledge of the pump and Stokes mode structure as well as their statistical properties, we will restrict ourselves to the above simple lowest order approximation.

It will now be informative to investigate the effects of focusing on the measurable quantities. In the notation of eqn. 2.37 we can write the solutions in terms of transmission ratios:

$$T_2(0) = \frac{\delta - T_2(0)}{\delta\, e^{-\zeta[\delta - T_2(0)]L^*} - 1}$$

$$T_1(L) = \frac{\delta - T_2(0)}{\delta - T_2(0)\, e^{-\zeta[\delta - T_2(0)]L^*}} \tag{2.70}$$

where the pump output has been written in terms of the Stokes solution and $\zeta = \eta_2(L)\,\sigma$. An effective gain length has also been defined for plane waves of spot size radius $w_1(0)$:

$$L^* = \frac{w_1^2(0)}{w_0^2}\, z_r \left[tan^{-1}\frac{(L-l)}{z_r} + tan^{-1}\frac{l}{z_r} \right] \tag{2.71}$$

We proceed to analyse these results under three focusing conditions:
(1) $l = 0$ – focus at the cell entrance, (2) $l = L$ – focus at the cell exit and (3) $l = \frac{1}{2}L$ – focus at the centre of the cell. Comparison of these cases with this definition of the gain length leads to the erroneous conclusion of Zhang et al. [31]. The comparison is misleading, since the input intensity ratio ($\delta = \frac{\eta_1(0)}{\eta_2(L)}$ here) is obviously different in each case. We notice, however, that

$$M(0)\frac{w_1^2(0)}{w_0^2} = (\delta - T_2(0))\frac{w_1^2(0)}{w_0^2}\eta_2(L)$$

in eqn. 2.70 is the same in each case representing, as it does, the 'intensity difference' at the focus. Thus for comparison we define the effective gain

length L', for plane waves of spot size equal to the waist size of the focused beam, yielding:

$$L' = \frac{w_0^2}{w_1^2(0)} L^* = z_r \left[tan^{-1} \frac{(L-l)}{z_r} + tan^{-1} \frac{l}{z_r} \right] \tag{2.72}$$

Two regimes are of particular interest in each of the three cases. These are: (a) $L/z_r \ll 1$, i.e. soft focusing $\Rightarrow$ effectively plane waves through the cell, and (b) $L/z_r \gg 1$, i.e. tight focusing. It is readily apparent that for the first limit (a) $L/z_r \ll 1$, the three focused cases reduce to the expected plane wave result i.e. $L' = L$. In the second limit (b) $L/z_r \gg 1$, the first two cases, (1) $l = 0$ and (2) $l = L$, both reduce to

$$L' \simeq \frac{\pi}{2} z_r$$

In this limit, the third case, (3) $l = 1/2L$ reduces to:

$$L' \simeq \pi z_r \tag{2.73}$$

resulting in twice the gain of the other two cases. The effects of the focusing conditions and the length of the medium can be investigated in a more instructive way by looking at L'/z_r. In the first instance we look at a fixed cell of length L with the focal plane varying from the cell entrance to the cell exit. Thus define:

$$L_f(z) = \frac{L'}{z_r}(z) = [\, tan^{-1} z/z_r + tan^{-1}(L-z)/z_r \,] \tag{2.74}$$

Secondly we may look at a beam with fixed focusing characteristics (i.e. l fixed) traversing a cell of variable length. In this case we define:

$$L_g(z) = [\, tan^{-1} l/z_r + tan^{-1}(z-l)/z_r \,] \tag{2.75}$$

These two functions are plotted together in figure 2.6 for $L/z_r = 300/1.24 \gg 1$ and $l = 150\ mm$. The curve of $L_f(z)$ illustrates that once the focal

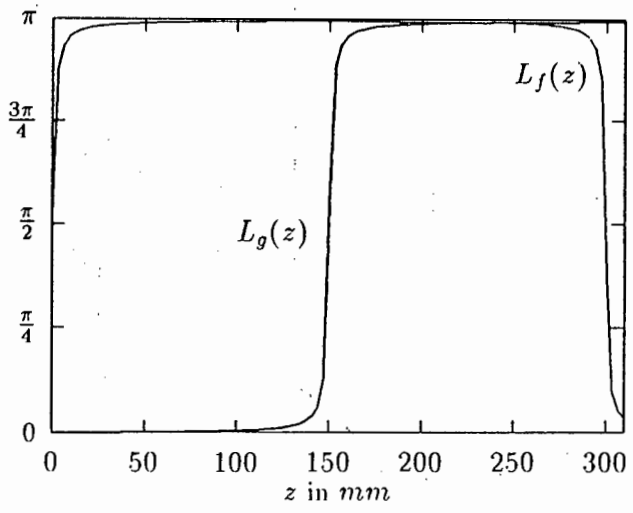

Figure 2.6: illustrates the dependence of various focusing conditions L_f and cell lengths for a fixed focusing condition L_g on the effective gain length. The observations being discussed in the text.

region is inside the medium, the gain saturates. Included are the three cases (1,2,3) considered above. The curve of $L_g(z)$ illustrates the same result from a different perspective; showing again that only when the medium is sufficiently long so as to include the focal region, is the gain at its maximum. It is clear that increasing the length of the medium beyond the focal region has a negligible effect on the available gain.

We restrict our discussion now to the last case (or more generally to the case where the whole focal region is within the medium) as this most closely models most experimental situations. It is seen that for a Gaussian beam focused midway in a Raman active cell, the effect of focusing may be viewed as follows: The initial propagation of the focused beam through the cell can be treated as free space propagation until the focal region is reached

whereupon the beam may be treated as a plane wave of the same intensity as at the waist of the focused beam. This beam can then be assumed to experience gain over roughly the length of the focal region. It is seen in the above equation that this effective interaction length is slightly longer than the confocal region (extent of the beam focus – see Appendix B) of the focused beam.

Alternatively, a plane wave of the same intensity as that of the focused beam upon entry into the cell is seen to have an effective gain length of:

$$L^* = \frac{\pi L^2}{4 z_r} \tag{2.76}$$

for the above conditions. Even for reasonably soft focusing, this will be longer than the actual cell length. For this reason it is more convenient to hold the former view. It should be noted that this picture breaks down when the intensity at the focus becomes sufficiently large. It is relatively easy to obtain extremely large gains at the focus (e.g. $f = 300mm$ lens with $w_1(0) = 2.5mm$ in H_2 yields $gI_1L \simeq 150$ for a laser power of $1\,MW$, where $g = 2.5\,cm/GW$ [32] has been used) in which case large conversion will occur well before the entire focal region has been traversed. A much more complicated dynamic interaction can be envisaged as the response of the medium becomes important. A steady state treatment seems inappropriate. This type of situation will be considered in section 2.5 when the transient response of the medium is discussed.

The intensity transmissions given by eqn. 2.70 are plotted in figure 2.7 as a function of the gain length for an input intensity ratio of $\delta = 1000$. This may be compared with fig. 2.1 representing the plane wave solution of forward SRS from which it is seen that the pump is not as drastically

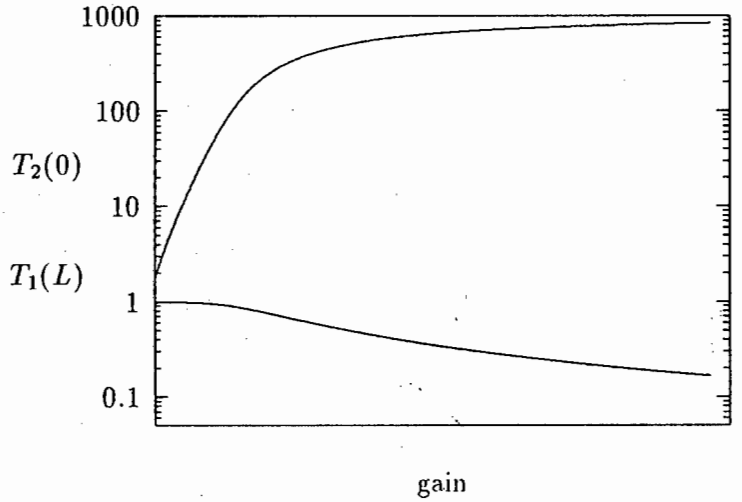

Figure 2.7: illustrates the output backward transmission coefficient $T_2(0)$ as well as the pump transmission coefficient $T_1(L)$ for backward SRS with focusing for an input intensity ratio of $\delta = 1000$. As discussed in the text, this figure will be the same as for the plane wave case with a redefinition of the gain length.

depleted. This may be due to the counter-propagating nature of backward SRS, in which the SRS continually sees fresh pump as it travels back, whereas in the forward case the SRS always interacts with the same portion of the pump [12].

2.3.2 Inhomogeneous Intensity Distribution

The method of taking focusing into account presented above assumes a uniform intensity distribution across the spot size. However, for a Gaussian intensity distribution this is obviously not the case. The intensity measured experimentally will be an average intensity over the aperture. Hence for comparison, the theoretical intensities should be averaged over the aper-

ture [25, 31]. Thus for an aperture of radius b, the average intensity is defined as:

$$I_{av}(b) = \frac{\int_0^b I(r) r\, dr}{\int_0^b r\, dr} \tag{2.77}$$

where $I(r)$ is given by eqn. B.5. Performing the integration leads to the result:

$$I_{av}(b,z) = I(0,z)\frac{w^2(z)}{2b^2}\left[1 - e^{-\frac{2b^2}{w^2(z)}}\right] \tag{2.78}$$

where $I(0,z)$ is the peak (on axis) intensity and $w(z)$ is the beam spot radius at the position (z) of measurement. It is easily shown that the on axis intensity $I(0,z)$ is equal to twice the total power in the beam divided by the cross sectional area i.e.

$$I(r=0,z) = \frac{2P_t}{\pi w^2(z)} \tag{2.79}$$

We now assume that the beam can be represented as a square wave pulse of duration τ and height E_t, where E_t is the total energy in the beam passing through an aperture of radius b. Thus the total power in such a beam is given by

$$P_t = \frac{E_t}{\tau} \tag{2.80}$$

If we now assume that at the aperture of the measuring device the beam radius is the same as that of the aperture, then the average intensity of the beam is given by eqn. 2.78 after substitution of eqns. 2.79 and 2.80, yielding:

$$I_{av} = \frac{E_t}{\pi b^2 \tau}[1 - e^{-2}] \tag{2.81}$$

Thus we have taken the inhomogeneous intensity distribution into account.

2.4 The Forward/Backward Gain Anomaly

Much work has been done on the forward/backward SRS gain ratio. On the basis of the steady state theory with a constant pump (see section 2.2.1) for monochromatic fields with no dispersion, SRS is predicted to occur with equal gain in the forward and backward directions [10, 11]. In reality, however, this situation is never realised for a number of possible reasons: i) Dispersion can not in general be ignored. This will give rise to small differences in the forward/backward gain which will appear as large intensity differences due to the exponential nature of the amplification. ii) The monochromatic field approximation is rarely realised, necessitating consideration of the frequency structure of the input fields. iii) In liquids the phenomenon of self-focusing plays a crucial role. Often experimental setups have a focused geometry which is therefore also important to take into consideration. iv) It has also been suggested that in some cases anti-Stokes coupling in the forward direction may explain a gain ratio differing from unity.

In section 2.4.1 below, the effects of the frequency structure of the input fields, on the theory is discussed. In these considerations the importance of dispersion will become apparent and we will attempt to account for it. This will be followed in section 2.4.2 by a discussion on anti-Stokes scattering and how this affects the SRS output. Focusing will be shown to play an important role in these considerations. The discussions will by and large be restricted to the case at hand, where a narrow band pump ($\Gamma_l \ll \Gamma$) enters a gaseous medium (H_2) in a focused geometry, resulting in high intensity backward SRS output.

2.4.1 Input Bandwidths and Dispersion

We start by following the theoretical treatment of Trutna et al. [33] which follows from the set of coupled wave equations derived earlier (i.e. eqn. 2.6). We will relax the single mode plane wave solution, instead expressing the input fields in terms of an arbitrary number of plane waves. In this way we can model a laser oscillating in a number of modes. Hence:

$$\vec{E}_l(z,t) = \sum_j \vec{E}_{lj}(z,t)\, e^{i(k_{lj}z - \omega_{lj}t)} \tag{2.82}$$

where $l = 1, 2$ for the pump and Stokes fields respectively. As before, fields propagating in the opposite direction to the pump are described by replacing k_j by $-k_j$. We proceed with copropagating beams, since the results for counter propagating beams will follow this case. This decomposition of the fields enables dispersion to be taken into account in an approximate way. As in the single mode case presented previously, the frequencies are related via the Raman resonance of the medium.

$$\omega_{1j} - \omega_{2j} \simeq \omega_v$$

Similarly the material excitation is seen to propagate with a wave vector $k_{vj} = k_{1j} - k_{2j}$. Dispersion will ensure that this relationship is not the same for each mode. Thus by defining

$$k_v = k_{10} - k_{20}$$

we are able to obtain an expression for the k-vector (or momentum) mismatch of the j^{th} mode:

$$k_{1j} - k_{2j} \simeq k_v + \Delta\omega_j \left(\frac{1}{v_1} - \frac{1}{v_2}\right) = k_v + \Delta k_j \tag{2.83}$$

where

$$\Delta\omega_j = \omega_{1j} - \omega_{10} = \omega_{2j} - \omega_{20}$$

is the detuning of the j^{th} mode. This is valid for a gas with low dispersion, where v_1 and v_2 are respectively the group velocities of the pump and Stokes fields. In the wide mode spacing approximation (i.e. $\Delta\omega_{ij} = \omega_j - \omega_i \gg \Gamma$), the equations governing the amplitudes of the fields and the material excitation in eqn. 2.6 become:

$$\begin{aligned}
\left(\frac{\partial}{\partial z} + \frac{1}{v_1}\frac{\partial}{\partial t}\right) E_{1j}(z,t) &= +i\frac{\omega_1}{n_1}\frac{n_2}{\omega_2} B_1 E_{2j}(z,t) A(z,t)\, e^{-i\Delta k_j z} \\
\left(\pm\frac{\partial}{\partial z} + \frac{1}{v_2}\frac{\partial}{\partial t}\right) E_{2j}(z,t) &= +i\, B_1 E_{1j}(z,t) A^*(z,t)\, e^{i\Delta k_j z} \qquad (2.84) \\
\left(\frac{\partial}{\partial t} + \Gamma\right) A^*(z,t) &= -i\, B_2 \sum_j E^*_{1j}(z,t) E_{2j}(z,t)\, e^{-i\Delta k_j z}
\end{aligned}$$

where the constants are given by:

$$B_1 = \frac{N}{4\pi}\left(\frac{2\pi\omega_2^2}{k_2 c^2}\right)\left(\frac{\partial\alpha}{\partial Q}\right)_0$$

$$B_2 = \frac{1}{(4\pi)8m\omega_v}\left(\frac{\partial\alpha}{\partial Q}\right)_0$$

The usual physical interpretation, that the pump and Stokes fields act in pairs to drive the material excitation, is therefore valid. However, here the effect of dispersion (exponential term) causes the pump and Stokes fields to become dephased as they propagate through the medium. Hence when a pump mode mixes with the reduced material excitation, the resulting amplification of its corresponding Stokes mode is also reduced. Whenever the laser pulse duration is much greater than the dephasing time of the material ($\Gamma_l \gg [\Gamma^{-1} = 1/T_2]$) then the steady state solution of the above

equations can be found. A more stringent criterion will be introduced in the next section. The rate of change of the average Stokes intensity in the case of no dispersion ($\Delta k_n = 0$) is readily shown to be:

$$\frac{\partial}{\partial z}\bar{I}_2 = \beta g \bar{I}_2 \tag{2.85}$$

which is seen to differ from the single mode result (eqn. 2.14) by a gain reduction factor β defined by:

$$\beta = \left\{ \frac{[\sum_n |E_{2n}|\,|E_{1n}|\,]^2}{\sum_n |E_{1n}|^2 \sum_n |E_{2n}|^2} \right\} \tag{2.86}$$

Embodied in this description is a constraint on the relative phase and amplitude of the fields in order to achieve maximum gain. The requirement for maximum gain is encapsulated by the relationship:

$$\frac{E_{1n}}{E_{2n}} = c(z) \tag{2.87}$$

where $c(z)$ is complex and independent of the mode n. The constraint on the relative phase implied here (i.e. $\phi_{1n} - \phi_{2n} = \phi_0$) for all n has been given by a number of authors [16, 34]. Further it can be shown that for pump and Stokes fields of the same spectral distribution, there is no reduction in the gain compared to the single mode case i.e. $\beta = 1$. This leads to an important prediction in the dispersionless case when the SRS is built up from spontaneous Raman noise (i.e. there is no external Stokes input). The prediction is that in order to maximise the gain, the Stokes spectrum automatically duplicates the pump spectrum. This follows from the fact that only when a noise component has the correct frequency and phase relationship with the pump will it see significant amplification.

In the case where dispersion is not neglected ($\Delta k_n \neq 0$), the above considerations for maximum gain will still hold. However, the effect of dispersion is to destroy the phase relationships between the fields as they propagate through the medium. This process may be characterised by a coherence length [33, 35]:

$$l_c \simeq \frac{c}{2(n_1 \mp n_2)} \Delta\nu_1 \tag{2.88}$$

where $n = \frac{c}{v}$ is the refractive index in the medium and $\Delta\nu_1 = \frac{\Delta\omega_1}{2\pi}$ is the bandwidth of the pump. Here the minus (plus) sign represents copropagating (counter-) pump and Stokes fields. Thus if this length, over which the requisite phase relationships for maximum amplification are maintained, is longer than the effective interaction length of the medium, then there will be no reduction in the gain and dispersion can be ignored.

There is an obvious asymmetry in this coherence length depending on whether forward or backward scattering is being considered. The coherence length for backward SRS will be much shorter than that for forward SRS. However, for a sufficiently narrow pump we will have $l_c(\mp) > L$ (L is the length of the medium) and no asymmetry in the gain is predicted. For a broadband pump the prediction is for reduced gain in the backward direction. This will therefore not explain our observation of 'predominantly' backward SRS output.

A complementary approach was followed by Egglestone and Byer [36] who investigated the change in the gain reduction factor β during propagation through the cell. The interpretation of β as the pump/Stokes correlation factor affords a clearer description. The gain mechanism tends to increase the correlation, while dispersion obviously results in a reduction

as the fields propagate through the medium. Thus it was concluded that as long as the gain mechanism was strong enough to overcome the effects of dispersion, the pump/Stokes correlation would increase with propagation through the medium. Thus the resulting amplification of the Stokes field would approach the single mode result. This interaction was also noticed by Carman et al. [34], and has been experimentally observed [37]. In fact Egglestone and Byer [36] go further and include pump depletion in their considerations. It is pleasing to note that in the single mode case their result reduces to that presented here (i.e. eqn. 2.37 of section 2.2.4). From their more general result it is seen that for non-monochromatic input fields an extra interaction length (i.e. higher gain) is required before the Stokes output reaches saturation. The result that the SRS gain is independent of laser bandwidth in the case of no dispersion was also obtained for SRS built up from Raman noise [17]. In this case the Stokes spectrum was shown to be gain narrowed. In fact as mentioned earlier, the result for the halfwidth of the Stokes output, eqn. 57 of Raymer et al. [17] is the same as was obtained by our more simplistic approach (i.e. eqn. 2.27) which is valid for both forward and backward Stokes output.

It is of interest to compare these predictions, for the output Stokes spectrum, with those presented in sections 2.2.3 and 2.2.5. The different way in which the frequency structure is modeled should be kept in mind. The model used in the above description is of pump and Stokes inputs consisting of many widely spaced, independent, modes. In the earlier development (i.e. sections 2.2.3 and 2.2.5), the input linewidths were modeled by introducing a frequency mismatch in the SRS gain. Even with these differences in model, the qualitative agreement is remarkable. The prediction here is that for SRS

built up from the initial Raman noise, the Stokes output spectrum will be driven, by the pump, to replicate the pump spectrum provided the gain is sufficiently high [36]. This is precisely the type of mechanism, intimated by the considerations of section 2.2.5, in which pump depletion was included (see page 41).

It should be noted that many models have been proposed to take the input spectral distributions into account [16, 34, 36, 38]. There is, however, a large variation in the predictions depending on the way in which the input spectral profiles were modeled [39]. Those presented here seem to be the most appropriate.

2.4.2 Stokes – Anti-Stokes Coupling and Focusing

The parametric coupling between the Stokes and the anti-Stokes fields has been proposed as an explanation of the forward/backward gain asymmetry. The coupling has been known for some time [10, 40] to lead to suppression of the forward scattered Stokes emission. Because of the nature of the coupling, the effects of both focusing and dispersion are important [21, 26, 27]. The precise nature of these effects will become clear upon investigation of the parametric coupling of the fields. We will now investigate the coupling between the Stokes (at ω_2) and the anti-Stokes (at ω_3) fields in the steady state. The relevant equations being [40]:

$$\begin{aligned} \frac{\partial E_2}{\partial z} &= K_2 E_2 + K_{23} E_3^* e^{i\Delta k z} \\ \frac{\partial E_3}{\partial z} &= K_{32} E_2 e^{-i\Delta k z} + K_3 E_3^* \end{aligned} \tag{2.89}$$

where the coupling constants are given by:

$$K_2 = i\left(\frac{2\pi\omega_2^2}{k_2 c^2}\right)\chi_R^{(3)}|E_1|^2$$

$$K_3 = -i\left(\frac{2\pi\omega_3^2}{k_3c^2}\right)\chi_A^{(3)^*}|E_1|^2$$

$$K_{23} = i\left(\frac{2\pi\omega_2^2}{k_2c^2}\right)\sqrt{\chi_R^{(3)}\chi_A^{(3)^*}}|E_1|^2 \tag{2.90}$$

$$K_{32} = -i\left(\frac{2\pi\omega_3^2}{k_3c^2}\right)\sqrt{\chi_R^{(3)}\chi_A^{(3)^*}}|E_1|^{2^*}$$

The momenta k_l $(l = 2, 3)$ are the projections of the propagation vectors in the z-direction and thus $\Delta k = 2k_1 - k_2 - k_3$ is the momentum mismatch in the z-direction. We have assumed no linear absorption and no dispersion (hence $\frac{\omega_2^2}{k_2}\chi_R^{(3)} = \frac{\omega_3^2}{k_3}\chi_A^{(3)^*}$) in the solution. Also it should be noted that $K_{23} \neq K_{32}^*$ in general. With these approximations, the solution of the field amplitudes is found to be:

$$E_2(z) = \mathcal{E}_{2+}e^{i\Delta K_{2+}z} + \mathcal{E}_{2-}e^{i\Delta K_{2-}z}$$

$$E_3^*(z) = \mathcal{E}_{3+}^*e^{i\Delta K_{3+}z} + \mathcal{E}_{3-}^*e^{i\Delta K_{3-}z} \tag{2.91}$$

where the gain constants are given by:

$$\Delta K_{2\pm} = \frac{\Delta k}{2} + \Delta K_\pm$$

$$\Delta K_{3\pm} = -\frac{\Delta k}{2} + \Delta K_\pm \tag{2.92}$$

$$\Delta K_\pm = \pm\sqrt{\left(\frac{\Delta k}{2}\right)^2 - \Lambda\Delta k}$$

with $\Lambda = -iK_2$ and the steady state Raman gain is $g = -2\,Im(\Lambda)$ (cf. section 2.2.1). With the boundary conditions $E_2 = \mathcal{E}_{20}$ and $E_3 = \mathcal{E}_{30}$ at $z = 0$, the amplitudes can be shown to be [18]:

$$\frac{\mathcal{E}_{3\pm}}{\mathcal{E}_{2\pm}} = \frac{\Delta K_\pm - \Lambda + \frac{\Delta k}{2}}{\Lambda}$$

$$\mathcal{E}_{2\pm} = \frac{(-\frac{\Delta k}{2} - \Delta K_{\mp} + \Lambda)\mathcal{E}_{20} + \Lambda\mathcal{E}_{30}^{*}}{\Delta K_{\pm} - \Delta K_{\mp}} \tag{2.93}$$

This result facilitates physical interpretation. Out of the coupling, two composite waves ($\mathcal{E}_{2+}$,$\mathcal{E}_{3+}$) and ($\mathcal{E}_{2-}$,$\mathcal{E}_{3-}$) have arisen with the amplitude ratio given above. It is apparent that if $Im(\Delta K_{+}) > 0$ then that wave will experience exponential gain while the other wave will experience loss (i.e. $Im(\Delta K_{-}) < 0$) and vice versa. The relative nature of the composite waves clearly depends on phase matching. The coupling is maximised for exact phase matching ($\Delta k = 0$), since then $|\mathcal{E}_{3\pm}/\mathcal{E}_{2\pm}| = 1$ and both composite waves have fifty percent Stokes and fifty percent anti-Stokes character. Hence there is neither gain nor loss for either of the composite waves and therefore also for the Stokes and anti-Stokes waves (i.e. $\Delta K_{n\pm} = 0$)! This is a well known result from parametric oscillator theory [18].

If the phase mismatch is very large then the fields are not coupled and the solutions can be found individually. The most interesting case is where one of the composite waves experiences exponential gain while the other experiences loss. It should be clear that this will occur when both $\Delta K_{\pm}$ and Δk are non-zero or $|\Delta k| \sim |\Lambda|$. The anti-Stokes radiation will therefore be emitted in a cone about the phase matching direction (see figure 2.8). It should be noted that Λ is in general proportional to $1/(\Delta\omega + i\Gamma)$ (by substituting eqn. 2.22 into K_2 in eqn. 2.90). Thus both the momentum mismatch Δk and the accompanying frequency mismatch $\Delta\omega = \omega_1 - \omega_2 - \omega_v$ affect the conditions for achieving large anti-Stokes output [10, 40]. From these considerations one can see that the Stokes–anti-Stokes coupling in the forward direction can seriously inhibit the forward SRS output. Since there is no anti-Stokes coupling to the backward SRS due to the phase mismatch being

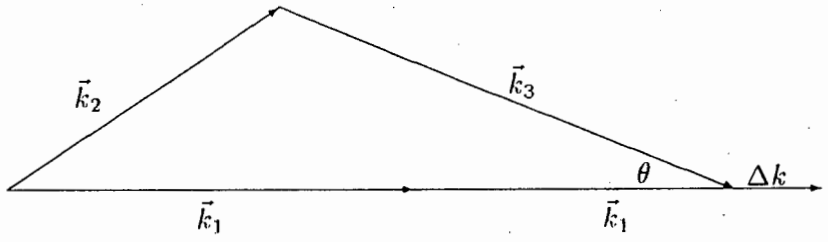

Figure 2.8: illustrates the momentum mismatch for anti-Stokes generation. The anti-Stokes radiation will be emitted in a cone of half apex angle θ about the phase matching direction ($\Delta k = 0$).

too large, this provides a possible explanation for predominantly backward scattered output in some cases.

The role of focusing in all of this can now be discussed. Since focusing changes the available propagation directions, it provides the fields with more freedom to seek out favourable momentum mismatch conditions. This has been experimentally verified by Perry et al. [27], who found that the ratio of Stokes to anti-Stokes output intensity depended critically on the confocal parameter of the pump beam. They went on to propose this as an explanation for their observation of backward SRS for small confocal parameters (i.e. tight focusing) since, as mentioned above, backward SRS is not coupled to the anti-Stokes scattering process.

It has also been pointed out that dispersion plays an important role in this and other 4-wave mixing processes. Thus in a gaseous Raman medium, varying the pressure alters the dispersion of the medium which therefore affects the phase matching condition [21]. This explanation of the for-

ward/backward gain asymmetry in favour of large backward SRS output is also under dispute [41]. However, focusing does in one way or another seem to play a very important role [42]. This is intimated by the phenomenon of self-focusing which was earlier found to explain anomalous results of this type in liquids. It should be noted that when self-focusing does occur, there are probably other complicated simultaneous nonlinear interactions going on [18, 43]. This may not be the case with focused beams in a gas. It does, however, remain necessary to account for focusing in our considerations as its possibly crucial role is by no means clear.

2.5 Transient Stimulated Raman Scattering

2.5.1 Discussion

Up until now we have restricted our considerations to the steady state, where time dependent phenomena were unimportant. We have not as yet fully described the conditions under which this assumption is valid. This question will be addressed in this section. Although, in many cases the observable quantities may be described by the steady state results, a reasonable picture of the initiation mechanism is only obtainable by considering the time dependence of the interaction dynamics. The exact role of focusing in all of this is also unclear (as mentioned in the previous section).

The full equations describing SRS in the monochromatic plane wave model have been derived at the beginning of this chapter. It was shown that a complete description is afforded by first solving for the equation describing the population difference (eqn. 2.4) and using this in the coupled equations for the pump and Stokes fields as well as the material excitation wave i.e. eqn. 2.3. However, in our classical model we have assumed that the population difference never deviates drastically from its equilibrium value. Under very high intensities this may not necessarily be valid, requiring equation 2.4 to be solved together with eqn. 2.3 in the quantum mechanical treatment. We consider only the case where our assumption still holds, in which case the process is fully described by eqn. 2.6 which we reproduce here for convenience.

$$\left(\pm\frac{\partial}{\partial z}+\frac{1}{v_2}\frac{\partial}{\partial t}\right)E_2(z,t)=i\frac{N}{4\pi}\left(\frac{2\pi\omega_2^2}{k_2c^2}\right)\left(\frac{\partial\alpha}{\partial Q}\right)_0 E_1(z,t)A^*(z,t)$$

$$\left(\frac{\partial}{\partial z}+\frac{1}{v_1}\frac{\partial}{\partial t}\right)E_1(z,t)=i\frac{N}{4\pi}\left(\frac{2\pi\omega_1^2}{k_1c^2}\right)\left(\frac{\partial\alpha}{\partial Q}\right)_0 E_2(z,t)A(z,t)$$

$$\left(\frac{\partial}{\partial t} + \Gamma + i(\omega_v - \omega)\right) A^*(z,t) = \frac{-i}{(4\pi)8m\omega_v}\left(\frac{\partial \alpha}{\partial Q}\right)_0 E_1^*(z,t)E_2(z,t)$$

Various transient regimes have been considered in the past [44]. In some cases the propagation of the fields is treated in a steady state manner, while the temporal response of the material excitation was included. This is based on the pump duration being comparable to the relaxation times of the material (i.e. $T_l \approx T_1, T_2$). This is the initial way in which transient phenomena were modelled [11, 45]. Often the temporal growth of the fields is comparable to their spatial growth, necessitating the inclusion of the temporal response of the fields as well. This was done in the case of forward SRS by Carman et al. [34]. In the backward case, however, Maier et al. [12] kept the temporal response of the fields but assumed that the temporal response of the material excitation was unimportant. A criterion for the consideration of the general transient response was found to be [34]: $g\,I_1 L\,T_2 > T_l$ where T_l is the pump duration, T_2 is the material collisional dephasing time and $g\,I_1 L$ is the usual steady state Raman gain. The origin of this condition will become apparent in the following section.

The transient response of the medium has been modelled in a number of ways. Initially, the material excitation was treated as a phonon wave using the classical representation followed here. Subsequently, the material excitation was described quantum mechanically by the vector Bloch model of Grishkowsky et al. [47] (see [16, 44]). We will, however, continue with the classical phonon wave description.

Other time-dependent phenomena on a time scale longer than that of the transient response have been found both in the case where a steady state response of the medium was assumed [20] and where the temporal response

of the medium was accounted for [19]. In the first case the phenomenon was reminiscent of relaxation oscillations and was found to occur as a two wave oscillation of the backward Stokes and pump beams. A corresponding three wave oscillation was found when the forward Raman field was included, although no oscillation was found when only the forward Stokes field was considered together with the pump. In the second case similar 'relaxation oscillations' were found in the case of forward scattering. In this case the input intensity ratio of the pump to the Stokes field was almost unity which would enable the pump field to be rapidly depleted [19]. In the case where focusing was taken into account (back scattering only), it was found that the period of the oscillations was dependent on the confocal parameter of the focused beam [46]. This makes sense in the light of our discussion on page 48 in which it was shown that the focusing results in large gain only in the focal region.

It is therefore evident that in order to elucidate the initiation mechanism in the scheme where 'mainly' backward SRS is produced, the temporal response of the fields and of the medium will have to be taken into account. Also, in view of the discussion in the previous section, the anti-Stokes fields should be included together with the effects of focusing. This has been done by Zaporozhchenko et al. [41]. We will discuss their results in the final chapter after the presentation of our results in the following chapter.

2.5.2 Backward Transient Theory

The backward transient theory can be adapted from the theory of Wang [11] in the forward case. In order to proceed from the general description of SRS given by eqn. 2.6, which is reproduced at the begining of this section, we

must make the assumption of an undepleted pump. With the definition:

$$K_1 = \frac{1}{(4\pi)8m\omega_v}\left(\frac{\partial\alpha}{\partial Q}\right)_0$$
$$K_2 = \frac{N}{4\pi}\left(\frac{2\pi\omega_2^2}{k_2c^2}\right)\left(\frac{\partial\alpha}{\partial Q}\right)_0 \tag{2.94}$$

we obtain the equations describing the transient theory in this case [34]:

$$\left(\frac{\partial}{\partial t} + v_{ph}\frac{\partial}{\partial z} + \Gamma\right) A^*(z,t) = -i\,K_1 E_1^*(z,t)E_2(z,t)$$
$$\left(\frac{1}{v}\frac{\partial}{\partial t} - \frac{\partial}{\partial z}\right) E_2(z,t) = i\,K_2 E_1(z,t)A^*(z,t) \tag{2.95}$$

It should be noted that the minus sign has been chosen in eqn. 2.6 so that the backward process is modelled. The speed of propagation of the pump and Stokes waves is assumed to be the same and hence the subscript of the veloctiy has been dropped. We consider the solution along the characteristics $z' = z - v_{ph}t$ and $t' = t + z/v$ which together with the fact that for a heavily damped phonon wave $v_{ph} \simeq 0$, leads to the process being described by:

$$\left(\frac{\partial}{\partial t'} + \Gamma\right) A^*(z',t') = -i\,K_1 E_1^*(z',t')E_2(z',t')$$
$$\frac{\partial}{\partial z'}E_2(z',t') = -i\,K_2 E_1(z',t')A^*(z',t') \tag{2.96}$$

At this point it should be noted that the solution can be obtained if a step function pump pulse is assumed. In this case the solution will be precisely that of Wang [11] with the employment of the simple change in variable discussed in section 2.2.1 on page 22.

However, for the sake of clarity and completeness, we will proceed with a broad outline of the solution. Solving for A^* in the second of eqn. 2.96 and substituting it into the first, yields the partial differential equation:

$$\frac{\partial}{\partial t'}\left(\frac{1}{E_1}\frac{\partial E_2}{\partial z'}\right) + \frac{\Gamma}{E_1}\frac{\partial E_2}{\partial z'} = -K_1\,K_2 E_1^* E_2 \tag{2.97}$$

This equation can be compared with the corresponding equation of Carman et al. [34]. However, since in this case the characteristic $t' = t+z/v$, describes a backward propagating wave and the pump is a function of $(t - z/v)$, the above equation can not be solved for arbitrary pump pulse shapes as was possible in the forward case [34]. Thus in order to solve the above equation the assumption of a step function pump pulse of duration $\overline{\tau}$, must be made, since then E_1 is a constant for $t > 0$ and thus does not depend on t' as the pump is assumed to undergo no depletion. Hence the above equation reduces to:

$$\frac{\partial^2 E_2}{\partial t' \, \partial z'} + \Gamma \frac{\partial E_2}{\partial z'} + K_1 \, K_2 |E_1|^2 E_2 = 0 \tag{2.98}$$

which can be solved in the following way. With the definitions

$$x = K_2 |E_1|^2 z' \quad , \quad y = K_1 t' \quad , \quad \beta = \frac{\Gamma}{K_1}$$

equation 2.98 reduces to:

$$\frac{\partial^2 E_2}{\partial x \, \partial y} + \beta \frac{\partial E_2}{\partial x} + E_2 = 0 \tag{2.99}$$

which is a hyperbolic partial differential equation and can be solved by Riemann's method [48, 49]. The explicit method follows that of Wang [11] with the only major difference arising from the different boundary conditions, which necessitate a different choice of the integration region. The integration region to be used in the case of backward SRS is illustrated in figure 2.9. The initial region APB with curve Γ must be chosen so that the point P is the point at which the final evaluation of the backward scattered Stokes field is required. With the identification $U = E_2$, the solution to eqn. 2.99 is

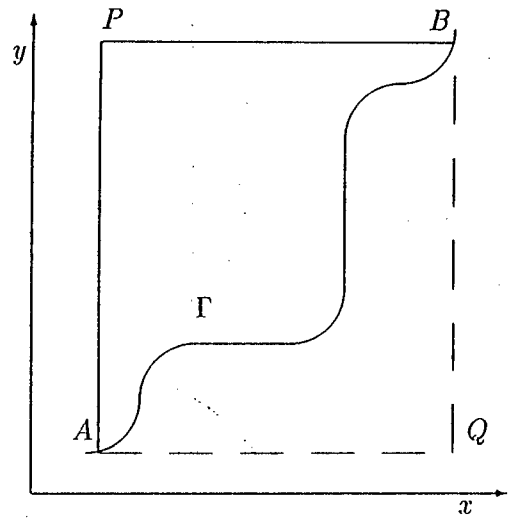

Figure 2.9: illustrates the appropriate integration region for the evaluation of the backscattered Stokes field amplitude at the cell entrance.

$$U]_P = U\,V]_B - \int_Q^B U\left(\frac{\partial V}{\partial y} - \beta\,V\right)dy + \int_A^Q V\frac{\partial U}{\partial x}\,dx \tag{2.100}$$

where $V(x, y, x', y')$ is known as Riemann's function, which must be a solution of the equation:

$$\frac{\partial^2 V}{\partial x'\,\partial y'} - \beta\frac{\partial V}{\partial x'} + V = 0 \tag{2.101}$$

which is known as the adjoint of equation 2.99. It is easily verified that a solution of this equation satisfying the necessry conditions [48, 49] is:

$$V(x, y, x', y') = e^{-\beta(y-y')}I_0[2\sqrt{(y-y')(x'-x)}] \tag{2.102}$$

where $I_0(s)$ is the modified Bessel function of zeroth order. The final solution may be obtained by choosing the curve Γ such that the region of integration is $PAQBP$ as in figure 2.9. Then A must be identified as the

origin (i.e. $A \equiv (0,0)$) and both B and Q should be at the cell exit. Hence the first term of eqn. 2.100 is a boundary condition since $U \equiv E_2$ is evaluated at $z' = L$ i.e. $U]_B = E_0$. It should be noted that the conditions imposed on V [49] require $V]_B = 1$. In our case it is easily shown that the final term of eqn. 2.100 does not contribute, since:

$$\frac{\partial E_2}{\partial x'}\Big|_{y'=0} \propto A^*|_{t'=0}$$

and we have no phonon wave before the pump arrives, i.e. $A = 0$ for $t < 0$ and the above expression is zero. This leaves only the second term to be considered. This term can be simplified by making use of the recurrence relations for the modified Bessel functions [50], yielding the following expression for the backward SRS field evaluated at the entrance ($z = 0$) of the Raman cell of length $z' = L$:

$$E_2(0,t) = E_0 + E_0\sqrt{\frac{g\Gamma L}{2}}\int_0^t \frac{e^{-\Gamma(t-t')}}{\sqrt{t-t'}} I_1\left(2\sqrt{\frac{g\Gamma L}{2}(t-t')}\right) dt' \quad (2.103)$$

where the steady state gain

$$g = 2K_1K_2\frac{|E_1|^2}{\Gamma} \quad (2.104)$$

has been used. With the change of coordinate $\tau = t - t'$, this becomes:

$$E_2(0,t) = E_0 + E_0\sqrt{\frac{g\Gamma L}{2}}\int_0^t \frac{e^{-\Gamma\tau}}{\sqrt{\tau}} I_1\left(2\sqrt{\frac{g\Gamma L}{2}\tau}\right) d\tau \quad (2.105)$$

where $\tau = t_{max} \equiv \overline{\tau}$ can be viewed as the duration of the pump. The behaviour of this equation can be seen in figure 2.10 where it is plotted versus the steady state gain for a pump duration of $15ns$. Also plotted is the steady state result (see below). At low gains the transient intensity is slightly larger than in the steady state, whereas at much higher gains the

transient intensity is clearly lower as we move further into the transient regime according to eqn. 2.109 below. We now look at the steady state and transient limits of this solution.

2.5.3 Steady State Limit

The steady state occurs when $t \rightarrow \infty$ (i.e. a pump of sufficiently long duration) in which case the integral can be solved exactly after the change of variable $\tau' = \sqrt{\tau}$ has been made [51], yielding:

$$\int_0^\infty \ldots d\tau = \sqrt{\frac{\pi}{\Gamma}}\, e^{gL/4}\, I_{\frac{1}{2}}(gL/4) \tag{2.106}$$

Upon substitution of this result into eqn. 2.105 and by making use of reference [52], yields:

$$E_2(0,\infty) = E_0\, e^{gL/2} \tag{2.107}$$

which is the known steady state result. This is plotted for comparison with eqn. 2.105 in figure 2.10.

2.5.4 Transient Limit

We first consider the high gain limit i.e. $2g\Gamma L\tau \gg 1$, in which case the asymptotic form of the Bessel function can be used [53]:

$$I_1(x) \simeq e^x/\sqrt{2\pi x}\,, \quad x \gg 1$$

so that the Stokes field becomes:

$$E_2(0,t) = E_0 + E_0\sqrt{\frac{\sqrt{2g\Gamma L}}{8\pi}} \int_0^t \frac{e^{-\Gamma\tau+\sqrt{2g\Gamma L\tau}}}{\tau^{\frac{3}{4}}} d\tau \tag{2.108}$$

and the gain is determined by the maximum of the exponent, which is seen to occur at a time:

$$\tau = \frac{gL}{2}\frac{1}{\Gamma} \tag{2.109}$$

It should be apparent that the steady state will only be reached if the duration of the pump is longer than this time at which the integrand achieves its maximum. For a pump pulse of duration just larger than this time, a quasi-steady state regime is achieved, while for a pump pulse with a duration shorter than that implied by eqn. 2.109, the transient regime is realised. This is just the condition mentioned in the initial discussion of this section.

The gain in the transient regime can be calculated provided the condition $\Gamma\tau \ll 1$ holds. In this case the $e^{\Gamma\tau}$ factor in eqn. 2.105 can be set to unity. Thus with the change of variable $\tau' = 2\sqrt{g\Gamma L/2\,\tau}$, equation 2.105 becomes:

$$E_2(0,t) \simeq E_0 + E_0 \int_0^{\sqrt{g\Gamma L/2\,t}} I_1(\tau')\, d\tau' \tag{2.110}$$

which can be evaluated [50] to give:

$$E_2(0,t) \simeq E_0\, I_0\left(2\sqrt{\frac{g\Gamma L}{2}t}\right) \tag{2.111}$$

In the large gain limit, the Bessel function can again be replaced by its asymptotic form [53], finally yielding for the amplitude of the backscattered Stokes field in the transient regime with high gain [16]:

$$E_2(0,t) \simeq E_0 \frac{e^{2\sqrt{\frac{g\Gamma L}{2}t}}}{\sqrt{4\pi\sqrt{\frac{g\Gamma L}{2}t}}} \tag{2.112}$$

This enables the transient gain to be defined as:

$$G_T = 4\sqrt{\frac{g\Gamma}{2}\frac{t}{L}} \tag{2.113}$$

(i.e. $I_2(0,t) \propto e^{G_T L}$), which is independent of the halfwidth of the material excitation, since $g \propto 1/\Gamma$.

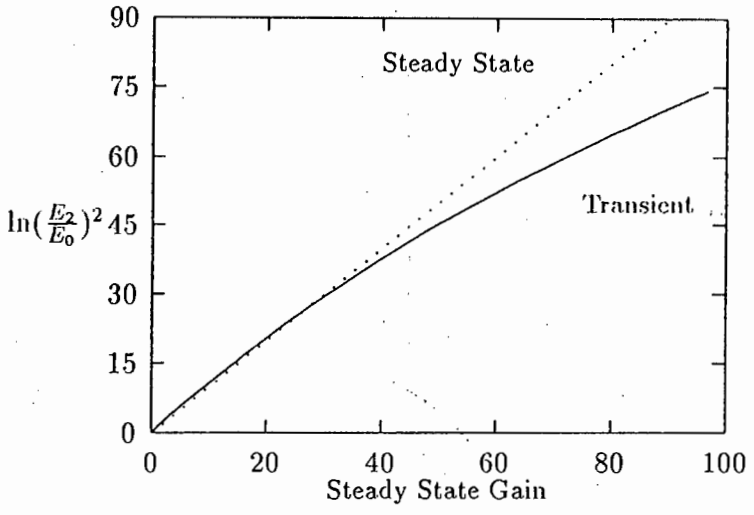

Figure 2.10: illustrates the Stokes intensity ratio as a function of gain in both the transient and steady state regimes. The curve is for a pump duration of $15ns$ in hydrogen at $41\,atm$ i.e. $\Gamma \simeq 10^9 Hz$.

This concludes our theoretical investigation into backward stimulated Raman scattering. The results of our experimental investigation are presented in the following chapter.

Chapter 3

Experimental Investigation

Introduction

We investigated various aspects of backward SRS in hydrogen ($\nu_r = 4155\,cm^{-1}$) pumped by a frequency doubled single longitudinal mode $Nd:YAG$ laser ($532\,nm$). The Stokes radiation was generated from noise by the $15\,ns$ long pump focused into a variable pressure cell containing the hydrogen.

Initially our experiments were simply aimed at quantifying the energy conversion efficiency and linewidth of the backward SRS output as a function of both the pump energy and the hydrogen pressure. After performing an extensive literature review, it became apparent that there were other areas of interest. One such area of interest was the effect of the focusing conditions on the backward to forward SRS intensity ratio. Also of interest was the temporal structure of the various output beams and their relationships to one another. We attempted to investigate these phenomena in the hope of achieving a better understanding of the dynamic interaction giving rise to 'predominantly' backward stimulated Raman scattering.

We now present the results of this investigation in two parts. In the first

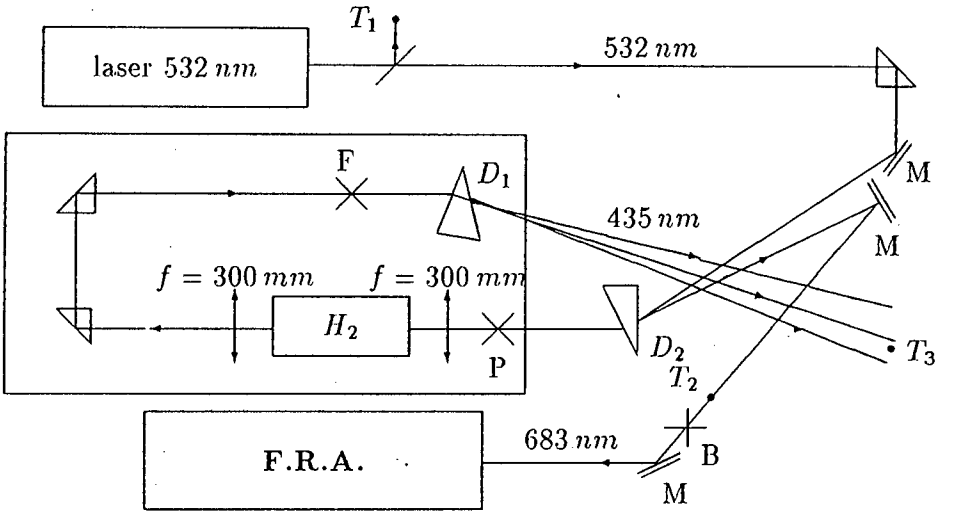

Figure 3.1: illustrates the experimental setup which we used. The box labelled **F.R.A.** contains the Fringe Recording Apparatus which is illustrated in detail in figure 3.11. The labels M, refer to mirrors. The labels P, B and F refer to the positions at which the calorimeter was inserted to measure the energies of the various beams. The labels T_1, T_2 and T_3 indicate the positions at which the various beams were sampled for temporal measurements.

section we will deal with the energy conversion and the temporal relationship measurements. We discuss the results of these measurements together since they involve complementary ideas. The second section will be concerned with the results of the linewidth measurements. Throughout this chapter an attempt will be made to compare qualitatively the results with the theory, so that a better picture of the overall process can be constructed.

3.1 Investigation of Energy Conversion Efficiency

The aim of this investigation was to obtain information about the Raman gain for backward stimulated Raman scattering. The setup used is that illustrated in figure 3.1.

For the energy conversion measurements a calorimeter (Scientech 380101) was inserted at the various positions P, B and F (see fig. 3.1), where the energy of the pump beam at the cell entrance, the backward Stokes beam exiting the cell and the radiation transmitted through the cell respectively was measured . Unfortunately the low sensitivity of the instrument used limited the measurements to energies well above threshold (i.e. visible to the naked eye). In fact our measurements will be seen to be in the heavy depletion/saturation gain region. All our energy measurements have been corrected for losses at the various optical elements. There is a 10% uncertainty associated with the calorimeter readings.

The temporal measurements were made by diverting a portion of the beam at the various positions T_1, T_2 and T_3 (see fig. 3.1) to a PIN diode (SOPRA) by means of an optical fibre cable. The traces were viewed on an oscilloscope (Tektronix 2467 $350MHz$) and recorded by means of a $35\,mm$ camera with high speed BW film (Ilford HP400). We decided to record two profiles simultaneously so that a direct comparison of the temporal structure of the various beams could be made. This was achieved by introducing a delay into the path of one of the beams before it reached the photodiode. It was found that there was sometimes large variability from shot to shot, which further justified a simultaneous recording. Neutral density filters were used to ensure that the relative intensity of the two traces was similar. It is important to keep this in mind when the traces are interpreted. A selection of traces, which illustrate some of the salient features, are reproduced in figure 3.2. The relevance of each of these will become apparent as the other experimental results are presented.

The shutter was operated manually which led to some difficulty in cap-

(a)

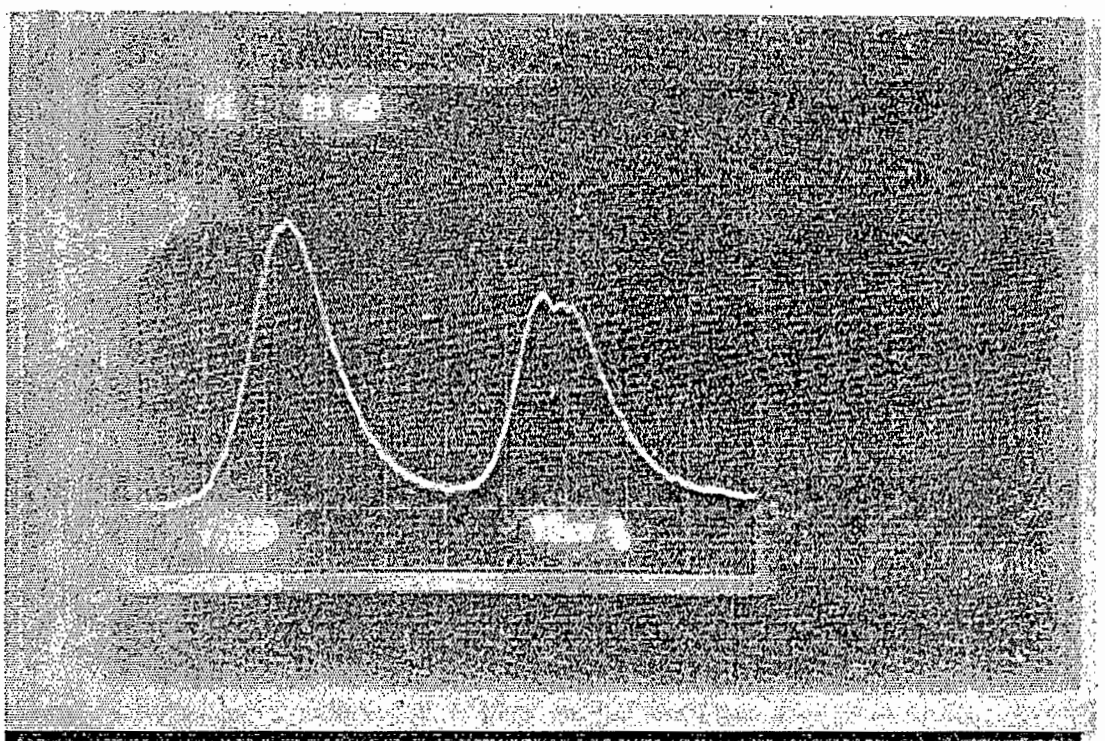

(b)

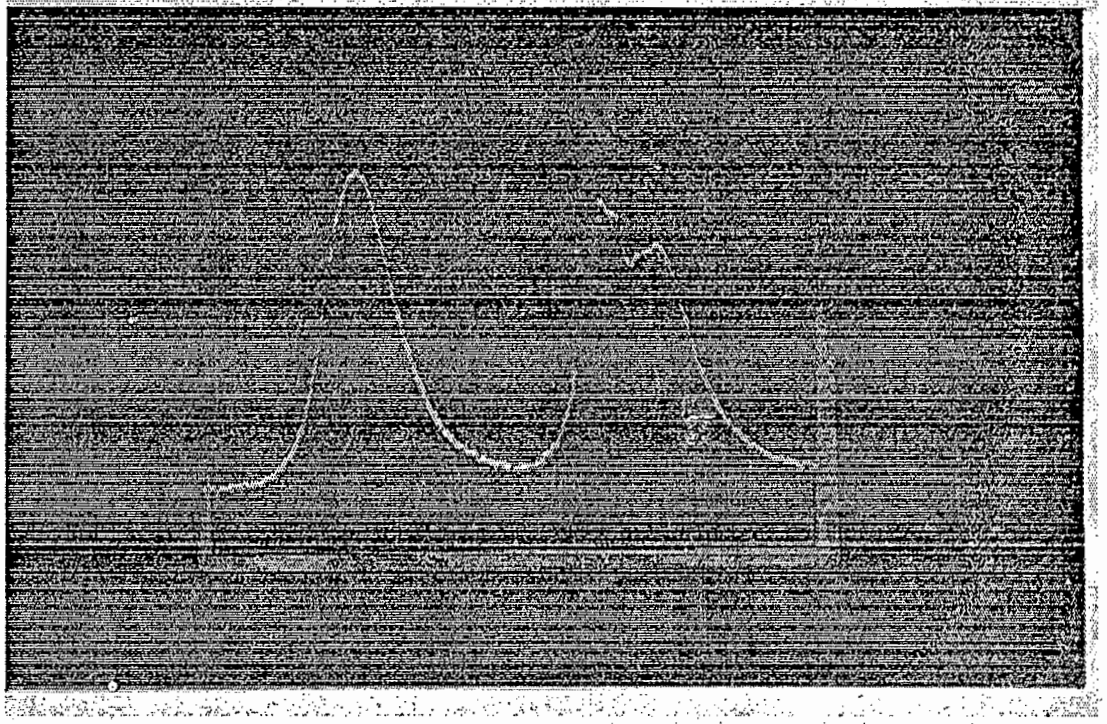

(c)

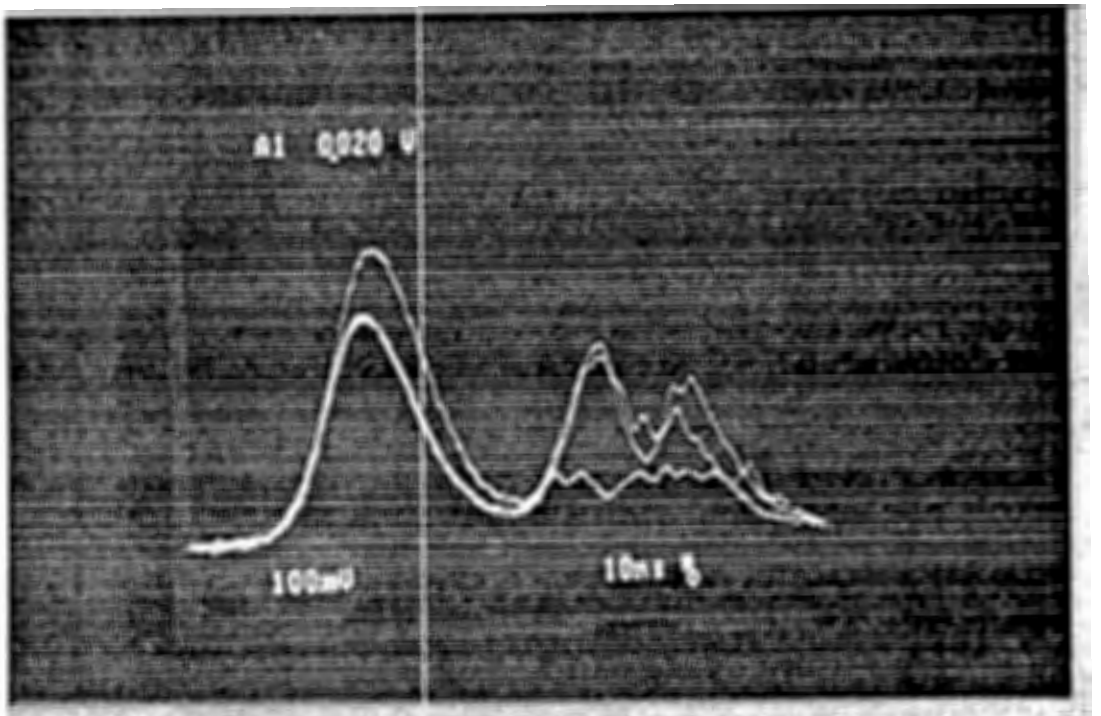

(d)

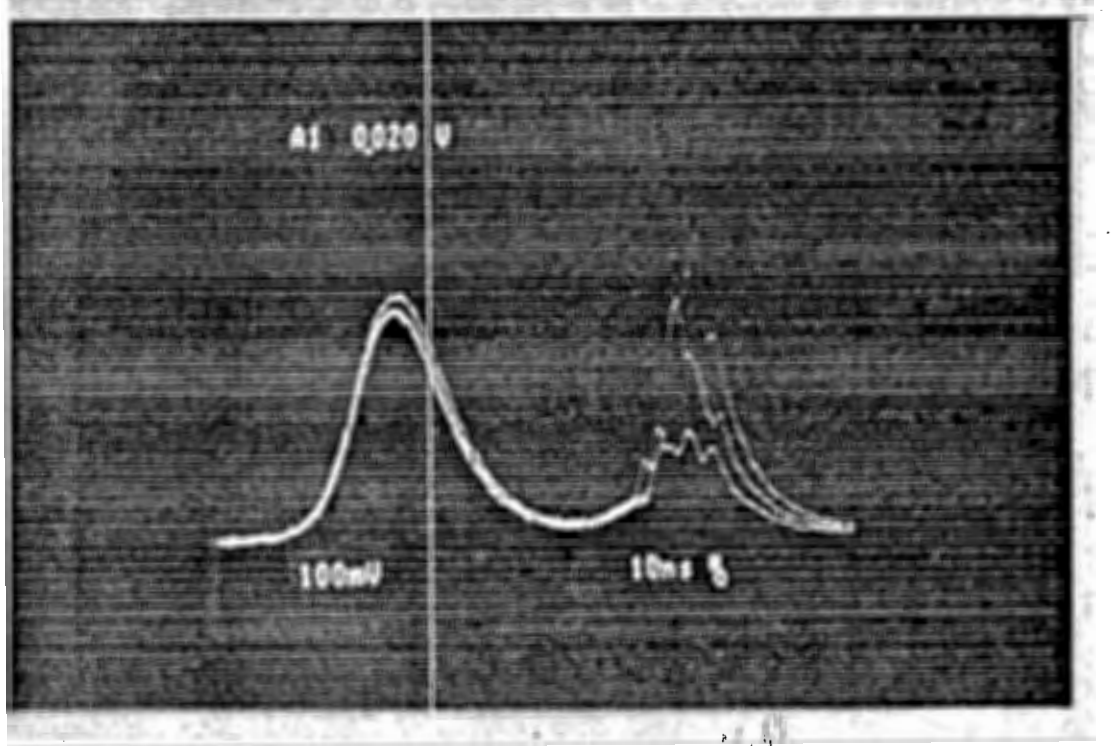

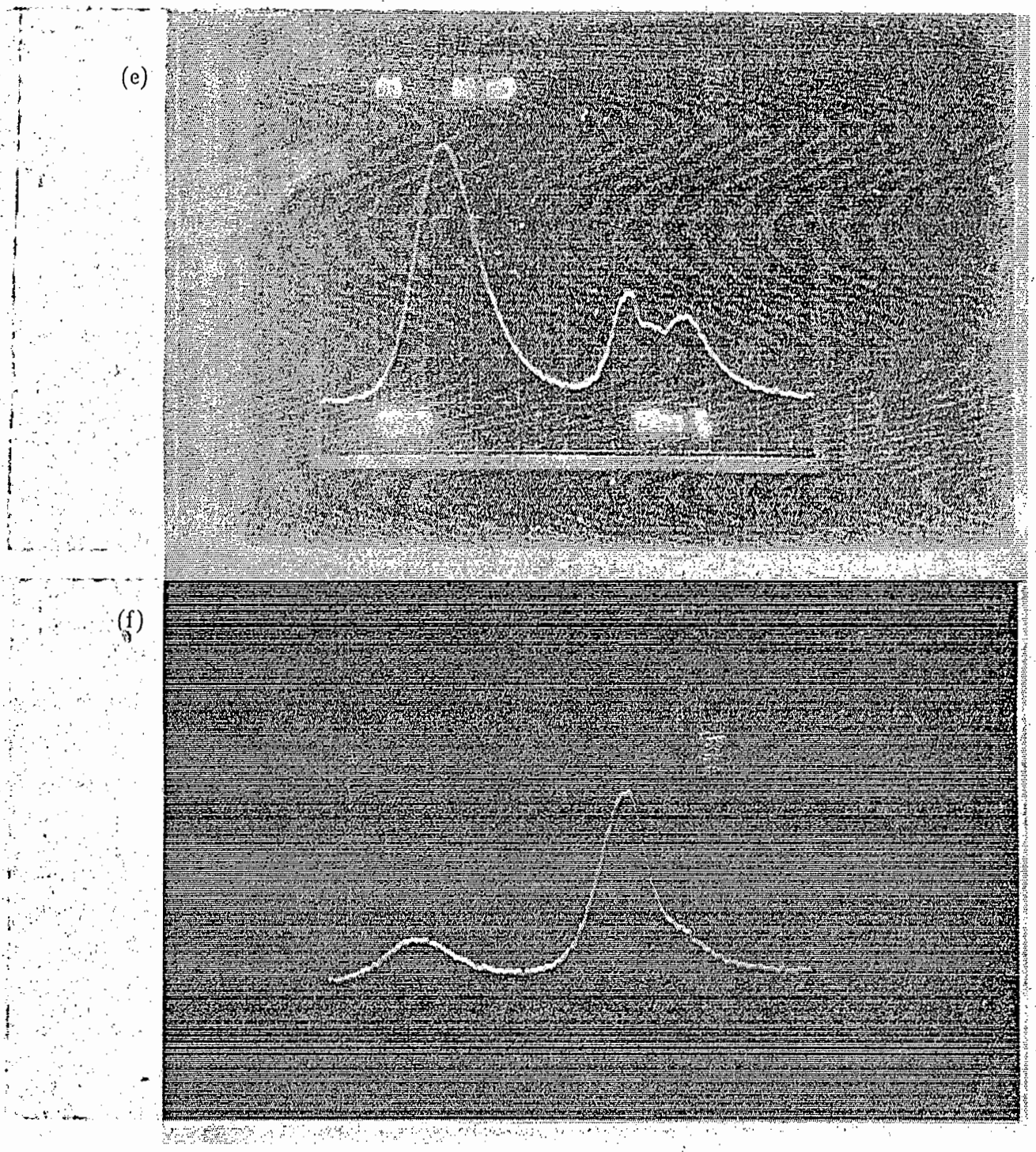
(e)
(f)

(i)

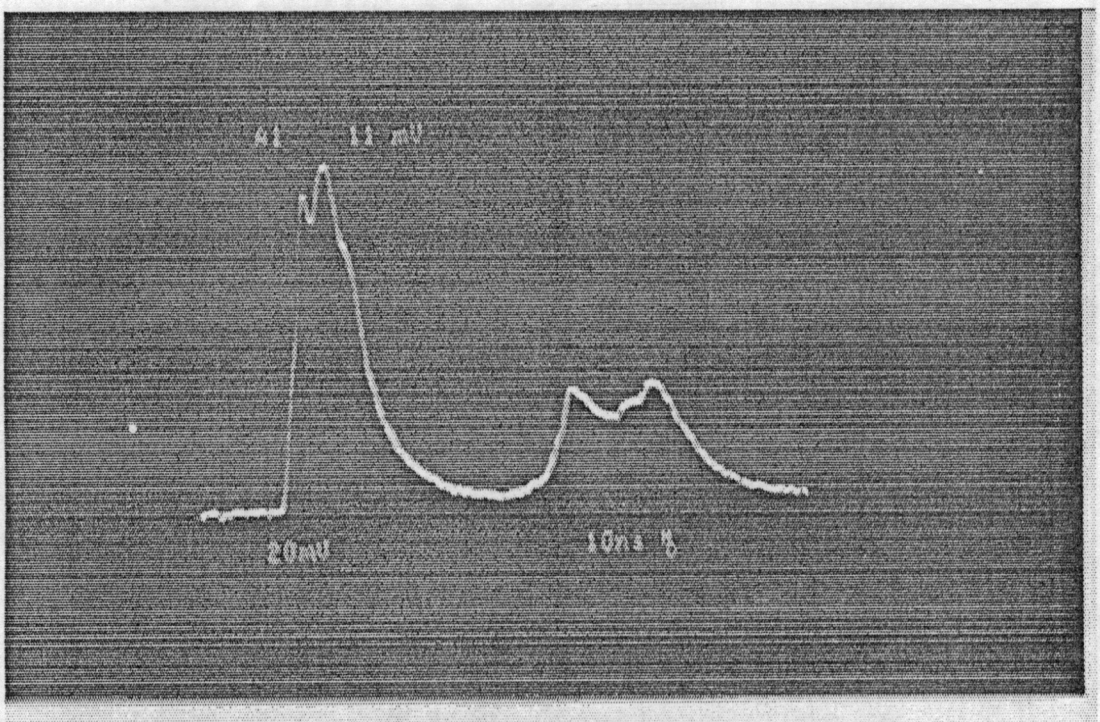

(j)

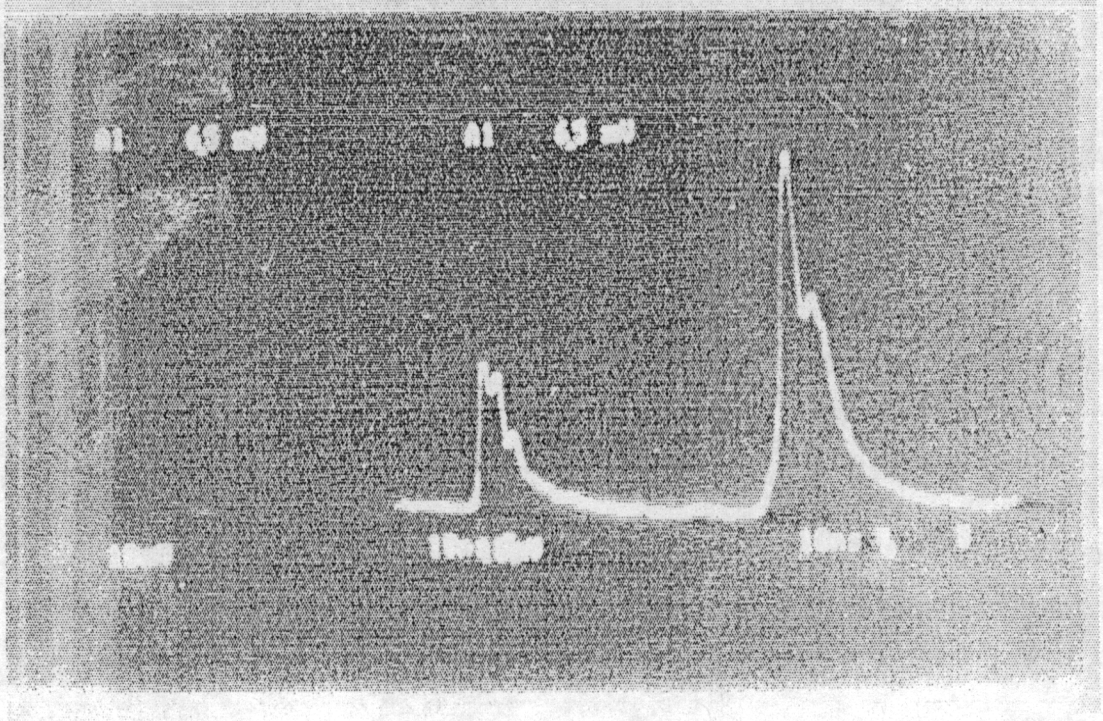

(k)

(l)

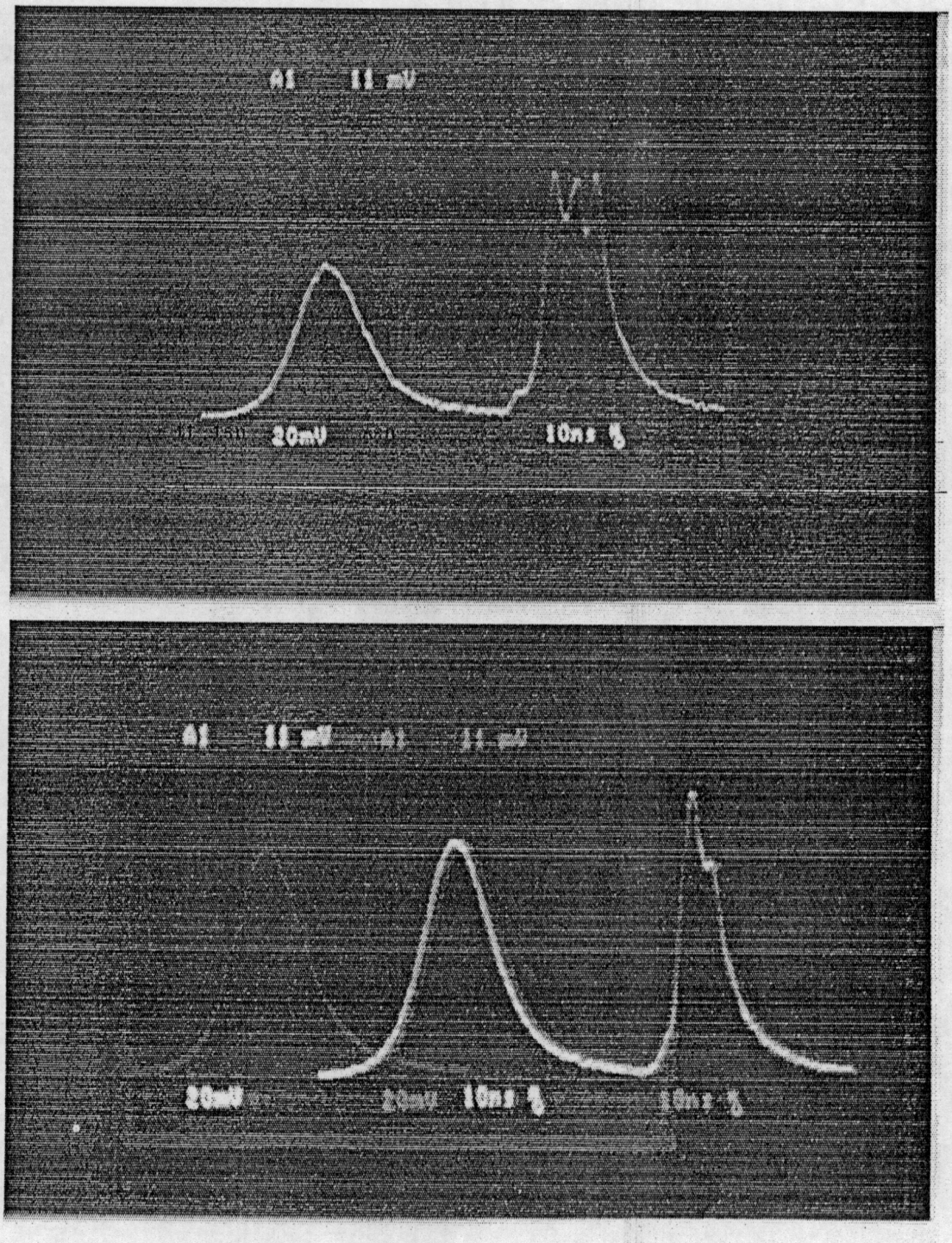

Figure 0.1: illustrates a selection of temporal traces which are combinations of various of the input and ouput beams. We list the combinations in each trace, identifying the left-hand trace first. The following labels are used: P–incident pump, T–transmitted pump, B–backward Stokes, F–forward Stokes and A–forward anti-Stokes. (a)–(c) PT, (d) PA, (e)–(h) PT, (i) BT, (j) BF, (k) PB and (l) PF

turing worthwhile shots. The captured shots represent chance recordings in that the nonreproducibility of the pump (fig. 3.2 (c)) and the variability of the output (fig. 3.2 (d)) was often such that many recorded traces were rendered useless. It would be useful, in this regard, to be able to record a sequence of shots in real time and then to discard any useless shots.

We proceed now with a presentation of the results of the energy conversion measurements together with a theoretical comparison.

3.1.1 The Interaction Region

Before we can continue we must examine the interaction region with our focused geometry. A theoretical discussion was presented in section 2.3.1. For a pump beam of diameter $7\,mm$, focused into the centre of a $500\,mm$ long cell by a $f = 300\,mm$ lens, the interaction region can be considered to be a cylinder of cross-section $A \simeq 6.62 \times 10^{-6}\,cm^2$ and length $L' = 0.39\,cm$. The results of Appendix B as well as eqn. 2.73 have been used.

However, this leads to extremely high pump intensities which in turn lead to unnaturally high gains. As was shown on page 50 a pump laser of power $\simeq 1\,MW$ focused in this way results in a gain of $gI\,L \simeq 150$ which is unnaturally high as will become apparent from our results. The problem can be traced to the development of the theory of focused propagation through the Raman medium i.e. section 2.3.1. The problem lies in the assumption of a steady state interaction. It will be informative to examine, in detail, the reason for the breakdown of this model. It is evident that for conditions such as ours, the pump beam will become sufficiently intense to initiate the SRS process long before it reaches the interaction region. It therefore follows that the pump will become depleted on its passage to the focal region so that

it will never attain the predicted high intensities at the focus. In order to account for this we should include the time dependence in the propagation equations. The only way of successfully incorporating the effects of focusing in the time-dependent equations is by computer simulation [46, 41].

The transient theory presented in this work (see section 2.5) does not include the effects of focusing and relies on knowledge of the steady state Raman gain. If the steady state Raman gain calculated above is used, then it is seen from eqn. 2.109 that we are in the transient regime for a 15 ns pump pulse. However, none of our results are consistent with this assumption. The only possible use of our transient theory is if a better estimate of a steady state Raman gain can be achieved. Even with a steady state gain of $gIL = 30$ (that usually quoted for amplification), we are still in the transient regime for our pressure range (i.e. $gIL/\tau\Gamma_{FWHM} > 1$). From our photographs (figure 3.2), however, it is clear that the depletion of the pump must be included in any analysis and our transient theory is therefore not applicable. This is due to the fact that our calorimeter used for the energy measurements only permitted us to measure energies in the depleted pump regime. Our comparison of experiment and theory will, therefore, be limited to one in which only a qualitative agreement (if any) with the general trends of the relevant steady state theory (section 2.2.4 and 2.2.5) is sought.

3.1.2 Stokes Noise

Since we are involved in the generation of Stokes radiation from noise, we use eqn. 2.19 together with eqn. 2.54 to estimate the initial Stokes intensity. However, in the light of our above discussion relating to the interaction region, we set the $(A/\lambda L)^2$ factor to unity and work instead with the initial

Stokes power: $P_2(0) = A\,I_2(0)$, so that no reference is made to the (unknown) interaction region. This together with the relevant pump power can be used to calculate the input intensity ratio δ defined in eqn. 2.38.

If we assume a square wave pump pulse of duration τ, then we may use the results of section 2.3.2 (i.e. eqn. 2.81) to obtain the average power in the beam as:

$$P_{av} = E_t[1 - e^{-2}]/\tau \tag{3.1}$$

where E_t is the total energy in the beam as measured by the calorimeter. One of the shortcomings of this square wave pulse approximation is evident in traces (a), (b) and (f) of figure 3.2, in which the transmitted pump is included. In these cases it is seen that the pump is only depleted near its peak, well above the level corresponding to the average energy. In our approximation of the pump pulse as a square wave, no SRS (and hence no depletion) would have been predicted. For our purposes, however, we shall content ourselves with this approximation even in the light of a further shortcoming described in the next section. We can therefore estimate the input intensity ratio as:

$$\delta = \frac{P_{av}\,(\text{pump})}{(P_2(0) \simeq \frac{1}{2}\Gamma\hbar\omega_2)} \tag{3.2}$$

It should be noted that δ is a function of pressure via eqn. 2.54.

3.1.3 Duration of the Output

The duration (FWHM) of the pump pulse was found to be 15 ns over the whole energy range. However, the duration (FWHM) of the backward Stokes output was found to depend on the pump energy. Table 3.1 illustrates the observed trend; that as the pump energy was increased, the duration of the

Pump Energy (mJ)	Stokes Duration (ns)
10.1	11.5
15.0	12
21.7	15
32.8	15
42.0	17.5
58.1	19
65.6	20

Table 3.1: contains the duration of the backward Stokes output at various pump energies

backward Stokes output increased from a value below that of the pump to a value well above that of the pump.

This trend is consistent with the SRS being initiated at a fixed power level and with the pump having a Gaussian intensity profile. Thus this is another shortcoming of the square wave pulse approximation. For a relatively low pump energy, there will not be amplification over the full duration of the pump. As the pump energy is increased, the duration over which significant gain is experienced becomes larger until the FWHM duration of the backward Stokes output becomes even longer than that of the pump. This is well illustrated in traces (h), (f) and (i) of fig. 3.2. In the first of these, the trace of the transmitted pump at a low pump energy indicates a small depletion region overwhich high gain was experienced, whilst the second trace, which was obtained at a much higher pump energy, reveals that high gain was experienced over a much longer period. In the last of the above traces, in which the backward Stokes output appears together with the transmitted (depleted) pump at a relatively low energy, the FWHM duration of the

backward Stokes output is seen to be less than that of the pump. Trace (l) of the same figure is an illustration of the same effect in the forward direction. The characteristic sharp rise and fall-off following the pump [12, 34], of the Stokes output in either direction is evident in these and many of the other traces of figure 3.2.

For the sake of simplicity, however, we assume that all the backward Stokes output is of the form of a square wave pulse of duration $15\,ns$, as in the case of the pump.

3.1.4 Energy Conversion Measurements

We first investigated the dependence of the backward Stokes output on pressure. The total pump energy was fixed at $70.5\,mJ \Rightarrow P_{av} \simeq 4.1\,MW$ for this investigation. The results are displayed in figure 3.3 in which we have plotted the logarithm of the ratio of the measured output power to the initial Stokes noise versus the hydrogen pressure. From this figure it is evident that our measurements were restricted to the saturation/depletion gain region of SRS. We were unable to fit the relevant equation for backward SRS (i.e. eqn. 2.7) to our experimental results. We did, however, fit the relevant forward equation, eqn. 2.37, for comparison. The fit seemed reasonable at higher pressures (i.e. $P > 10\,\text{atm}$). However, when we used the relevant fitted parameters, obtained in this exercise, to fit curves to our other experimental results, the results were dismal. We are therefore unable to compare our experimental results with any of our theory in a consistent manner.

Next we investigated the effect of pump energy on the backward Stokes energy. We repeated the measurements at three different pressures, namely 41 atm, 31 atm and 21 atm. The results are illustrated in fig. 3.4 from which

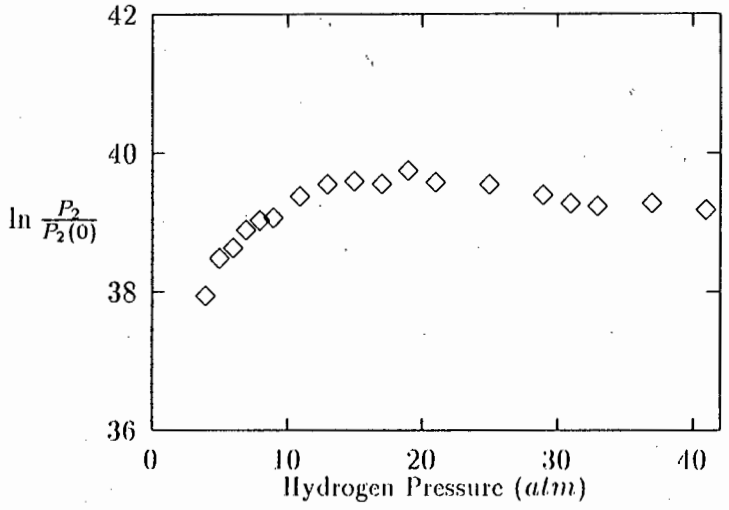

Figure 3.3: illustrates the effect of pressure on the backward Stokes output energy. The results were obtained with a pump energy of $70.5\,mJ$.

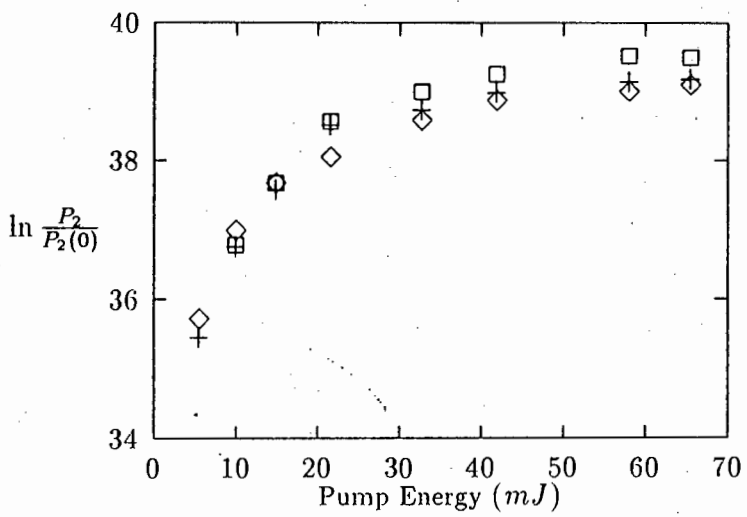

Figure 3.4: illustrates the effect of pump energy on the backward Stokes output energy. The results were obtained with at hydrogen pressures of (a) 41 atm (diamonds) (b) 31 atm (crosses) and (c) 21 atm (squares).

it is seen that they follow the same trends. The general shape of both the above curves is reminiscent of steady state behaviour.

3.1.5 Anti-Stokes and Higher Order Output

It was generally found that anti-Stokes radiation accompanied the Stokes output for our conditions (i.e. $f = 300\,mm$ focusing into the cell). Whenever the forward scattered Stokes radiation became visible, it was invariably partnered by an amount of anti-Stokes radiation when viewed at position T_3 in fig 3.1. It was also found that the anti-Stokes radiation was collimated in the same fashion as the pump i.e. no cones were evident. A trace of the anti-Stokes output in the forward direction appears in fig. 3.2 (d). It has

been assumed in the past that parametric coupling in the backward direction is not possible [27]. From our theoretical considerations in section 2.4.2, this would seem to be the case. However, we found that at the higher pump energies the backward Stokes output was partnered by a diffuse anti-Stokes output. We are only aware of one other such observation [54]. We diverted the anti-Stokes radiation into a spectrometer and measured an equal Raman shift of $\approx 4155\,cm^{-1}$ in either propagation direction. Even more interesting was that the backscattered anti-Stokes radiation was not collimated (as all the other visible output was), upon exiting the cell. It was found that it was brought to a focus outside the cell at a position which was consistent with it having originated at the far end of the Raman cell. This accounted for the diffuse nature of the backscattered anti-Stokes output (when it was observed). It was further found that the anti-Stokes output in both directions became more intense at lower pressures as expected for a parametric process [21]. We did not obtain any quantitative measurements of the anti-Stokes outputs. This very interesting observation warrants a much more careful investigation.

Since we do not have a good understanding of the interaction region and hence the gain involved, we can make no quantitative theoretical calculations. However, in the light of the increase in output energy with decreasing pressure, it does seem likely that the anti-Stokes radiation in both directions is due to parametric coupling .

Detection of higher order Raman effects was beyond our capabilities since we could not detect radiation in either the infrared (2nd Stokes output) or the ultraviolet (2nd anti-Stokes output). There was, however, some evidence that such processes were occurring. This can be seen from figure 3.5 in which

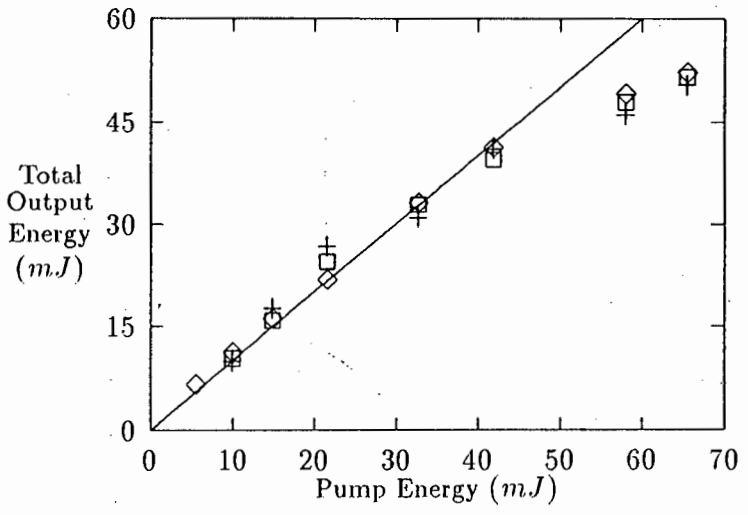

Figure 3.5: illustrates the relationship between the measured total output energy (backward Stokes and all forward output including transmitted pump) and the input pump energy (solid line). The measurements were made at 41 atm (diamonds), 31 atm (crosses) and 21 atm (squares).

the input pump energy is plotted together with the total of output energies at three different pressures. They are seen to overlap within error ($\simeq$ 10%) for most pump energies except at the highest energies. A similar observation has been made by Brueck et al. [26].

Although the backward anti-Stokes radiation could not be included (due to its diffuseness at the measuring site), it is unlikely that it was intense enough to account for the difference. It seems more likely that the backward Stokes radiation became intense enough to generate second Stokes radiation. This is obviously a tentative speculation which would have to be checked out more carefully.

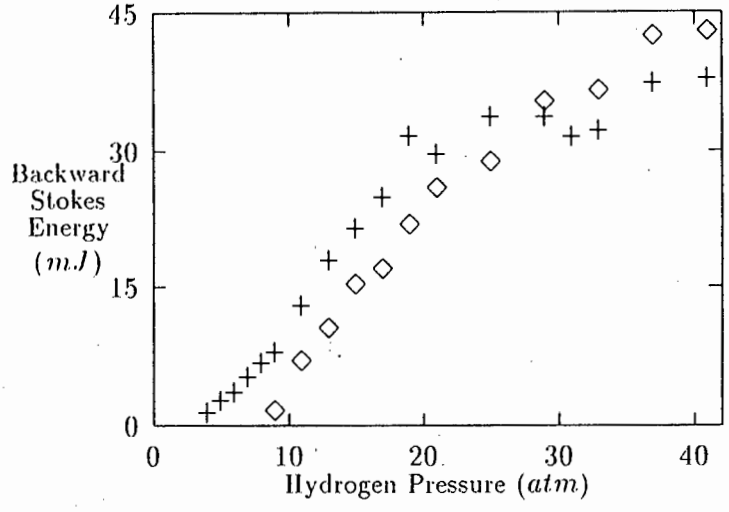

Figure 3.6: illustrates the effect of hydrogen pressure on the backward Stokes output energy. The results with the present focusing conditions ($f = 160\,mm$– diamonds) are compared with the previous results obtained with an $f = 300\,mm$ focusing arrangement (crosses).

3.1.6 Focusing Conditions

We attempted to perform the same experiments under different focusing conditions. Unfortunately due to the constraint of a cell of fixed length, this proved a difficult task. We succeeded in repeating the measurements under tighter focusing conditions ($f = 160\,mm$). The results are presented in figure 3.6, illustrating the effect of pressure for a fixed pump power ($P_{av} \simeq 4.1\,MW$ as before), and figure 3.7 in which the effect of varying the pump energy at a fixe pressure of 41 atm is illustrated. In both cases the results are compared with the previously obtained results.

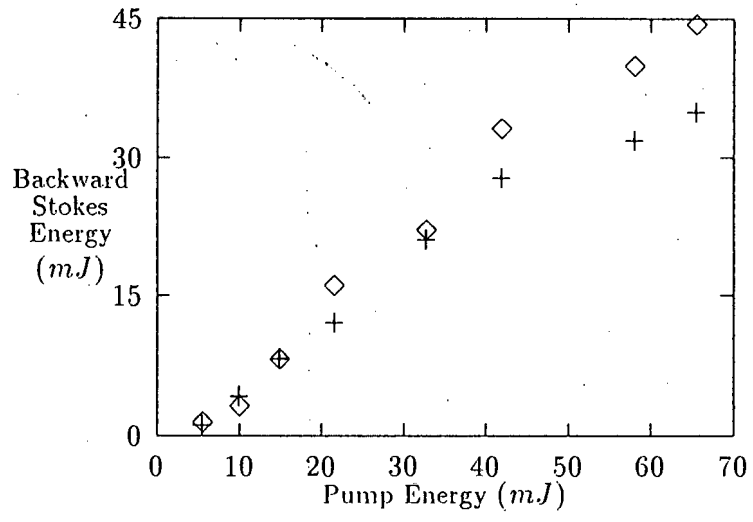

Figure 3.7: illustrates the effect of pump energy on the backward Stokes output energy for a fixed hydrogen pressure of 41 atm. As before, the diamonds represent the present focal conditions ($f = 160\,mm$) and the crosses represent the results with the previous focal conditions ($f = 300\,mm$).

Figure 3.7 can be compared to the results obtained by Brueck et al. [26]. They, however, used a broadband pump which thus explains their observation of more SRS output in the forward direction (due to the longer coherence length for forward SRS, see eqn. 2.88), and so it is only the general trend of the results which are comparable. The effects of focusing are again seen to play a crucial role. The parametric coupling with the anti-Stokes radiation is affected by the different focusing conditions, possibly accounting for the observation. Figure 3.6 may have a similar explanation, with the added influence of the variable pressure also affecting the phase-matching of the parametric coupling. It is obvious that a thorough examination of all the output fields under various focusing condtions is necesssry to clarify the situation. A more comprehensive theoretical model of the process with a focused geometry is also required.

We failed in our attempt to repeat the measurements with softer focusing ($f = 500\,mm$) because the focal region was too close to the exit window of the cell, which resulted in a burnt exit window. In order to properly investigate the effect of the focusing conditions, a cell of variable length is of paramount importance.

3.1.7 Temporal Structure of the Output

There is evidence of nanosecond timescale structure on the temporal traces of the various SRS outputs in fig. 3.2 (i.e. traces (i)–(l)). This structure is comparable in form to the observations of Kachen et al. [46]. Temporal 'relaxation' oscillations of the output energy have been predicted [20] and observed [46]. However, the timescale involved was considerably smaller than that of our phenomena. Thus a comparsion with our observations was

not afforded.

Since the observed phenomenon is at the limit of the resolution of our scope, we are not able to confidently interpret their significance. It would seem that a similar qualitative explanation to that proposed for the 'relaxation' oscillations is plausible. Hence the phenomenon may be the manifestation of the exchange of energy between the pump and the various beams generated by SRS. Once again we find that in order to understand the process, we require a better model of the interaction region and its dynamics. We discuss ways of achieving this in the concluding Chapter.

If the observed nanosecond timescale phenomenon is indeed real, then we can expect that the linewidth of the Stokes outputs will be broadened with respect to that of any steady state prediction. We discuss the results of our investigation into the backward Stokes linewidth in the following section.

3.2 Linewidth Measurements

3.2.1 Introduction and Aim

The aim of this investigation was to measure the dependence on pump energy and pressure of the linewidth of the backward SRS at $683nm$, resulting from a variable pressure H_2-filled cell being pumped by a Nd:YAG ($532nm$) laser. The linewidth measurements were made with the use of a Fabry-Perot interferometer.

The available Fabry-Perot interferometer restricted the determination of the linewidths to a method of electronic recording of the fringe system. A 1024 channel optical multichannel analyser (O.M.A.) was used to record the fringe system. It will thus be instructive to proceed with the theory of linewidth determination by this method.

3.2.2 The Theory of the Fabry-Perot Interferometer

General

For spectroscopic purposes the geometric description of the Fabry-Perot interferometer is sufficient [55] and more instructive than a complete cavity-mode analysis describing the distribution of the field over the plates. We concern ourselves solely with the transmitted intensity distribution.

It is easy to show that the transmitted intensity through the interferometer is:

$$I_T = \left[\frac{T}{1-R}\right]^2 \mathcal{A}(\psi) \tag{3.3}$$

where T and R are respectively the transmitted and reflected intensity co-

efficients, and $\mathcal{A}(\psi)$ is the Airy function:

$$\mathcal{A}(\psi) = \frac{1}{1 + F\sin^2(\frac{\psi}{2})} \tag{3.4}$$

where F is the *Coefficient of Finesse* [56] or the *contrast* [57] and is given by :

$$F = \frac{4R}{(1-R)^2} \tag{3.5}$$

and

$$\psi = \phi + \varepsilon = 2\pi(2\mu t\cos\theta)/\lambda_0 + \varepsilon \tag{3.6}$$

is the phase lag between successive beams for a cavity of refractive index μ and length t. Here ε is the additional phase lag due to reflections at the surfaces. It can be seen from eqn. 3.3 that for no scattering or absorption losses in the cavity $T + R = 1$. Thus for this perfect case the transmitted intensity is just the Airy function itself. However, in real interferometers, losses do inevitibly arise (i.e. $T + R < 1$) and are taken into account by eqn. 3.3.

To obtain a good fringe pattern with maxima of high relative intensity (i.e. sharp fringes), high reflectivities are required. High reflectivities can be seen to give rise to large values of F (for $R = 0.85 \Rightarrow F \cong 151$) which in turn via eqn. 3.4 can be seen to give sharp fringes.

The Transmitted Fringe Pattern

The intensity distribution in the transmission focal plane (see fig. 3.8) is given by:

$$I(\psi) = \left(\frac{T}{1-R}\right)^2 \frac{I_0}{[1 + F\sin^2(\frac{\psi}{2})]} \tag{3.7}$$

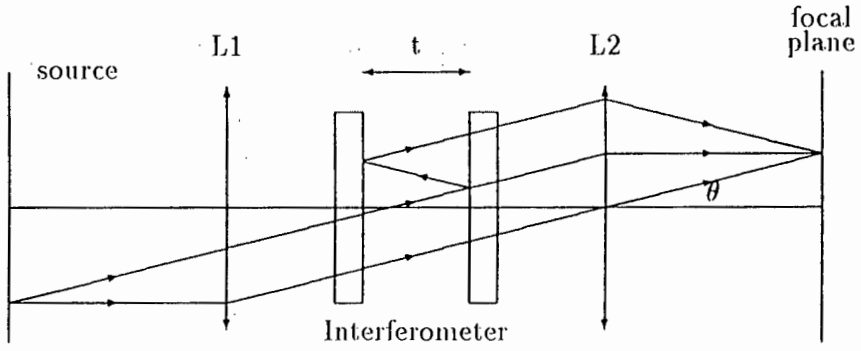

Figure 3.8: The basic set-up for viewing the transmitted fringe pattern of a Fabry-Perot interferometer

where I_0 is the illumination in the focal plane in the absence of the interferometer. From eqn. 3.7 it is apparent that maxima occur for $\psi = 2\pi n$ where n is an integer. The usual configuration of cylindrical symmetry about the optical axis of the arrangement obviously results in a fringe pattern of concentric bright rings of angular radius θ (see fig. 3.8) given by:

$$\psi = \frac{4\pi\mu t}{\lambda_0}\cos\theta + \varepsilon = 2\pi n \tag{3.8}$$

Thus

$$2\mu t\cos\theta = \lambda_0(n - \frac{\varepsilon}{2\pi}) \tag{3.9}$$

from which it can be seen that the phase change due to reflections does not affect the fringe pattern, but does cause a shift in the fringe positions. This is equivalent to a small shift in the interferometer spacing. This can obviously be ignored for high orders of interference, which is the case in most practical cases. Indeed for our purposes, this effect will be neglected

in the rest of the discussion. Consequently,

$$\psi = \phi_n = 2\pi n = \frac{4\pi\mu t}{\lambda_0}\cos\theta_n \tag{3.10}$$

and hence,

$$\theta_n = \arccos\left(\frac{n\lambda_0}{2\mu t}\right) \tag{3.11}$$

From fig. 3.8 the radius of the circular fringes can be seen to be $f\theta_n$ where f is the focal length of the lens L_2. For illumination with quasi-monochromatic light, the half-width of the fringes at half-intensity is given by:

$$F\sin^2(\phi_{\frac{1}{2}}/2) = 1 \tag{3.12}$$

which for sufficiently large F enables the approximation of the sine by its angle, yielding:

$$\phi_{\frac{1}{2}} = \frac{(1-R)}{\sqrt{R}} \tag{3.13}$$

Recall that for large F, the fringes are narrow and hence $\phi_{\frac{1}{2}}$ is small and the above approximation is valid. Now since there is a 2π change of phase ϕ between successive orders, the reciprocal of the full fringe width at half maximum intensity (FWHM) expressed as a fraction of an order can be defined:

$$N_R = \frac{2\pi}{2\phi_{\frac{1}{2}}} = \frac{\pi\sqrt{R}}{1-R} = \frac{\pi}{2}\sqrt{F} \tag{3.14}$$

and is called the ideal *reflectivity finesse* of the interferometer [55]. This conveniently expressed ratio encapsulates the increase in fringe sharpness as the reflectivity increases. This quantity defines the relative fringe width to be expected for ideally flat plates with the given reflectivity. In practice, plate imperfections as well as the way in which the instrument is used, will alter this property of the instrument.

Free spectral range and Resolving power

Consider the effect of the interferometer under illumination by quasi-monochromatic light at λ_0 as well as at a slightly different wavelength of $\lambda_0 + \delta\lambda$. Two distinct fringe systems will be formed.

Assuming the same refractive index for these two closely spaced lines, it is apparent from eqn. 3.10 that for a fixed angle of incidence θ, these two wavelengths have a difference of phase delay given by:

$$| \delta\phi | = 4\pi\mu t \cos\theta \frac{\delta\lambda}{\lambda_0^2} \tag{3.15}$$

where $\delta\lambda/\lambda_0^2$ is simply the wavenumber difference of the two wavelengths. When the separation between the two wavelengths is increased, it will eventually reach the stage where the n^{th} order of interference for λ_0 overlaps the $(n+1)^{th}$ order of interference for $\lambda_0 + \delta\lambda$. Obviously (from eqn. 3.12) when this happens, $| \delta\phi | = 2\pi$. Hence from eqn. 3.15,

$$\left[\frac{\delta\lambda}{\lambda_0^2}\right]_{2\pi} = (2\mu t \cos\theta)^{-1} \tag{3.16}$$

For normal incidence (i.e. $\cos\theta = 1$), this is defined as the *Free Spectral Range* of the interferometer:

$$\Delta\kappa_{fsr} = \frac{\delta\lambda}{\lambda_0^2} = \frac{1}{2\mu t} \tag{3.17}$$

This is just the wavenumber separation which for fixed plate separation, would result in the exact overlap of successive orders of interference for two spectral lines thus separated. The usefulness of this quantity can be illustrated as follows: consider the wavenumber difference between two close lines,

$$\Delta\kappa = \frac{\delta\lambda}{\lambda_0^2} = \left|\frac{\delta\phi}{2\pi}\right| (2\mu t \cos\theta)^{-1} \tag{3.18}$$

which follows from eqn. 3.15, but upon using eqns. 3.16 and 3.17 this yields:

$$\Delta\kappa = \left|\frac{\delta\phi}{2\pi}\right| \Delta\kappa_{fsr} \tag{3.19}$$

and hence knowing the interval between the fringe patterns as a fraction of an order (i.e.| $\frac{\delta\phi}{2\pi}$ |) enables the wavenumber difference to be found. The details of this method follow in a later section.

As | $\delta\phi$ | decreases, the fringe patterns of the two lines approach one another and eventually overlap. Of interest here is the point at which the two fringe patterns are just resolvable as this will be a measure of the *resolving power* of the interferometer given by $\frac{\lambda}{\delta\lambda}$ where $\delta\lambda$ is the wavelength difference of the two lines. Various criteria for resolution have been put forward, notably that for prisms and grating instruments proposed by Lord Rayleigh. Instead of arbitrarily imposing this condition for this instrument, a somewhat simpler method will be employed. For two lines of equal intensity, the corresponding fringe systems are considered resolved if they coincide at their half-intensity positions (i.e. set | $\delta\phi$ |= $2\phi_{\frac{1}{2}}$ in eqn. 3.15). For large F this yields a peak-to-saddle ratio of 0.833: 1, compared to a saddle intensity 0.811 of the peak for the Rayleigh criterion [56].

Using this criterion and from eqns. 3.13&3.14, resolution of the two equal intensity lines is achieved if

$$| \delta\phi |_{min} = 2\phi_{\frac{1}{2}} = 2\pi/N_R \tag{3.20}$$

Hence the *resolving limit* (minimum resolvable wavenumber separation) of the instrument is given (using eqn. 3.18) by:

$$\Delta\kappa_{min} = \Delta\kappa_{fsr}/N_R \tag{3.21}$$

which is just the free spectral range divided by the finesse. It should be noted, however, that this resolving limit is for perfect plates and vanishingly

small detector aperture etc. A discussion on choice of aperture can be found in ref [55].

3.2.3 Analysis of Recorded Fringe Systems

The analysis will concentrate on the particular area of interest, i.e. the determination of the spectral linewidth of the source. Two approaches will be discussed, both of which are approximate methods. The first is based solely on the ratio of fringe width to fringe separation. It does, however, require that the *free spectral range* of the interferometer be known. The second approach depends on the determination of the parameters of an Airy function which is fitted to the recorded profile.

Determination of Frequency intervals

Two closely separated lines A and B of wavenumber separation $\Delta\kappa$, will result in two fringe systems separated by a difference in order of interference δn. This difference which may be a small integer plus a fraction is given by:

$$\Delta\kappa = \delta n \Delta\kappa_{fsr} = \frac{\delta n}{2t} \tag{3.22}$$

In order to relate this to the recordings, we must first look more closely at the phase dependence of the recorded patterns. For the intensity profile along a diameter we are particularly interested in the effect of different values of the fractional phase at the centre of the pattern $\varepsilon_c (< 2\pi)$ for fixed plate separation and varying θ. Consider the phase at the centre ot the pattern:

$$\phi_c = \frac{4\pi\mu t}{\lambda_0} = 2\pi n + \varepsilon_c \tag{3.23}$$

It is obvious that in general the order of interference at the centre of the pattern is a fraction. It can only be an integer when the optical path dif-

ference is a whole number multiple of half-wavelengths. For small angles of incidence θ, the small angle approximation to $\cos\theta$ in eqn. 3.10 yields a phase of:

$$\phi = \phi_c(1 - \theta^2/2) \tag{3.24}$$

where eqn. 3.23 has been used.

The squares of the angular radii of successive bright rings from the centre of the pattern are:

$$\begin{aligned}
\theta_1^2 &= 2\phi_c^{-1}(\phi_c - \phi_1) = \frac{2\varepsilon_c}{(2\pi n + \varepsilon_c)} \\
\theta_2^2 &= 2\phi_c^{-1}(\phi_c - \phi_2) = \frac{2(\varepsilon_c + 2\pi)}{(2\pi n + \varepsilon_c)} \\
\theta_3^2 &= 2\phi_c^{-1}(\phi_c - \phi_3) = \frac{2(\varepsilon_c + 4\pi)}{(2\pi n + \varepsilon_c)}
\end{aligned} \tag{3.25}$$

which are obtained from the conditions for maxima $\phi_1 = 2\pi n, \phi_2 = 2\pi(n-1)$ and $\phi_3 = 2\pi(n-2)$ respectively. Hence it is evident that the difference between the squares of successive angular radii are equal, with magnitude

$$(\theta_{i+1}^2 - \theta_i^2) = \frac{4\pi}{(2\pi n + \varepsilon_c)} \tag{3.26}$$

From this we can see that for a fringe forming lens of focal length f, the difference of squares of the fringe diameters of the i^{th} and $(i+1)^{th}$ bright rings from the centre for spectral line A is given by:

$${}_aD_{i+1}^2 - {}_aD_i^2 = \frac{16\pi f^2}{(2\pi n_a + {}_a\varepsilon_c)} = \Delta_a \tag{3.27}$$

For large order of interference n_a, Δ_a reduces to $\frac{8f^2}{n_a}$. Notice too that (using eqn. 3.25) for the fringe system of line A, the fractional order at the centre is given by:

$${}_a\varepsilon_c/2\pi = [{}_aD_{i+1}^2/(8f^2/n_a)] - i \tag{3.28}$$

This can be rewritten with the help of eqn. 3.27 to yield:

$$
\begin{aligned}
{}_a\varepsilon_c/2\pi &= [{}_aD_{i+1}^2/({}_aD_{i+1}^2 - {}_a D_i^2)] - i \\
&= [{}_aD_{i+1}^2/\Delta_a] - i
\end{aligned}
\tag{3.29}
$$

The results similarly hold for spectral line B.

$$
{}_bD_{i+1}^2 - {}_b D_i^2 = \frac{8f^2}{n_b} = \Delta_b \tag{3.30}
$$

and

$$
{}_b\varepsilon_c/2\pi = [{}_bD_{i+1}^2/\Delta_b] - i \tag{3.31}
$$

For closely separated lines, Δ_a and Δ_b are essentially the same and the difference is neglected. The actual order of interference at the centre of the fringe pattern is $n - \varepsilon_c/2\pi$. Finally we obtain the order difference δn between the two lines:

$$
\begin{aligned}
\delta n &= (n_a - {}_a\,\varepsilon_c/2\pi) - (n_b - {}_b\,\varepsilon_c/2\pi) \\
&= (n_a - n_b) - ({}_a\varepsilon_c - {}_b\,\varepsilon_c)/2\pi
\end{aligned}
\tag{3.32}
$$

which for lines producing patterns with overlapping fringes of the same order of interference (i.e. $n_a = n_b$), yields

$$
\delta n = ({}_b\varepsilon_c - {}_a\,\varepsilon_c)/2\pi \tag{3.33}
$$

But from eqns. 3.29 & 3.31 we have

$$
({}_b\varepsilon_c - {}_a\,\varepsilon_c)/2\pi = ({}_bD_{i+1}^2 - {}_a\,D_{i+1}^2)/\Delta \tag{3.34}
$$

which implies that $({}_bD^2_{i+1} - {}_aD^2_{i+1})$ is a constant which we call δ_{ba}. Thus δ_{ba} and Δ, which may be readily measured from recorded fringe patterns, and the difference in order of interference

$$\delta n = \frac{\delta_{ba}}{\Delta} \tag{3.35}$$

are easily found for fringe systems due to lines A and B with overlap of the same order. This quantity can now be inserted into eqn. 3.22 at the begining of this discussion and hence the wavenumber separation of the lines obtained.

If it so happens that a portion of the fringe pattern not including the centre is recorded, or the centre cannot be located, the above analysis is not applicable. Approximate methods are necessitated and it can be shown that the fractional order of interference can be approximated by [55]:

$$\delta n = \frac{2\sigma_{ab}}{\omega_{b-} + \omega_{a+}} \tag{3.36}$$

where σ_{ab} is the separation of the adjacent fringes of the two systems and ω_{a+} and ω_{b-} are the fringe separations of successive fringes of the same system, as illustrated on figure 3.9. The derivation of this relationship appears in Appendix C. It is easy to obtain an accuracy in this way of 1 in 10^3 in the determination of δn [55].

We now describe how this method can be applied to an unresolved fringe profile.

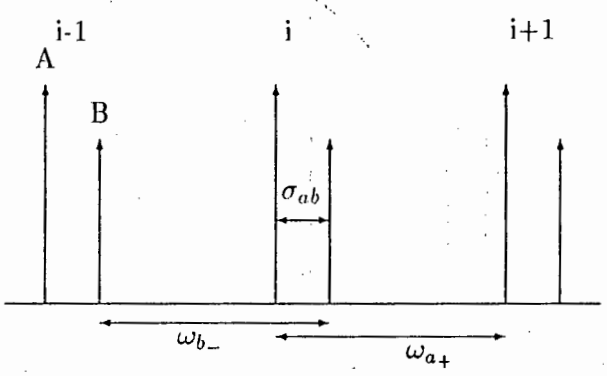

Figure 3.9: Illustration of the quantities used in the approximation of the order of interference when fringes off centre have been recorded.

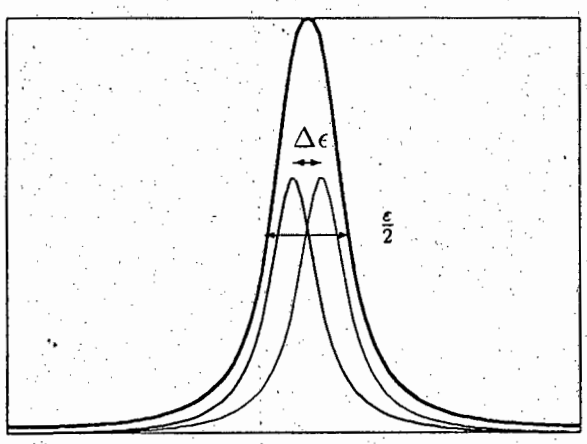

Figure 3.10: The unresolved fringe resulting from the overlapping of two fringes separated by $\Delta\epsilon$

Consider two fringe systems, arising from two monochromatic spectral lines of wavenumber separation $\Delta\kappa$, with the centres of their recorded fringes separated by say $\Delta\epsilon$. Consider the case when these two fringes are not resolved (i.e. $\Delta\kappa < \Delta\kappa_{min}$). The observed single fringe with full width at half maximum $\varepsilon/2$ (note $\Delta\epsilon < \varepsilon/2$) can be seen as being due to a line of wavelength λ_0 and width $\Delta\kappa$, where λ_0 is the average wavelength of the two spectral lines (see figure 3.10). The assumption has been made that a quasi-monochromatic line of width $\Delta\kappa$ at λ_0 can be approximated by two monochromatic lines of separation $\Delta\kappa$ about λ_0. This approximation is easily shown (by summing the two resulting profiles) to be valid for narrow lines i.e. linewidth less than $\Delta\kappa_{min}$ of the interferometer. This then validates the use of the the half height locations as the positions used in the linewidth calculation (i.e. A and B in figure 3.9).

Naturally this will be an overestimate of the linewidth as this analysis is based on the fringes being just unresolved. Obviously if two spectral lines are close enough so that their respective fringe patterns are not resolved, thus having the appearance of having arisen from a spectral line of the average wavelength, then their separation should be less than the minimum resolvable wavelength of the instrument (see fig. 3.10). This limit is, however, as mentioned earlier extremely dependent on the correct set-up of the interferometer as well as on the capture of the profiles. Broadening of the fringes can be effected by incorrect focus or misalignment of the image forming lens system, a badly adjusted interferometer or inaccurate centering of the linear array detector along a diameter of the fringe system.

Fitting an Airy Function to a Recorded Profile

An Airy function can be fitted to a recorded fringe system whenever the intensity profile along a diameter of the fringe pattern has been recorded. The fitted Airy function enables the linewidth of the source to be determined. The method involved will follow the discussion of the fitting procedure.

Equation 3.7 is the basic function to be fitted. However, various modifications to this function are necessary for fitting to a given recorded profile. The generalised Airy function used for profile fitting takes the following form:

$$\mathcal{A}_{fit}(x) = b_g + \frac{I_s}{[1 + F\sin^2\{\frac{\phi_c}{2}\cos(R_f(x + c_s))\}]} \tag{3.37}$$

The argument x refers to the position on the recording (e.g. pixel number in the case of recording by a linear photo-diode array). This is converted to θ, the argument of the cosine in eqn. 3.7 by the factor R_f which depends on the image forming lens as well as properties of the recording device (e.g. length of the array). The factor c_s denotes a centre shift ensuring that the centre of the fitted function coincides with that of the recorded profile. The coefficient of finesse F remains as in eqn. 3.7 and ϕ_c is as defined in eqn. 3.23, this being proportional to the number of half wavelengths in the cavity. The intensity scaling factor I_s normalises the peak transmitted intensity of the fitted curve to correspond to that of the recorded profile. Finally the parameter b_g takes excess background intensity, inherently present in recorded intensity distributions, into account.

A χ^2- fitting procedure enables an Airy function to be fitted to a recorded profile by treating these parameters as variables. Not all of the parameters need be treated as variables for optimization. The choice of which parame-

ters to treat as variables depends on a detailed knowledge of the experimental set-up.

The intensity scale factor is readily estimated directly from the recording as is an approximate background reading b_g. The coefficient of finesse F is calculated directly from eqn. 3.5, although the fringes produced with this value of F will be narrower than the recorded fringes. There are two reasons for this, the first of which is due to instrumental limitations such as the previously discussed plate imperfections. A more reliable estimate may be achieved by considering the quoted plate flatness, usually quoted as λ/m. There are various ways of taking this into account in a modified instrumental finesse N_1. It is generally accepted that for the best results the reflectivity finesse N_R should be in the range of $m/2$ to $m/4$ as determined by plate flatness specifications [55]. The modified instrumental finesse N_1 depends heavily on the type of plate imperfections. The resulting instrument profile may then be incorporated into the fitting procedure by utilising a series representation of the Airy function (see Appendix E), which allows for convolution of the Airy function with Lorentzian and Gaussian functions.

The second factor contributing to the broadening of the fringes is the fact that the radiation passing through the interferometer is not monochromatic but instead has some spectral distribution. Hence, in principle, allowing the parameters describing the convolution with Lorentzian and Gaussian distributions to be variables in the fitting procedure will enable the spectral width of the incident radiation to be determined.

The parameter ϕ_c can obviously be calculated knowing the plate separation and the wavelength of the spectral line under consideration. If the plate separation (or wavelength) is not accurately known, this quantity can

be treated as a variable in the fitting procedure. The same applies to R_f which is generally difficult to determine accurately. Some considerations in the determination of this quantity appear in Appendix D. The centre shift c_s can also be left to vary unless the exact location of the centre is known.

We now present a discussion on the details of the set-up which we used, followed by the presentation of our results.

3.2.4 Experimental Determination of Linewidths

Experimental Set-up Requirements

The signal (Nd:YAG or SRS) is in the form of a parallel coherent beam of diameter $\sim 7mm$. This is expanded over the usable aperture ($\phi \sim 40mm$) of the Fabry-Perot interferometer by means of a Galilean telescope, which could also provide the necessary cone of rays for the interference. It was necessary to record a portion of the resulting fringe system ($4-7$ fringes) using a linear photodiode array of length $25mm$ and an O.M.A. From these recordings, the linewidth of the relevant signal could be determined. This necessitated the expansion of the fringe system image after exiting the interferometer. All manipulations to the fringe system after exiting the interferometer as well as the recording of the fringe system had to be carried out in a light-proof box. Details of the developement of each of these facets of the set-up will be discussed in turn. The set-up for the recording of the fringe system is schematically represented in figure 3.11.

- The Galilean Telescope

  The incoming beam is expanded from $\sim 7mm$ diameter to $\sim 40mm$ diameter. To achieve this, a Galilean telescope was used since it contains no internal focal points as well as allowing the necessary expansion to

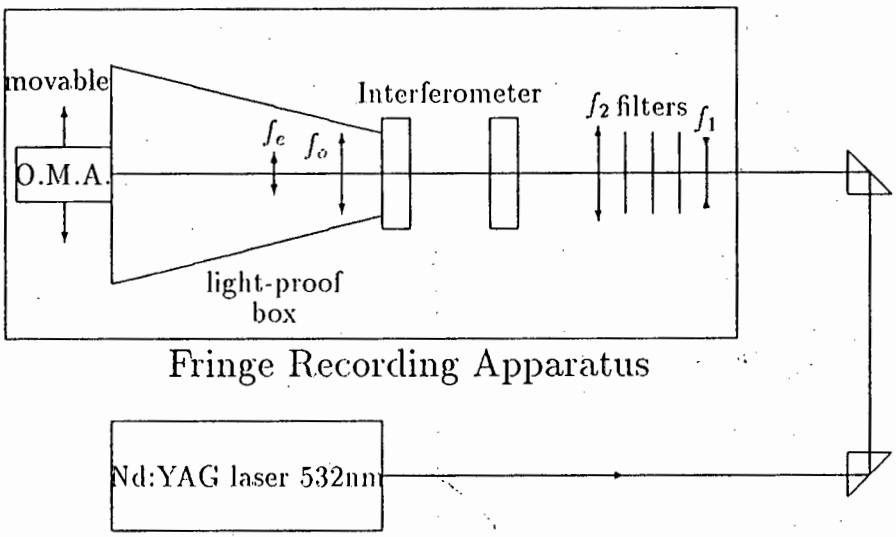

Figure 3.11: Schematic representation of the Fringe Recording Apparatus used to record the fringe pattern from a Fabry-Perot interferometer. The detailed positioning of the lenses appears in the figure in Appendix D.

be achieved in the shortest possible distance. The expansion provided by this arrangement is given by:

$$MP = -\frac{f_2}{f_1} \tag{3.38}$$

Where MP is the transverse magnification of the lens system. With lenses $f_1 = -25mm$ and $f_2 = 300mm$ (see fig 3.11) this gives a more than sufficient expansion of $MP = 12$. The two lenses are mounted on an optical bench with at least one of them being movable. This was used to achieve the necessary plate parallelism as discussed in detail in the following section.

- Image Formation and Expansion

  This was achieved by a simple telescopic arrangement which was nec-

essarily mounted in a light-proof box. The light-proof box was of length $500mm$, which put constraints on the lenses that could be used to achieve the requisite image formation and expansion. These lenses had to be of high quality to provide a good image. A high quality camera lens ($f_o \simeq 58mm$) was selected to form the image. In order to decide on the second lens to be used in the telescope, it was first necessary to have an idea of the size of the image of the fringe system formed by the camera lens. To make an estimate of this, consider the development in Appendix D. Following the same argument, it is possible to estimate the radius of the i^{th} bright fringe of the image formed by the camera lens (i.e. at $k \simeq 60mm$ and no lens f_e).

$$y_{di} \simeq |[(1 - \frac{k}{f_o})R' + k]|\theta_i \tag{3.39}$$

Where k and R' are defined in Appendix D. To estimate the radius of the i^{th} fringe from the centre requires knowledge of the angle (θ_i) of the cone of rays responsible for the appearance of this fringe. For large orders of interference n, ε_c can be neglected in eqn. 3.25 and n can be replaced by $2\mu t/\lambda_o$ (from eqn. 3.23) to yield for small angles θ_i:

$$\theta_i \simeq \sqrt{\frac{\lambda_o}{\mu t}}\sqrt{i-1} \tag{3.40}$$

With a plate separation of $t \simeq 10cm$ and the signal (Nd:YAG at $\lambda_o = 532nm$) passing through the cavity with $\mu = 1$, the angular deviation of the i^{th} fringe from the optical axis can be estimated. For the fourth bright fringe this yields:

$$y_{d4} \simeq 0.5mm \tag{3.41}$$

where $R' \simeq 5000mm$ has been used. To record only the first four fringes with the detector requires a magnification of $MP \simeq 50$. This is given by $MP = \frac{v}{u}$ for a lens with $\frac{1}{u} + \frac{1}{v} = \frac{1}{f_e}$ [58]. Choosing a lens with $f_e \simeq 6mm$ yields a focussed image at $v = 300mm$ for an 'object' (image of the fringe system formed by the camera lens) at $u \simeq f_e$ from the lens. Hence these lenses will suffice for the required telescope. A $6mm$ microscope objective (i.e. as the $f_e \simeq 6mm$ lens) was mounted on a micro-travel plate to ensure that the image was formed on the detector plane. Fine control in the vertical direction enabled us to ensure that the horizontal diameter of the fringe system was coincident with the detector array.

- The Light-proof Box

  As mentioned earlier, all manipulation of the fringe system exiting the interferometer had to be carried out in a light-proof box. It is important to minimize the stray light reaching the detector and thus adding to the 'noise' which would reduce the image clarity. A light-proof box was designed and constructed to meet all the above-mentioned experimental requirements. The box was about $500mm$ long and incorporated an optical bench on which the lenses of the image forming telescope were mounted. The linear photo-diode array detector was mounted at the far end of the light-proof box and was laterally moveable. The linear photo-diode array was positioned on the horizontal diameter of the fringe pattern and the lateral adjustability enabled the fringes far from the centre to be recorded. A schematic representation of the light-proof box appears in the set-up diagram figure 3.11.

Obtaining Plate Parallelism

Initial rough alignment was achieved by allowing the unexpanded laser beam to enter the interferometer directly. Non-parallelism of the plates is indicated by the distinctive comet's tail [59] due to multiple reflections of the beam in the mirror cavity. Rough plate parallelism was obtained by adjusting the plates so that the comet's tail disappeared.

The Galilean telescope was then inserted into the set-up, providing an expanded beam through the interferometer. At this point it was necessary to ensure that the beam passed through the centre of the lenses comprising the Galilean telescope, for all lens positions. With the telescope providing a converging beam, the alignment was adjusted so that the familiar fringe pattern was obtained. Whilst the moveable lens was being adjusted to provide an increasingly parallel beam, the image was observed. The optical alignment of the beam through the Galilean telescope was then adjusted until the centre of the fringe system remained in a fixed position as the beam entering the interferometer was made to vary from converging to diverging. When this was observed to be the case, we were sure that the necessary alignment of the telescope had been achieved.

Now for a fully expanded parallel beam travelling normally through the interferometer, deviation from plate-parallelism is indicated by the appearance of equal inclination (or Haidinger) fringes [55]. The following method was devised to overcome the physical difficulties that were experienced in applying the standard method of achieving plate parallelism [55, 59].

A near-parallel beam was made to pass through the interferometer. By appropriately adjusting the interferometer, the equal inclination fringes

(symptomatic of non-parallelism of the plates) were made to disappear, leaving a uniform illumination exiting the cavity. The telescope was adjusted so that the beam entering the interferometer ranged from converging to diverging. When this operation is performed (starting with a converging beam), the fringe pattern should slowly expand without distortion, with its centre remaining fixed. The plates should be uniformly illuminated for a parallel beam. As the beam becomes diverging, the area of uniform illumination should shrink (remaining centred and undistorted), accompanied by the successive appearance of the bright rings of the fringe pattern. The observation of this scenario indicated that parallelism of the Fabry-Perot plates over the whole aperture had been achieved.

Image formation on the detector

The above adjustments were carried out with the light-proof box in position. This prevented any slight disturbance of the interferometer upon positioning the box. The camera lens was positioned as close to the exit window of the interferometer as the light-proof box would allow. The focused image was observed and the $f = 6mm$ lens position roughly its focal length away from this image. As mentioned earlier, this lens was mounted on a micro-travel plate for adjustment along the optical axis while as well as having vertical control to ensure that the lens was centred on the optical axis. The resulting image was focused by eye on the detector. The box was then sealed up and the fringe pattern was recorded at incremented positions of this lens (f_e). The lens was then fixed at the position which resulted in the best recording. The alignment of the fringe system on the detector was crucial. Adjustments to the height of the lens ensured that the horizontal diameter was recorded.

Additional adjustments to the moveable lens (f_e) about the vertical axis were necessary to ensure that the focal plane and the detector plane coincided. This was the most difficult part of the set-up to realise as we had no fine control over this adjustment.

Linewidth Calculations

The set-up to record the fringe pattern resulting from the backwards Stokes output is illustrated in fig. 3.1, where the fringe recording apparatus is depicted in fig. 3.11. Before we can proceed with the results of the investigation, we must first discuss the details of the calculation of the linewidth from a profile.

The linewidth of the single longitudinal mode Nd:YAG laser used as the pump for SRS is known to be very small:

$$\Delta\kappa < 0.001\ cm^{-1} \tag{3.42}$$

from coherence length measurements [60]. Thus we have that $\Gamma_l < 10\Gamma$, so that we may be approaching the limit of the applicability of the theory on input bandwidths (see page 53). From eqn. 3.21 and eqn. 3.17, the theoretical minimum resolvable wavelength of a given Fabry-Perot interferometer is:

$$\Delta\kappa_{min} = \frac{1}{2\mu t N_R} \tag{3.43}$$

The interferometer used here is quoted to have a reflectivity of $R = 0.85$ and hence a reflectivity finesse of $N_R \simeq 20$. As mentioned in section 3.2.2 on page 101 and section 3.2.3 on page 110 this holds for perfectly flat plates. When the plate flatness of $\lambda/20$ is taken into account, a modified instument

finesse can be obtained. This is quoted by the manufacturers as $N_1 = 10$. Thus for $\mu = 1$ (air filled cavity), the minimum resolvable wavelength separation is achieved for largest possible plate separation t. For this instrument $t_{max} \simeq 10cm$. Hence

$$\Delta\kappa_{min} \simeq 0.005cm^{-1} \tag{3.44}$$

for the interferometer used here. Note that for this plate separation

$$\Delta\kappa_{fsr} \simeq 0.05cm^{-1} \tag{3.45}$$

The method outlined in section 3.2.3 can now be used to calculate linewidth from the recorded fringe profile. Initially an Airy function was fitted to the recorded fringe system. The reason for this was that the method to be used for the linewidth calculations requires knowledge of the *free spectral range* of the instrument. This in turn is dependent on the plate separation t which we were unable to determine accurately enough by direct measurement. However, by treating the parameter $\frac{\phi_c}{2}$ in eqn. 3.37 as a variable enabled the plate separation to be determined from the fitted value of this parameter. The parameter R_f was also allowed to vary, because of the difficulty involved in accurately determining its value (see Appendix D). These two parameters are the most important parameters for fitting the curve to the recorded profile. The other four parameters were estimated from the individual recordings and kept as constants. A range for the two variable parameters was estimated based on rough measurements.

The plate separation t was measured with a vernier caliper to be:

$$t = 10.50cm$$

The background and scaled height parameters b_g and I_s respectively, were estimated from a plot of the recorded profile. These obviously varied for

each profile being fitted. We also estimated the position of the centre of the profile from a recording in which it was included. Using the quoted reflectivity of the plates, $R = 0.85$, the *coefficient of finesse* was obtained as $F = 151$. However, we used the manufacturers quoted value of $N_1 = 10$ to calculate $F = 41$, using eqn. 3.14, for this coefficient and hence took plate imperfections into account. We also implemented a series representation of the Airy function with two further variables which allowed for broadening by Gaussian and Lorentzian functions (see Appendix E).

A function minimisation procedure (based on χ^2 calculations) called MINUIT [61] was used to fit the theoretical curve eqn. 3.37 to the recorded fringe system.

From the parameter $\frac{\phi_c}{2}$, the plate separation was found to be (see eqn. 3.23):

$$t = 10.574cm \tag{3.46}$$

This in turn yields the free spectral range (eqn. 3.17) for this case:

$$\Delta\kappa_{fsr} = 0.0473cm^{-1} \tag{3.47}$$

The method for determining the linewidth as outlined in section 3.2.3 on page 105 can now be applied.

The linewidth of the $Nd:YAG$ pump laser was found to be

$$\Delta\kappa = 0.0109 \pm 0.0009\, cm^{-1}$$

This is seen to be much larger than the theoretical minimum resolvable wavelength separation given by $\Delta\kappa_{min} = 0.0047cm^{-1}$. This difference can be attributed to the previously mentioned sources i.e. incorrect focus or misalignment of the image forming lens system, poorly adjusted interferometer

or inaccurate centering of the linear array detector along the horizontal diagonal of the fringe system. Also in the discussion relating to fig. 3.10 it was shown that the method applied, results in an overestimate of the linewidth. It should be noted that the method of fitting a series representation of the Airy function, including the freedom of broadening due to the finite spectral width of the radiation (as outlined in Appendix E) is limited by the fact that the recorded peaks are in general not of uniform intensity (see figs. 3.14 and 3.15) and also because the further broadening due to possible misalignment cannot be disentangled. Naturally, if none of the above-mentioned problems occurred, we would expect that the measured linewidth would be at the calculated limit. We therefore confine our linewidth evaluations to the method of section 3.2.3. The fitting procedure will only be used to obtain a more accurate estimate of the plate separation as well as for illustrative purposes.

Results of the Investigation

Each recording consisted of the capture of 30 profiles, each of which consisted of the first $5-7$ fringes, by the O.M.A. Not all of the thirty profiles of each recording were equally good. There was in fact a great deal of variability from shot to shot. For the purposes of measurement, it was decided that only the best profiles of each recording would be analysed. The significance of this will now be discussed.

Included in each recording were a variety of different profiles. These ranged from profiles which had far broader fringes than the 'good' profiles and were generally more 'messy', to profiles which exhibited distinctly multimode type features (i.e. two superimposed fringe systems). Examples of

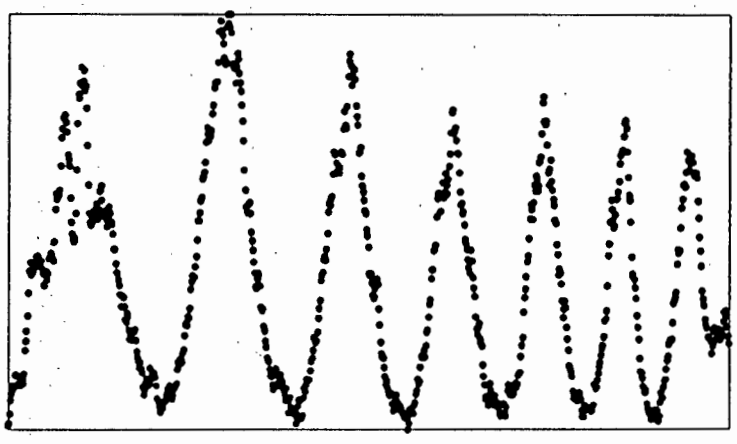

Pixel positions

Figure 3.12: contains a reproduction of 'broad messy' profile.

these types of profiles are reproduced in figure 3.12 and figure 3.13 respectively.

These 'multimode' shots are, by and large, not associated with spurious multimode firings of the laser. It is supposed that they are in fact an inherent feature of transient SRS in which more than one Stokes mode can experience appreciable gain. This would also qualitatively explain the numerous 'broad – multimode' profiles since the various Stokes modes would experience different relative gains from shot to shot (see figure 3.13). As mentioned in the previous section on page 95, a further possible explanation could be due to the nanosecond temporal structure of the output (see fig. 3.2 (i), (j) and (k)), with its concommitant frequency broadening. This phenomenon will therefore have to be investigated more carefully.

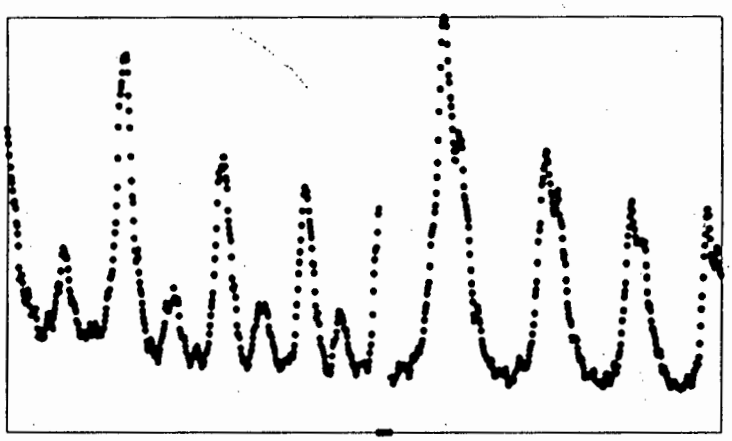

Pixel positions

Figure 3.13: contains reproductions of two 'multimode' type profiles. The profile on the left exhibits well resolved fringes, while in the profile on the right the overlapping fringe systems are just resolved.

In each recording, the profiles were therefore classified as 'good' or 'messy – multimode'. The best profiles of the 'good' shots were then used to obtain the linewidth of that recording. Generally, the calculated linewidths of the 'good' shots varied by $10 - 15\%$. An example of a 'good' profile appears in fig. 3.14. The ratio of the 'good' profiles to the total number of profiles in each recording showed no clear dependence on either the pump energy or the hydrogen pressure. The ratio which varied from $0 - 80\%$ of the profiles being classified as 'good' showed no correlation with the conditions.

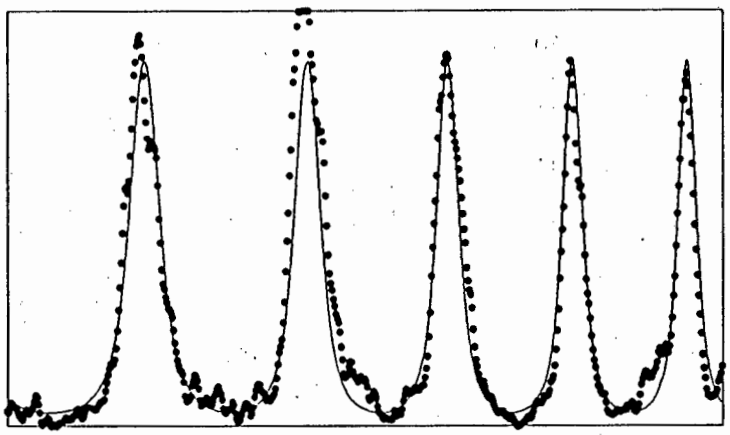

Figure 3.14: contains a portion of a 'good' profile, from which linewidth measurements were obtained, together with a fitted Airy function.

We did not attempt to measure the separation of the modes in the multimode profiles for two reasons. The first reason being that it was not clear that the two fringe patterns were of the same order. Secondly, as is evident from the two reproductions in figure 3.13 the separation of the modes was quite variable. It should therefore be borne in mind that the linewidth results presented here represent the best case scenario.

A further odd observation was that of the rapid decrease of the fringe intensity towards the outside of the fringe (i.e. away from the centre) in some shots. We were unsure what caused this phenomenon, which is well illustrated in figure 3.15, as there was no correlation with the pump energy or hydrogen pressure. We were able to obtain three to five measures of the

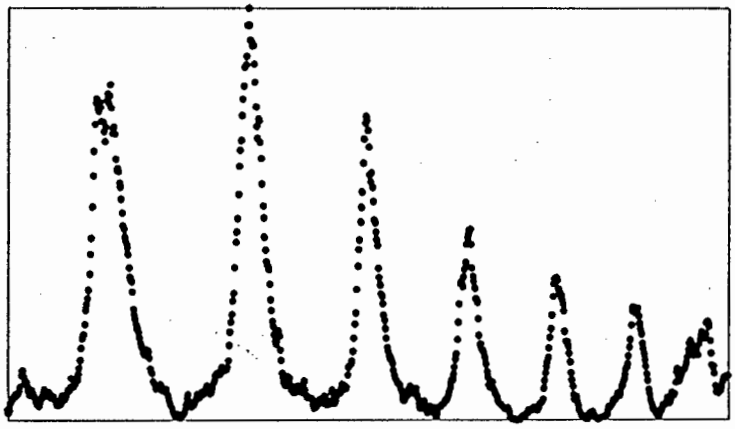

Pixel positions

Figure 3.15: contains a reproduction of a profile which exhibits a rapid decrease in the fringe profile towards to outside of the profile

linewidth from each profile, depending on the relative intensity of the fringes across the profile, by the method outlined in section 3.2.3.

After recording the profile of the pump laser, we commenced with the investigation into the linewidth of the backscattered Stokes output. We first looked at the effect of varying the pump energy at fixed pressures as well as the effect of varying the pressure.

The results at fixed pressures of 41 and 21 atm, plotted in fig. 3.16, show no clear dependence of the linewidth on laser energy within the 10% uncertainty of the results.

Although we have been unable to fit our relevant theoretical equations to any of our results, we can still make a qualitative comparison of the results

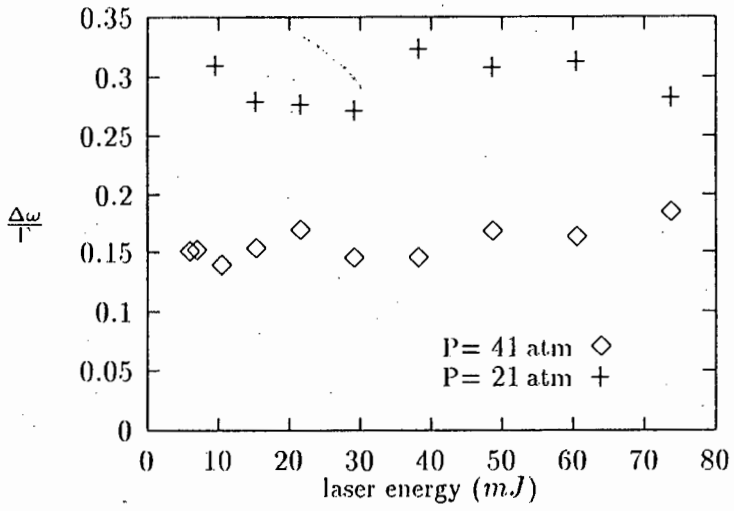

Figure 3.16: contains a plot of the results of the investigation into the effects on the backward Stokes linewidth of the pump energy. The results were obtained at fixed pressures of 41 atm and 21 atm.

of fig. 3.16 with fig. 2.4. For an intensity ratio of the order of that in our case, the bottom portion of the linewidth curve (b) in fig. 2.4 extends much further along the gain axis. Thus for the appropriate gain it seems plausible that there would be no dependence on the pump energy.

Assuming that the pump had no effect on the best linewidth, we proceeded to investigate the effect of pressure on the linewidth. We recorded profiles at various pressures for three distinct pump energy regions, namely: (1) threshold, (2) depletion and (3) saturation. These three pump regions are defined in terms of the temporal intensity trace of the transmitted pump. They are illustrated in some of the traces of figure 3.2. The threshold region (1), is characterised by very small distortions to the peak of the transmitted pump as illustrated in traces (a) and (b). The depletion region (2) is characterised by a marked dip in the profile of the transmitted pump as illustrated in traces (e) and (i). Finally, the saturation region (3) is characterised by a flattened transmitted pump profile as illustrated in trace (g). It should be stressed that the labels: threshold, depletion and saturation, do not hold their usual meaning from SRS gain considerations.

In figure 3.17 the results of this investigation are plotted. A definite relationship between the linewidth of the backward Stokes output and the hydrogen pressure is seen to exist. Again we can compare these results with the trend illustrated in fig. 2.5, so that for a much larger input intensity ratio, we might expect the dip region to extend well into our pressure range. The fact that our measured linewidth is broadened at lower pressures is, however, unaccounted for in this comparison.

We now present our concluding chapter in which the significance of our results is discussed.

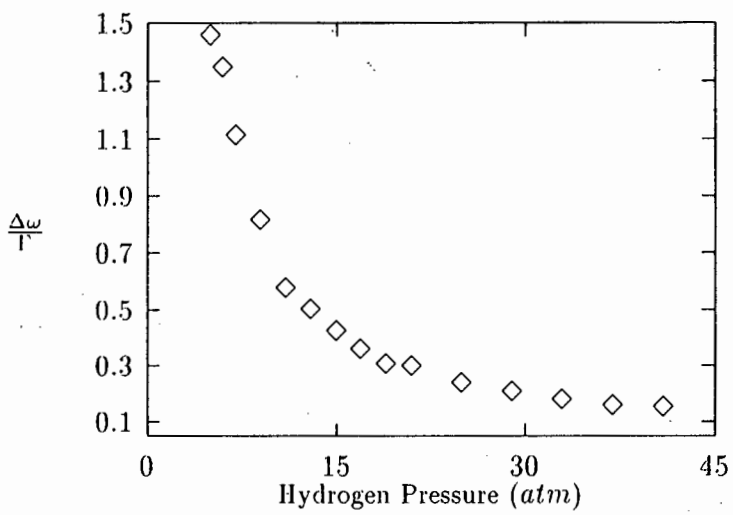

Figure 3.17: is a plot of the linewidth in units of the Raman linewidth as a function of pressure.

Chapter 4

Discussion and Conclusion

Unfortunately it seems that the regime to which we were experimentally restricted, does not correspond with the area covered by the presented theory. We are therefore not able to quantitatively explain the origins of 'predominantly' backward SRS in our observations. On the positive side, this indicates that a more comprehensive model is required to describe the complicated interaction involved. This is only possible by making use of computer simulations.

Two different possibilities explaining the suppressed forward SRS gain have been proposed [21, 27, 41]. Trainor et al. [21] and Perry et al. [27] proposed that anti-Stokes coupling in the forward direction was the cause of the suppressed forward Stokes emission. In a computer simulation in which this anti-Stokes coupling was included, Zaporozhchenko et al. [41] found that this had a negligible effect. They essentially concluded that the observed enhancement of the backward Stokes emission was as a result of the complexities introduced by focused propagation through the medium. Although the importance of focusing can not be overstated, it seems that the mere presence of the correct focusing conditions alone are unable to

account for this effect. It is unclear from the presentation of Zaporozhchenko et al. how they incorporated the maximising of the gain with respect to the momentum mismatch. This places doubt on the method in which the anti-Stokes radiation was taken into account.

Our experimental results seem to illustrate the importance of the anti-Stokes coupling in the forward direction. This explanation is, however, not without its faults, specifically the very interesting observation of anti-Stokes radiation in the backward direction. The nature of the process giving rise to this anti-Stokes emission is unclear and warrants further investigation.

The way in which focusing has, thus far, been taken into account in the computer simulations, is approximate. A more complete treatment is the decomposition of the fields into coupled Gauss-Laguerre mode equations [29]. This treatment has already provided interesting predictions (some of which have been experimentally verified [27]) in the case of forward SRS. The applicability of this method to backward SRS should be investigated.

Once a better model of the interaction region has been formulated, a more relevant comparison with our experimental work would become possible. In particular, the effects of focusing and the observed temporal structure could be clarified. Because of the limitations of our equipment, the experimental work itself would also have to be repeated.

An investigation into the effects of focusing will require a high pressure cell of variable length. The temporal investigation of the output will require a much 'faster' oscilloscope. The energy conversion experiments require more sensitive equipment so that the whole SRS gain curve can be investigated. This should be accompanied by a more careful analysis of possible higher order Raman emission.

In order to investigate the predictions of our model of the Stokes linewidth in the presence of a depleted pump, we would have to ensure that we were operating in the steady state. More sensitive spectral analysis equipment would also be desirable. The variability of the measured linewidths for the 'same' conditions needs to be clarified by investigating the output linewidths in both the steady state and transient regimes. The role of the observed temporal structure of the SRS output in this regard may then also become clear.

Although it is evident from this discussion that the dynamics of the SRS process under focused conditions is as yet unclear, it can be concluded that a much better understanding of the process has been obtained. The fact that the laser only became available towards the end of the research period, made it very difficult to perform an exhaustive comparison of the results with the theory. It is therefore entirely possible that important correlations may have been missed.

Finally the use of stimulated Raman scattering as a means of providing a pump beam for CARS work, by frequency shifting the output of the $Nd:YAG$ laser, can be discussed. The results of the energy conversion measurements are positive in this regard. However, the fact that the linewidth of the Stokes emission is subject to extreme variability, is cause for concern. It seems likely that if the process can be confined to steady state operation, then the resulting Stokes emission in the backward direction would constitute a suitable pump for CARS work.

Appendix A

The Slowly Varying Amplitude Approximation

We begin by considering only spatial propagation and we therefore assume that there is no time dependence. We further simplify matters by assuming plane waves propagating in the z-direction. Hence the field may be written as:

$$\vec{E}_\omega(z) = \hat{e}E(z)e^{i(kz-\omega t)} \tag{A.1}$$

More generally, the field may be split into components parallel and perpendicular to the propagation vector $\vec{k}$. This enables the wave equation to be split into two equations, one for each component.

$$\nabla^2\vec{E}_\perp + \frac{\omega^2}{c^2}(\underline{\epsilon}.\vec{E})_\perp = -\frac{4\pi\omega^2}{c^2}\vec{P}_\perp^{NL}$$

$$\vec{\nabla}.[(\underline{\epsilon}.\vec{E})_{||} + 4\pi\vec{P}_{||}^{NL}] = 0 \tag{A.2}$$

Where the vector identity

$$\vec{\nabla}\times(\vec{\nabla}\times\vec{a}) = \vec{\nabla}(\vec{\nabla}.\vec{a}) - \nabla^2\vec{a}$$

with $\vec{\nabla}.(\vec{\nabla} \times \vec{b}) = 0$, has been used. Now since we have confined our considerations to plane waves propagating in the z - direction, only the first of the above equations remains to be satisfied. In this case we have that:

$$\nabla^2 \vec{E}_\perp = \frac{\partial^2}{\partial z^2} \vec{E}_\omega(z) = \hat{e}\, e^{i(kz-\omega t)} \left[\frac{\partial^2}{\partial z^2} + 2i\, k \frac{\partial}{\partial z} - k^2 \right] E(z) \qquad \text{(A.3)}$$

It should be noted that we have neglected the tensorial nature of $\underline{\epsilon}$, (resulting in $\frac{\omega^2}{c^2}(\underline{\epsilon}.\vec{E})_\perp = k^2$), which is consistent with isotropy or propagation along a symmetry axis of the medium. We expect the relative amplitude change over a wavelength to be small since the nonlinear susceptibility is much smaller than its linear counterpart. Hence we assume

$$|\frac{\partial^2 E(z)}{\partial z^2}| \ll |k \frac{\partial E(z)}{\partial z}| \qquad \text{(A.4)}$$

which is the slowly varying amplitude approximation. This results in spatial propagation being described by:

$$\frac{\partial}{\partial z} E(z) = i \left(\frac{2\pi\omega^2}{k\, c^2} \right) P^{NL}(z) \qquad \text{(A.5)}$$

Where $\vec{P}^{NL}(z) = \hat{e}\, P^{NL}(z) e^{i(kz-\omega t)}$.

It should be noted that for backward travelling waves the relevant equation becomes:

$$\frac{\partial}{\partial z} E_b(z) = -i \left(\frac{2\pi\omega^2}{k\, c^2} \right) P^{NL}(z) \qquad \text{(A.6)}$$

which is obtained from the general wave equation simply by changing the propagation vector to $-\vec{k}$.

In general the field amplitudes will not be independent of time. We may treat temporal propagation in an analogous fashion. The equation describing

temporal propagation after the slowly varying amplitude approximation has been invoked is [2]:

$$\frac{1}{v}\frac{\partial}{\partial t}E(t) = i\left(\frac{2\pi\omega^2}{k\,c^2}\right)P^{NL}(t) \qquad \text{(A.7)}$$

Appendix B

Gaussian Beam Propagation

A full treatment of this topic is given in many texts on lasers and nonlinear optics [62, 63].

We assume azimuthally symmetric fields propagating in the z-direction in a homogeneous medium.

$$\vec{E}(x,y,z,t) = Re[\vec{E}(r,z)e^{i(\omega t - kz)}] \tag{B.1}$$

In the slowly varying amplitude approximation, the solution for a single field component is found to be:

$$E(r,z) = E_0 \frac{w_0}{w(z)} e^{-i[kz-\theta(z)]-r^2[1/w^2(z)+ik/2R(z)]} \tag{B.2}$$

where the parameters are:

$$w^2(z) = w_0^2[1+(z/z_0)^2] \qquad R(z) = z[1+(z_0/z)^2]$$
$$\theta(z) = tan^{-1}(z/z_0) \qquad z_0 = \frac{\pi\omega_0^2}{\lambda} \tag{B.3}$$

The coefficient of r^0 describes the phase variation compared to the plane wave solution. The coefficient of r^2 can be written as $ik/2q(z)$ where $k = 2\pi/\lambda$ and hence

$$\frac{1}{q(z)} = \frac{1}{R(z)} - \frac{i\lambda}{\pi w^2(z)} \tag{B.4}$$

which is the fundamental Gaussian beam solution in terms of which the propagating beam can be desribed. The first term, $R(z)$, can be identified with the spherical wavefront radius and it evolves according to the the appropriate relation in eqn. B.3. Notice that since the second term in equation B.4 is the only one in the solution, eqn. B.2, which is not complex, the intensity profile can be written as:

$$I(r) = I(0)e^{-\frac{2r^2}{w^2}} \tag{B.5}$$

Thus it is evident that w can be used to define the beam spot size, since at $r = w$, the beam intensity has fallen to $1/e^2$ of its on axis value. The beam can therefore be considered to be contained within this area. The spot size radius $w(z)$, evolves according to the appropriate relation in eqn. B.3. From this it is seen that $w(z = 0) = w_0$ is the minimum spot size of the beam. It is known as the beam waist and is located at the in the focal plane of the beam.

The quantity z_0 is known as the Rayleigh range and is a measure of the extent of the waist region i.e. $w(z = z_0) = \sqrt{2}\, w_0$ so that the beam area at $z = z_0$ is twice that at the beam focus. The quantity $2z_0$ is commonly refered to as the confocal parameter of the beam.

In the far field it is easily shown that the beam is asymptotic to the cone of half apex angle

$$\alpha = tan^{-1}\left(\frac{\lambda}{\pi w_0}\right) \simeq \frac{\lambda}{\pi w_0} \tag{B.6}$$

which defines the beam divergence and illustrates the phenomenon of beam diffraction. We now discuss the propagation of a Gaussian beam through optical elements.

For a beam propagating through a system described by the geometrical matrix element

$$\begin{bmatrix} A & B \\ C & D \end{bmatrix}$$

it can be shown that the complex beam parameter is transformed according to

$$q_2 = \frac{Aq_1 + B}{Cq_1 + D} \tag{B.7}$$

Thus the focusing of a Gaussian beam can now be treated. A beam entering a lens of focal length f, at its waist w_0, will be focused down to a beam of waist w_0'. The spot size of the focused beam is described along the propagation direction by:

$$w'^2(z) = w_0^2[(1 - z/f)^2 + (z/z_0)^2] \tag{B.8}$$

Thus the cross-sectional area of the focused beam is given by:

$$A(z) = \pi w'^2(z) \tag{B.9}$$

The new beam waist, located at $z = l$, is given by:

$$w'^2(l) = w_0'^2 = \left(\frac{\lambda f}{\pi w_0}\right)^2 \frac{1}{1 + (f/z_0)^2} \tag{B.10}$$

which defines the Rayleigh range of the focused beam according to eqn B.3. Thus the Rayleigh range or the confocal parameter can be seen as a measure of the the focusing conditions of the beam (i.e. tighter focus $\Rightarrow$ smaller waist $\Rightarrow$ smaller confocal parameter $\Rightarrow$ quicker cross-sectional growth).

More generally for a beam of divergence α and spot size w, incident on a lens of focal length f, the new waist radius can be shown to be [63]:

$$w_0' = \frac{\lambda}{\pi}\left[\alpha^2 + (w/f)^2 - \frac{2\lambda}{f}\sqrt{\frac{\pi w \alpha}{\lambda} - 1}\right]^{-\frac{1}{2}} \tag{B.11}$$

which reduces to the previous case when $w = w_0$. If, however, the new beam radius need not be known in terms of the the original beam's parameters, then we can simply use the relevant equation for $w^2(z)$ in eqn. B.3 with the appropriate focused beam parameters.

$$w^2(z) = w_{0f}^2 \left(1 + \frac{(z-l)^2}{z_r^2}\right) \tag{B.12}$$

where w_{0f} is the beam radius at the waist which is located at $z = l$ and z_r is the Rayleigh range of the focused beam i.e. $z_r = \frac{\pi w_{0f}^2}{\lambda}$. Thus this relation, eqn. B.12, cannot describe continued propagation of the beam beyond the lens.

Focusing can thus be taken into account in our simple 1-dimensional model by dividing the power in each signal by the beam cross-sectional area, eqn. B.9, using either eqn. B.8 or eqn. B.12.

Appendix C

Approximate Spectral Line Separation

The purpose of this appendix is to justify the approximation leading to eqn. 3.36. References are made to fig. 3.9 which schematically represents the situation. In equation 3.19 it was shown that if we could find $|\frac{\delta\phi}{2\pi}|$ then the wavelength separation of the two lines could be found. In equation 3.22 this was shown to be equal to δn, the difference of order of interference, which was shown to be given by eqn. 3.35:

$$\delta n = \frac{\delta_{ba}}{\Delta}$$

where eqns. 3.34 & 3.27, 3.30 define δ_{ba} and Δ respectively.

Now writing

$$\Delta = \frac{1}{2}(\Delta_a + \Delta_b)$$

yields the following for the difference in the order of interference:

$$\delta n = \frac{2({}_bD_i^2 - {}_a D_i^2)}{({}_bD_i^2 - {}_b D_{i-1}^2) + ({}_aD_{i+1}^2 - {}_a D_i^2)}$$

$$= \frac{2\sigma_{ab}({}_aD_i + {}_b D_i)}{[{}_b\omega({}_bD_i + {}_b D_{i-1}) + {}_a \omega({}_aD_i + {}_a D_{i+1})]}$$

where $\sigma_{ab} = ({}_bD_i - {}_aD_i)$ and $\omega = (D_i - D_{i-1})$ as indicated in the figure. We now write:

$${}_aD_{i+1} = {}_bD_i + ({}_aD_{i+1} - {}_bD_i)$$

$${}_bD_{i-1} = {}_aD_i + ({}_bD_{i-1} - {}_aD_i)$$

so that the difference in the order of interference becomes upon substitution:

$$\delta n = \frac{2\sigma_{ab}({}_aD_i + {}_bD_i)}{[({}_a\omega + {}_b\omega)({}_aD_i + {}_bD_i) + {}_a\omega({}_aD_{i+1} - {}_bD_i) + {}_b\omega({}_bD_{i-1} - {}_aD_i)]}$$

Now the third term of the denominator can be rewritten as:

$${}_b\omega({}_bD_{i-1} - {}_aD_i) = -{}_b\omega({}_aD_i - {}_bD_{i-1})$$

$$\simeq -{}_b\omega({}_aD_{i+1} - {}_bD_i) = -\Delta D_b\omega$$

Hence the last two terms in the denominator can be combined to yield:

$$\delta n = \frac{2\sigma_{ab}({}_aD_i + {}_bD_i)}{[({}_a\omega + {}_b\omega)({}_aD_i + {}_bD_i) + ({}_a\omega - {}_b\omega)\Delta D]}$$

Now for rings far from the centre we have:

$$\Delta D \ll ({}_aD_i + {}_bD_i)$$

and hence

$$({}_a\omega + {}_b\omega)({}_aD_i + {}_bD_i) \gg ({}_a\omega - {}_b\omega)(\Delta D)$$

so that dividing by $({}_a\omega + {}_b\omega)({}_aD_i + {}_bD_i)$ enables the binomial theorem to be applied, thus obtaining for the difference in order of interference:

$$\delta n = \frac{2\sigma_{ab}}{({}_a\omega + {}_b\omega)}\left[1 - \frac{{}_b\omega({}_bD_{i-1} - {}_aD_i) + {}_a\omega({}_aD_{i+1} - {}_bD_i)}{({}_a\omega + {}_b\omega)({}_aD_i + {}_bD_i)} + \cdots\right]$$

Then taking only the first term leads to the approximation of eqn. 3.36.

Appendix D

Calculation of the Fitting Parameter R_f

This appendix is concerned with the calculation of the parameter R_f used in the fitting of an Airy function to a recorded pattern. The discussion is referred to the general set-up illustrated in fig. D.1. This parameter contains information about the optical set-up involved in preparing the source (assumed to be a parallel beam) for entry into the interferometer as well as that involved in the formation of the image in the detector plane. A geometrical optics approach will be pursued in these considerations. R_f also depends on the detector dimensions.

Firstly it is necessary to know the radius of the converging/diverging wave exiting the interferometer. To obtain a fringe pattern, the beam entering the interferometer must be either converging or diverging. This is achieved by having the beam expander slightly off the afocal configuration:

$$d = f_1 + f_2 + x$$

Where x is a measure of how far from afocal the configuration is. The case where $x = 0$ is the afocal configuration in which a parallel input beam is

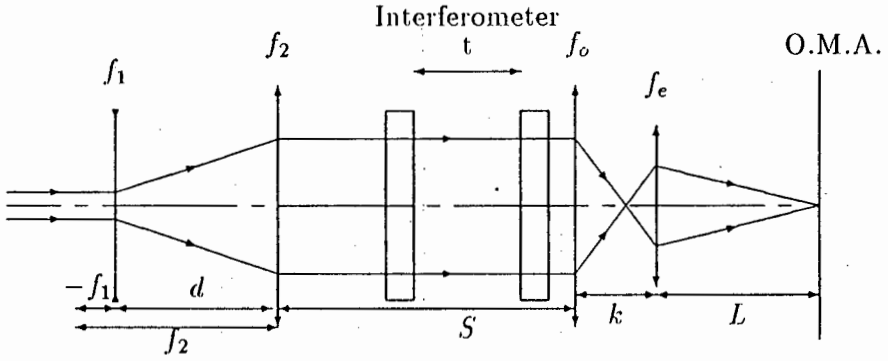

Figure D.1: Set-up illustrating quantities for calculation of R_f.

expanded but remains parallel at output. For the second lens f_2 we have

$$\frac{1}{u} + \frac{1}{v} = \frac{1}{f_2}$$

which can be rewritten as:

$$\frac{1}{v} = \frac{1}{f_2} - \frac{1}{d - f_1}$$

Here v is the position where the beam exiting the beam expander will be brought to a focus. Hence we can make the identification:

$$R = v$$

where R is the radius of curvature of the beam exiting the beam expander.

$$\frac{1}{R} = \frac{1}{v} = \frac{1}{f_2} - \frac{1}{f_2 + x} = \frac{x}{f_2(f_2 + x)}$$

or

$$R = \left(\frac{f_2^2}{x} + 1\right)$$

Note that if $x < 0$ (i.e. lenses closer than afocal) and $|x|$ is small, then the exiting beam will be converging and vice versa for $x > 0$. Thus the radius of curvature of the wave upon exiting the interferometer is:

$$R' = R + S$$

where S is the distance from the exit of the beam expander to the entrance of the image forming system.

We now procede with the calculation of the size of the image of the fringe system on the detector. The ray matrix approach will be applied. Consider the i^{th} fringe of the transmitted fringe system. Upon exiting the interferometer, this fringe will be described by the vector:

$$\begin{pmatrix} y \\ \theta \end{pmatrix}_i$$

where y_i is the radius and θ_i the angular radius of the i^{th} fringe. At the detector this fringe will be described by:

$$\begin{pmatrix} y_d \\ \theta_d \end{pmatrix}_i$$

The equation relating these two vectors is:

$$\begin{pmatrix} y_d \\ \theta_d \end{pmatrix}_i = \begin{pmatrix} 1 & L \\ 0 & 1 \end{pmatrix} \begin{pmatrix} 1 & 0 \\ -\frac{1}{f_e} & 1 \end{pmatrix} \begin{pmatrix} 1 & k \\ 0 & 1 \end{pmatrix} \begin{pmatrix} 1 & 0 \\ -\frac{1}{f_o} & 1 \end{pmatrix} \begin{pmatrix} y \\ \theta \end{pmatrix}_i$$

$$= \begin{pmatrix} (1-\frac{L}{f_e})(1-\frac{k}{f_o}) - \frac{L}{f_o} & k(1-\frac{L}{f_e}) + L \\ -\frac{1}{f_e}(1-\frac{k}{f_o}) - \frac{1}{f_o} & -\frac{k}{f_e} + 1 \end{pmatrix} \begin{pmatrix} y \\ \theta \end{pmatrix}_i$$

Now notice that the radius of the i^{th} fringe is

$$y_i = R'\theta_i$$

where R' is the radius of the wavefront and θ the angular radius of the fringe. Hence:

$$y_{d_i} = [(1-\frac{L}{f_e})\{(1-\frac{k}{f_o})R' + k\} + L(1-\frac{R'}{f_o})]\theta_i$$

The dependence on the radius of curvature upon entry into the image forming system, R', can best be illustrated by an example.

e.g. Set: $f_e = 6mm$, $f_o = 58mm$, $k = 64mm$ and $L = 372mm$ then,

$$y_{d_i} \simeq [-0.1R' - 3500]\theta_i.$$

Thus it is evident that when R' is of the order of $10^3 mm$, it contributes $\simeq$ 10% to the detected radius. However, as $R' \rightarrow \infty$ (i.e. parallel beam through interferometer), it totally overwhelms the detected radius as expected. In this case only a small cone of rays is present in the beam and hence the transmitted intensity pattern is just that for normal illumination of the plates.

Thus with a definite converging/diverging beam, $|R'| \simeq 10^3 mm$ will be true and the major contribution to the image size is from the image forming system. This may thus be selected to suit the requirements of the recording (e.g. the number of fringes on the detector area etc.).

To obtain the conversion factor R_f enabling the conversion of the measured radius y_{d_i} to the argument θ_i of the cosine, we have

$$\theta_i = y_{d_i}/[(1 - \frac{L}{f_e})\{(1 - \frac{k}{f_o})R' + k\} + L(1 - \frac{R'}{f_o})]$$

Finally, recall from eqn. 3.37 that the radius measured from the recording is a pixel position x and hence must be converted to a radius y_d in meters or mm. This conversion must also be included in the parameter R_f. Note that for a linear array detector of dimensions z m containing 1024 pixels, a length in pixels of x corresponds to an actual length of

$$y_d = x.\frac{z}{1024}\ m$$

Hence $\theta_i = R_f x$ where

$$R_f = \frac{z}{1024}[(1 - \frac{L}{f_e})\{(1 - \frac{k}{f_o})R' + k\} + L(1 - \frac{R'}{f_o})]^{-1}$$

For a radius of curvature $R' \simeq 6000\ mm \Rightarrow y_{d_i} \simeq -4100\theta_i$ and with a detector of length $z = 0.025\,m$, using the above example, we get a conversion factor of: $R_f = 6 \times 10^{-6}$ rad.pixel^{-1}.

Appendix E

Broadening of the Airy Function

In this appendix we illustrate how broadening by Gaussian or Lorentzian functions can be incorporated into the form of the Airy function. We do not go into detail, but only present the major results [55]. The Airy function which describes the output through an ideal Fabry-Perot interferometer (see eqn. 3.7) can be written as a series:

$$I(\psi) = I_0 \left(\frac{T}{1-R}\right)^2 \frac{(1-R)}{(1+R)} \left(1 + 2\sum_{m=1}^{\infty} R^m \cos m\psi\right) \tag{E.1}$$

This representation lends itself to simple convolution with both Gaussian and Lorentzian functions. Thus phenomena, described by these two functions, causing broadening of the ideal output can be taken into account. Phenomena such as plate imperfections and non-monchromatic sources can be treated in this way.

The convolution of eqn. E.1 with a Gaussian function of unit area

$$f(\psi) = \frac{1}{a\sqrt{\pi}} e^{-\frac{\psi^2}{a^2}} \tag{E.2}$$

is

$$I_G(\zeta) = \frac{I'}{a\sqrt{\pi}} \left(1 + 2 \sum_{m=1}^{\infty} R^m e^{-a^2\pi^2 m^2} \cos 2\pi m\zeta \right) \tag{E.3}$$

where

$$I' = I_0 \left(\frac{T}{1-R} \right)^2 \frac{(1-R)}{(1+R)}$$

This illustrates that the convolution simply results in the multiplication of each term by the Gaussian function $\frac{1}{a\sqrt{\pi}} e^{-a^2\pi^2 m^2}$. Convolution with a normalised Lorentzian function

$$g(\psi) = \frac{\delta_L}{2\pi} / [(\delta_L/2)^2 + \psi^2] \tag{E.4}$$

is

$$I_L(\zeta) = \frac{\delta_L I'}{2\pi} \left(1 + 2 \sum_{m=1}^{\infty} (R e^{-\delta_L \pi})^m \cos 2\pi m\zeta \right) \tag{E.5}$$

This illustrates that convolution with a Lorentzian broadening function is equivalent to a reduction in the reflectivity. It should be noted that δ_L is the halfwidth of the Lorentzian function in units of the free spectral range i.e. $\delta_L = 2\mu t \nu_L$ with ν_L in cm^{-1}.

The associative and commutative property of the convolution process enables the profile to be written down in the presence of both broadening functions as:

$$I_{GL}(\zeta) = \frac{\delta_L I'}{2\pi\sqrt{\pi}a} \left(1 + 2 \sum_{m=1}^{\infty} (R e^{-\delta_L \pi})^m e^{-a^2\pi^2 m^2} \cos 2\pi m\zeta \right) \tag{E.6}$$

Thus a fitting routine which has two more variables, accounting for the broadening phenomena described by these two functions, may be applied with as many terms of the series as the quality of the experimental data requires.

Acknowledgements

I would like to acknowledge the assistance of a few people without whom this thesis would not have taken the present form. I would like to thank my two supervisors. Firstly, Professor G.N. Robertson for proposing the topic and for assisting with my conceptual understanding. Secondly, Dr H.S.T. Driver for his invaluable presence in the laboratory as well as for his time spent reading and re-reading this work as it slowly progressed.

I am very appreciative of the work done for me by our workshop, especially the construction of the light-proof box used in the linewidth experiments but also for all those little rush-jobs towards the end. I would also like to thank Dr R.J. Hutcheon for his assistance with my experiments.

I am grateful to Jasper Horrell, my office mate for the past two years, for some helpful and some not-so-helpful discussions. I would like to thank Johnathan Knight for his useful insight when my mind was blank.

I am indebted to the FRD for providing me with funding for the past two years, as well as my bursary company, De Beers Industrial Diamond Division, for allowing me to continue with my studies.

Finally, I would like to thank all those who I have failed to mention, but who contributed in some way to getting me through an interesting two years.

Bibliography

[1] W.K. Bischel in a private communication with G.N. Robertson

[2] Y.R. Shen, *The Principles of Nonlinear Optics*, John Wiley and Sons (1984), Ch. 1-3

[3] J.A. Armstrong, N. Bloembergen, J. Ducuing and P.S. Pershan, *Phys. Rev.*, **127**, (1962), p1918

[4] A. Yariv, *IEEE J. of Quant. Elec.*, **QE-13**, (1977), p943

[5] T.K. Yee and T.K. Gustafson, *Phys. Rev.*, **A18**, (1978), p1597

[6] Y. Prior, *IEEE J. of Quant. Elec.*, **QE-20**, (1984), p37

[7] D.C. Hanna, M.A. Yuratich, D. Cotter, *Nonlinear Optics of Free Atoms and Molecules*, (Springer Series in Optical Sciences **Vol 17**), Springer-Verlag (1979)

[8] A. Yariv *Quantum Electronics 3rd ed.*, John Wiley and Sons (1989), Ch. 16

[9] A. Yariv *Quantum Electronics 3rd ed.*, John Wiley and Sons (1989), Ch. 18

[10] Y.R. Shen and N. Bloembergen, *Phys. Rev.* **137**, (1965), p1787

[11] C.S. Wang, *Phys. Rev.* **182**, (1969), p482

[12] M. Maier,W. Kaiser,J.A. Giordemaine, *Phys. Rev.* **177**, (1969), p580

[13] P. Lallemand, G. Bret and P. Simova, *Phys. Rev. Lett.* **17**, (1966), p1239

[14] J.R. Murray and A. Javan, *J. of Mol. Spectr.* **42**, (1972), p1

[15] W.K. Bischel and M.J. Dyer, *Phys. Rev.* **A33**, (1986), p3113

[16] M.G. Raymer, J. Mostowski and J.L. Carlsten, *Phys. Rev.* **A19**, (1979), p2304

[17] M.G. Raymer and J. Mostowski, *Phys. Rev.* **A24**, (1981), p1981

[18] Y.R. Shen, *The Principles of Nonlinear Optics*, John Wiley and Sons (1984), Ch. 10

[19] N. Tan-no, T. Shirahata, K. Yokoto and H. Inaba, *Phys. Rev.* **A12**, (1975), p159

[20] R.V. Johnson and J.H. Marburger, *Phys.Rev.* **A4**, (1971), p1175

[21] D.W. Trainor, H.A. Hyman and R.M. Heinrichs, *IEEE J. of Quant. Elec.* **QE-18**, (1982), p1929

[22] W.H. Lowdermilk and G.J. Kachen, *J. of Appl. Phys.* **50**, (1979), p3871

[23] J.L. Carlsten, J.M. Telle and R.G. Wenzel, *Opt. Lett.* **9**, (1984), p353

[24] J.L. Carlsten, J. Rifkin and D.C. MacPherson, *JOSAB* **B3**, (1986), p1476

[25] D. von der Linde, M. Maier and W. Kaiser, *Phys. Rev.* **178**, (1969), p11

[26] S.R.J. Brueck and H. Kildal, *IEEE J. of Quant. Elec.* **QE-18**, (1982), p310

[27] B.N. Perry, P. Rabinowitz and D. Bomse, *Opt. Lett.* **10**, (1985), p146

[28] B.N. Perry, P. Rabinowitz and M. Newstein, *Phys. Rev. Lett.* **49**, (1982), p1921

[29] B.N. Perry, P. Rabinowitz and M. Newstein, *Phys. Rev.* **A27**, (1983), p1989

[30] A. Gavrielides and P. Peterson, *JOSAB*, **B3**, (1986), p1394

[31] Z.H. Zhang, H.A. Zhang and Q. Liu, *Opt.Comm.* **88**, (1992), p73

[32] W.K. Bischel and M.J. Dyer, *JOSAB*, **B3**, (1986), p677

[33] W.R. Trutna, Y.K. Park and R.L. Byer, *IEEE J. of Quant. Elec.* **QE-15**, (1979), p648

[34] R.L. Carman, F. Shimizu, C.S. Wang, N. Bloembergen, *Phys. Rev.* **A2**, (1970), p60

[35] S.A. Akhmanov, Yu.E. D'yakov and L.I. Pavlov, *Sov. Phys. JETP*, **39**, (1974), p249

[36] J. Egglestone and R.L. Byer, *IEEE J. of Quant. Elec.* **QE-16**, (1980), p850

[37] G.G. Lombardi and H. Injeyan, *JOSAB* **B3**, (1986), p1461

[38] M. Trippenbach, K. Rzazewski and M.G. Raymer, *JOSAB*, **B1**, (1984), p671

[39] M.G. Raymer and L.A. Westling, *JOSAB*, **B2**, (1985), p1417

[40] N. Bloembergen and Y.R. Shen, *Phys.Rev. Lett* **12**, (1964), p504

[41] R.G. Zaporozhchenko, I.S. Zakharova and G.G. Kotaev, *J. of Mod. Opt.* **39**, (1992), p863

[42] W.H. Culver, J.A. Vanderslice and V.W.T. Townsend, *Appl. Phys. Lett.*, **12**, (1968), p189

[43] Y.R. Shen and Y.J. Shaham, *Phys. Rev.* **163**, (1967), p162

[44] A.P. Hickman, J.A. Paisner and W.K. Bischel, *Phys. Rev.* **A33**, (1986), p1788

[45] E.E. Hagenlocker, R.W. Minck and W.G. Rado, *Phys. Rev.* **154**, (1967), p226

[46] G.I. Kachen and W.H. Lowdermilk, *Phys. Rev.* **A16**, (1977), p1657

[47] D. Grishkowsky, M.M.T. Loy and P.F. Liao, *Phys. Rev.* **A12**, (1975), p2514

[48] A.R. Forsyth, *Theory of Differential Equations*, Dover Puplications, Inc. (1959), **Vol. VI**, p119

[49] A. Sommerfeld, *Partial Differential Equations in Physics*, Academic Press, Inc. (1949), p52

[50] *Handbook of Mathematical Functions*, eds. M. Abramowitz and I. Stegun, U.S. GPO, Washington, (1964), **section 9.6.26**, p120

[51] I.S. Gradshteyn and I.M. Ryzik, *Tables of Integrals, Series and Products*, Academic Press, Inc. (1965), **section 6.618 No. 4**, p711

[52] I.S. Gradshteyn and I.M. Ryzik, *Tables of Integrals, Series and Products*, Academic Press, Inc. (1965), **section 8.468**, p967

[53] *Handbook of Mathematical Functions*, eds. M. Abramowitz and I. Stegun, U.S. GPO, Washington, (1964), **section 9.7.1**, p121

[54] J.G. Kepros and G.R. Fowles, *J. Appl. Phys.*, **45**, (1974), p4554

[55] J.M. Vaughan, *The Fabry-Perot Interferometer*, Adam Hilger - IOP Publishing Ltd., (1989)

[56] M. Born and E. Wolf, *Principles of Optics 6th ed.*, Permagon Press (1986), Ch. 7

[57] M.V. Klein and T.E. Furtak, *Optics 2nd ed.*, John Wiley and Sons, Inc. (1986), Ch. 5

[58] E. Hecht, *Optics 2nd ed.*, Addison-Wesley (1987)

[59] G. Hernandez, *Fabry-Perot Interferometers*, Cambridge University Press (1986)

[60] J. Horrell, *U.C.T. Honours Project*, Unpublished (1990)

[61] F. James and M. Roos, *MINUIT–CERN Library Entry* **D506**, Copyright CERN, Geneva (1989)

[62] A. Yariv *Quantum Electronics 3rd ed.*, John Wiley and Sons (1989), Ch. 6

[63] A.C. Walker in *The Physics and Technology of Laser Resonators*, eds. D.R. Hall and P.E. Jackson, Bristol: Hilger, (1989), Ch1

(k)

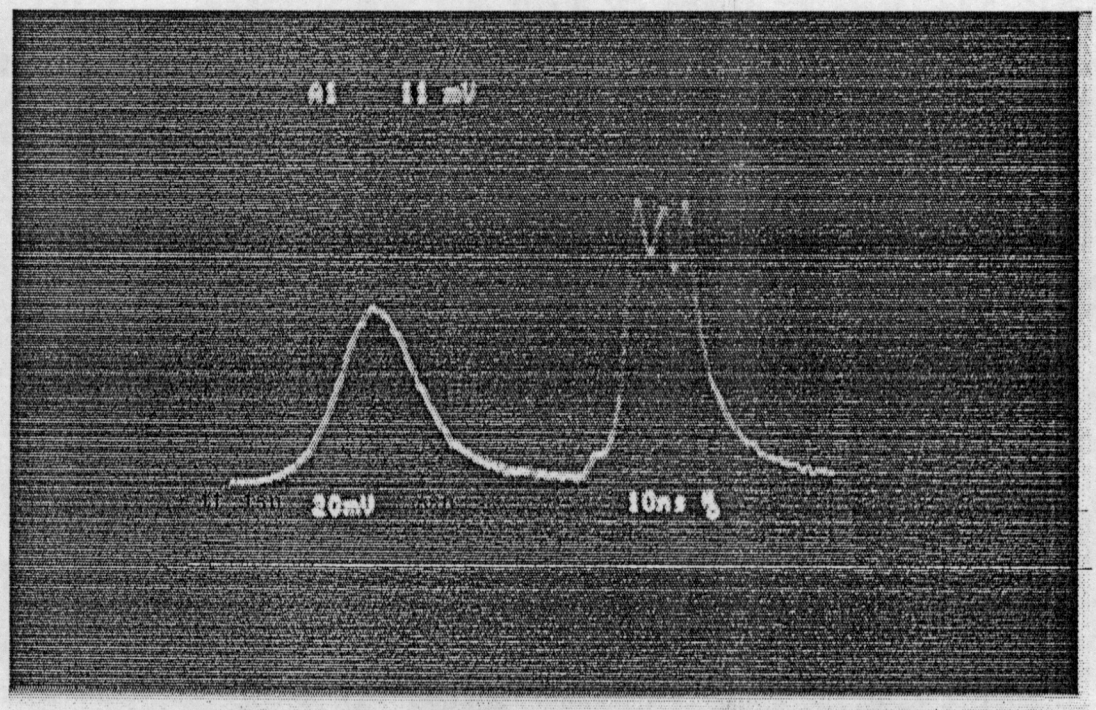

(l)

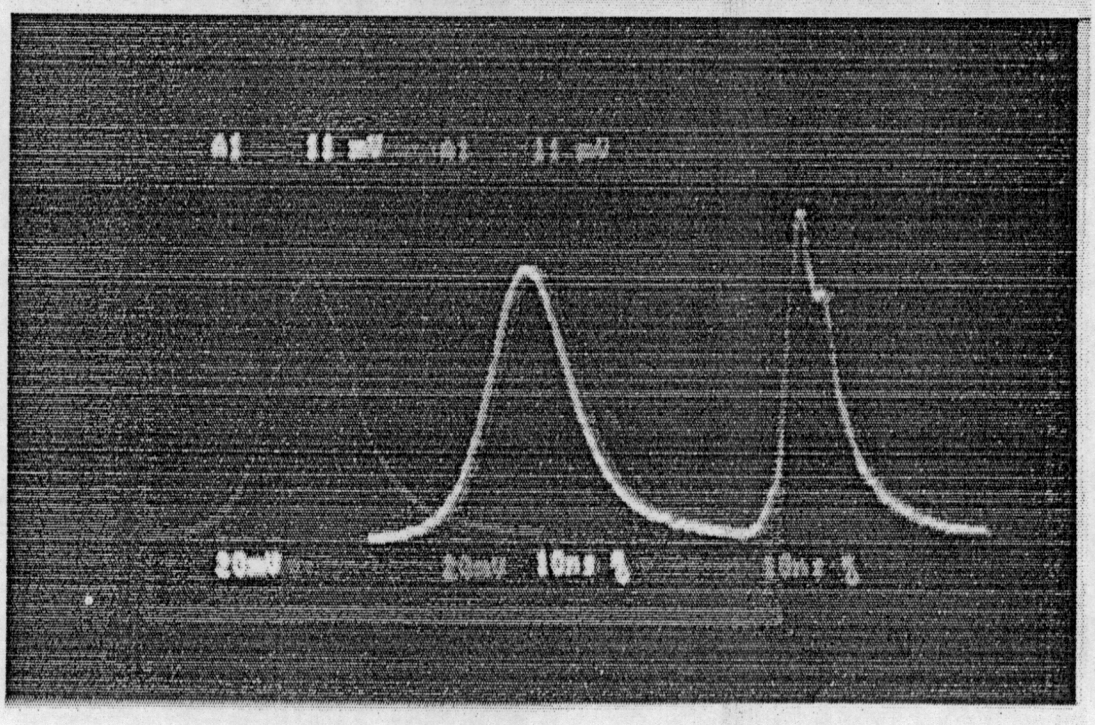

Figure 0.1: illustrates a selection of temporal traces which are combinations of various of the input and ouput beams. We list the combinations in each trace, identifying the left-hand trace first. The following labels are used: P–incident pump, T–transmitted pump, B–backward Stokes, F–forward Stokes and A–forward anti-Stokes. (a)–(c) PT, (d) PA, (e)–(h) PT, (i) BT, (j) BF, (k) PB and (l) PF